

3-21-2013

Power Requirements for Bi-harmonic Amplitude and Bias Modulation Control of a Flapping Wing Micro Air Vehicle

Justin R. Carl

Follow this and additional works at: <https://scholar.afit.edu/etd>

Part of the [Aerospace Engineering Commons](#)

Recommended Citation

Carl, Justin R., "Power Requirements for Bi-harmonic Amplitude and Bias Modulation Control of a Flapping Wing Micro Air Vehicle" (2013). *Theses and Dissertations*. 818.
<https://scholar.afit.edu/etd/818>

This Thesis is brought to you for free and open access by the Student Graduate Works at AFIT Scholar. It has been accepted for inclusion in Theses and Dissertations by an authorized administrator of AFIT Scholar. For more information, please contact richard.mansfield@afit.edu.



**POWER REQUIREMENTS FOR BI-HARMONIC AMPLITUDE AND BIAS
MODULATION CONTROL OF A FLAPPING WING MICRO AIR VEHICLE**

THESIS

Justin R. Carl, Captain, USAF

AFIT-ENY-13-M-37

**DEPARTMENT OF THE AIR FORCE
AIR UNIVERSITY**

AIR FORCE INSTITUTE OF TECHNOLOGY

Wright-Patterson Air Force Base, Ohio

DISTRIBUTION STATEMENT A:
APPROVED FOR PUBLIC RELEASE; DISTRIBUTION UNLIMITED

The views expressed in this thesis are those of the author and do not reflect the official policy or position of the United States Air Force, the Department of Defense, or the United States Government.

This material is declared a work of the U.S. Government and is not subject to copyright protection in the United States.

AFIT-ENY-13-M-37

POWER REQUIREMENTS FOR BI-HARMONIC AMPLITUDE AND BIAS
MODULATION CONTROL OF A FLAPPING WING MICRO AIR VEHICLE

THESIS

Presented to the Faculty
Department of Aeronautical Engineering
Graduate School of Engineering and Management
Air Force Institute of Technology
Air University
Air Education and Training Command
in Partial Fulfillment of the Requirements for the
Degree of Master of Science in Aeronautical Engineering

Justin R. Carl, B.S.M.E.

Captain, USAF

March 2013

DISTRIBUTION STATEMENT A:
APPROVED FOR PUBLIC RELEASE; DISTRIBUTION UNLIMITED

AFIT-ENY-13-M-37

POWER REQUIREMENTS FOR BI-HARMONIC AMPLITUDE AND BIAS
MODULATION CONTROL OF A FLAPPING WING MICRO AIR VEHICLE

Justin R. Carl, B.S.M.E.
Captain, USAF

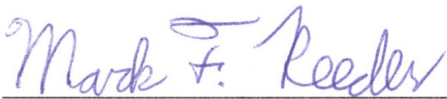
Approved:



Richard G. Cobb, PhD (Chairman)

4 MAR 2013

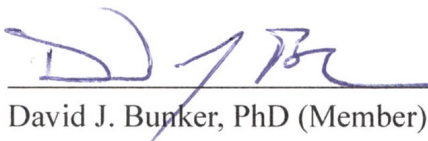
Date



Mark F. Reeder, PhD (Member)

4 Mar 2013

Date



David J. Bunker, PhD (Member)

4 Mar 2013

Date

Abstract

Flapping wing micro air vehicles (FWMAV) have been a growing field in the research of micro air vehicles, but little emphasis has been placed on control theory. Research is ongoing on how to power FWMAVs where mass is a major area of concern. However, there is little research on the power requirements for the controllers to manipulate the wings of a FWMAV.

A novel control theory, bi-harmonic amplitude and bias modulation (BABM), allows two actuators to produce forces and moments in five of the FWMAV's six degrees of freedom (DOF). Several FWMAV prototypes were constructed and tested on a six-component balance. Data was collected for varying control parameters and the generated forces were measured. The results mapped control parameters to different degrees of freedom. The force required to generate desirable motion and power required to generate that motion was plotted and evaluated. These results can be used to generate a minimum power controller in the future.

The results showed that BABM control required a 26% increase in power in order to increase lift by 22%. The lift increase was accomplished by increasing the amplitude by 10% over the established baseline. The data also showed that varying some parameters actually decreased the power requirements, allowing other parameters to increase which in turn would enable more complex maneuvers. For instance, an asymmetric change in split-cycle shift of ± 0.25 decreased the power required by 14% and decreased the lift by 25%. Changing the stroke bias to ± 0.75 had a negligible effect on power but decreased the lift by 27%. Furthermore, the data identified certain parameter combinations which resulted in other forces and moments. These results identified how BABM be used as a control theory for the control of FWMAVs.

*To God Almighty
Whose awesome creation drives
Our inspiration*

*To my loving wife
Who gave me strength and support
Throughout this process*

Acknowledgments

I would like to thank Dr. Richard Cobb for his guidance in this research and in my pursuit of a Master's degree and for pushing me to understand the world we live in. I would also like to thank Dr. Mark Reeder for his insight into the world of FWMAVs. To all those who came before me who set up a process and method of FWMAV research here at AFIT. To Capt Garrison Lindholm for his instruction into the control of FWMAVs. Additionally to Nelson Freeman for helping a MS candidate learn the most basic skills of building FWMAVs. Also to Lt Rob Lenzen for his companionship as we accomplished FWMAV work together. This would not have been possible without all the help of the people around me.

Justin R. Carl

Table of Contents

	Page
Abstract	iv
Dedication	v
Acknowledgments	vi
Table of Contents	vii
List of Figures	x
List of Tables	xiii
List of Symbols	xiv
List of Acronyms	xvii
I. Introduction	1
1.1 Motivation	2
1.2 Research Goals	2
1.3 Organization of Thesis	3
II. Background & Literature Review	4
2.1 The <i>Manduca sexta</i>	4
2.1.1 Mass	5
2.1.2 Wings	6
2.1.3 Locomotion	7
2.2 Design Considerations	8
2.3 The AFIT FWMAV	13
2.3.1 Wings	13
2.3.2 Locomotion	14
2.4 Control in FWMAVs	15
2.4.1 Flapping at Resonance	18
2.4.2 Bi-harmonic Amplitude and Bias Modulation	18
2.5 Power	23
2.5.1 Power System	24

	Page
2.5.2 Proposed Power Boosters	25
2.5.3 Power Supply	27
2.6 Chapter Summary	28
III. Test Methodology	29
3.1 Flapper	29
3.1.1 Flapper Materials	29
3.1.1.1 YSH-70A Carbon Fiber	30
3.1.1.2 Kapton	30
3.1.1.3 Mylar	31
3.1.2 Tools of Construction	31
3.1.3 Flapper Construction	32
3.1.3.1 Structure and Linkage	33
3.1.3.2 Rotation Joint	36
3.1.3.3 Wing	37
3.1.3.4 Assembly Clips	37
3.1.4 Assembly	37
3.2 Experimental Setup	39
3.3 Experimental Procedure	41
3.3.1 BABM Parameters	43
3.3.2 Design of Experiments	43
3.4 Chapter Summary	45
IV. Analysis and Results	47
4.1 Analysis	47
4.1.1 Data Processing	47
4.1.2 Center of Pressure	49
4.2 Single Wing Flapper	56
4.2.1 Amplitude	56
4.2.2 Split-cycle Shift	59
4.2.3 Stroke Bias	64
4.2.4 Design of Experiments	65
4.2.5 Randomized Verification	69
4.3 Dual Wing Flapper	73
4.3.1 Amplitude	73
4.3.2 Split-cycle Shift	79
4.3.3 Stroke Bias	85
4.3.4 Design of Experiments	89

	Page
4.4 Comparison to Earlier Work	93
4.5 Chapter Summary	93
V. Conclusions	94
5.1 Research Goals	94
5.2 Summary of Results	94
5.2.1 Power	95
5.2.2 Controllability	96
5.3 Future Work	97
Appendix: Explanation of MATLAB Scripts	99
Bibliography	106
Vita	110

List of Figures

Figure	Page
2.1 <i>Manduca sexta</i>	5
2.2 <i>Manduca sexta</i> average mass distribution	7
2.3 Cross-sectional view of the primary flight muscles	8
2.4 Proposed FWMAV mass properties for a 1.55 g vehicle	10
2.5 Simultaneous drive bimorph PZT actuator	15
2.6 Defined axis system	17
2.7 Split-cycle wing trajectory	19
2.8 Effect of amplitude on drive signal	22
2.9 Effect of split-cycle shift on drive signal	23
2.10 Effect of stroke bias on drive signal	24
2.11 Hybrid voltage multiplier	25
2.12 Boost converter with autotransformer	26
2.13 PT transformer equivalent circuit and amplifier	28
3.1 Constructed flapper	30
3.2 LPKF Multipress S	32
3.3 LPKF Protolaser U	33
3.4 Flapper parts for assembly	34
3.5 Final linkage configuration	35
3.6 Layup for multipress to make parts for assembly	36
3.7 Constructed flapper with piezoelectric actuator	39
3.8 Experimental setup	40
3.9 Sample FRF for a flapper	42

Figure	Page
4.1 Sample of raw lift data	48
4.2 Simulink model to compute power	49
4.3 Dual-wing flapper center of pressure and balance axes	50
4.4 Aerodynamic dimensions of FWMAV wing	50
4.5 Actuator displacement vs. amplitude	52
4.6 Actuator displacement vs. split-cycle shift, $\tau(n)$	53
4.7 Actuator displacement vs. stroke bias, $\eta(n)$	54
4.8 Measured pitch moment correction to center of pressure	55
4.9 Power vs. amplitude	57
4.10 Forces and moments about the balance center vs. amplitude	58
4.11 Power per lift vs. amplitude	59
4.12 Power vs. split-cycle shift	60
4.13 Drive signal with a split-cycle shift of $\pi/4$	61
4.14 Power vs. split-cycle shift	61
4.15 Forces and moments about the balance center vs. split-cycle shift	62
4.16 Power per lift vs. split-cycle shift	63
4.17 Power vs. stroke bias	65
4.18 Forces and moments about the balance center vs. stroke bias	66
4.19 Power per lift vs. stroke bias	67
4.20 DOE results for single-wing flapper	68
4.21 BABM parameter effects on power for a single-wing flapper	70
4.22 BABM parameter effects on lift for a single-wing flapper	71
4.23 Power vs. amplitude, random sampling	71
4.24 Power vs. split-cycle shift, random sampling	72
4.25 Power vs. stroke bias	72

Figure	Page
4.26 Power vs. amplitude, left wing	74
4.27 Power vs. amplitude, right wing	75
4.28 Forces and moments about the balance center vs. amplitude, left wing	76
4.29 Forces and moments about the balance center vs. amplitude, right wing	77
4.30 Power per lift vs. amplitude, left wing	78
4.31 Power per lift vs. amplitude, right wing	78
4.32 Power vs. split-cycle shift, left wing	79
4.33 Power vs. split-cycle shift, right wing	80
4.34 Forces and moments about the balance center vs. split-cycle shift, left wing	82
4.35 Forces and moments about the balance center vs. split-cycle shift, right wing	83
4.36 Power per lift vs. split-cycle shift, left wing	84
4.37 Power per lift vs. split-cycle shift, right wing	84
4.38 Power vs. stroke bias	85
4.39 Forces and moments about the balance center vs. stroke bias	87
4.40 Power per lift vs. stroke bias	88
4.41 DOE results for dual-wing flapper	90
4.42 BABM parameter effects on power for a dual-wing flapper	91
4.43 BABM parameter effects on lift for a dual-wing flapper	92

List of Tables

Table	Page
2.1 <i>Manduca sexta</i> Classification	6
2.2 Two-winged MAV flapping mechanisms	12
2.3 Linear actuator characteristics	15
2.4 Summary of aerodynamic forces and moments caused by control variables . . .	21
3.1 DOE parameters for a single-wing flapper	44
3.2 DOE parameters for a dual-wing flapper	46
4.1 Baseline of aerodynamic forces and moments caused by BABM parameters . .	56
5.1 Effects of BABM parameters on power and lift	95
5.2 Summary of forces and moments generated by changing BABM parameter . .	96

List of Symbols

Symbol	Definition
A	Stroke Amplitude
E	Elastic Modulus
L	Roll Moment
M	Pitch Moment
M_n	n^{th} Fourier Coefficient
M_x	Moment About the X -axis
M_y	Moment About the Y -axis
M_z	Moment About the Z -axis
M_{ω_n}	Magnitude of the Wing Displacement at the First System Resonance
$M_{2\omega_n}$	Magnitude of the Wing Displacement at Twice the First System Resonance
N	Yaw Moment
P	Power
R	Wingspan
R_I^B	Rotation Matrix from the Inertial Reference Frame to the Body Frame
Re	Reynolds Number
S	Wing Area
X	Axial Force in the in the X -direction
Y	Axial Force in the in the Y -direction
Z	Axial Force in the in the Z -direction
g	Gravity
m	Mass
n	Sample

Symbol Definition

p Roll Angular Rate

q Pitch Angular Rate

r Yaw Angular Rate

u Translational Velocity in the X -direction

v Translational Velocity in the Y -direction

w Translational Velocity in the Z -direction

\mathcal{R} Aspect Ratio

α Wing Angle of Attack

β Phase Shift

γ Phase Angle

δ Actuator Tip Deflection

η Stroke Bias

θ Wing Elevation Angle

τ Split-cycle Shift

ϕ Wing Stroke Angle

ϕ_{ω_n} Phase of the Wing Displacement at the First System Resonance

Subscripts

L Left Wing

R Right Wing

cp Center of Pressure

rms Root Mean Square

s Sample

Symbol Definition

Superscripts

bal Balance Reference Frame

List of Acronyms

Acronym	Definition
AFIT	Air Force Institute of Technology
AFRL	Air Force Research Laboratory
BABM	Bi-harmonic amplitude and bias modulation
DAQ	Data acquisition
DC	Direct current
DHPC	Discrete harmonic plant compensation
DLMs	Dorsal longitudinal muscles
DOE	Design of experiments
DOF	Degrees of freedom
DVMs	Dorsal ventral muscles
EAP	Electro active polymers
FRF	Frequency response function
FWMAV	Flapping wing micro air vehicle
ISR	Intelligence, surveillance, and reconnaissance
MAV	Micro air vehicle
MEMS	Microelectromechanical systems
PET	Polyethylene terephthalate
PSD	Power spectral density
PT	Piezoelectric transformer
PVDF	Piezo polymers
PZT	Lead zirconate titanate
SMA	Shape memory alloy

Acronym	Definition
UAV	Unmanned aerial vehicle
UV	Ultraviolet

POWER REQUIREMENTS FOR BI-HARMONIC AMPLITUDE AND BIAS MODULATION CONTROL OF A FLAPPING WING MICRO AIR VEHICLE

I. Introduction

RECENT years have seen an increase in use for unmanned aerial vehicles (UAVs). It is becoming apparent that they are now a major mainstay in American warfare. UAVs play a pivotal role in the intelligence, surveillance, and reconnaissance (ISR) mission affording troops unrivaled capabilities. UAVs also supported troops by serving as local weather sensors and communication relays. In that class falls the micro air vehicle (MAV). A key role that often comes to mind is the MAV's capability to fulfill the stealthy, persistent, perch, and stare mission. This calls for a MAV capable of flying to difficult targets, landing in a perched position, conducting surveillance, and returning to home base. [38] Furthermore, the possible roles of MAVs are ever expanding with new potentials such as the delivery of computer viruses without putting troops in harm's way. Multiple ideas have been investigated to generate a MAV to fulfill this mission to include fixed wing, rotary wing, and flapping wing aircraft.

A bio-inspired MAV, one whose design is based on nature, would have the inherent benefit of stealth through mimicry of insects. Such a MAV is referred to as a flapping wing micro air vehicle (FWMAV). A FWMAV takes advantage of several unsteady aerodynamic effects in the low Reynolds number regime. [3] A FWMAV could meet mission requirements while being unobtrusive and pervasive.

1.1 Motivation

The Air Force Institute of Technology (AFIT) has dedicated much research to the development of a bio-inspired FWMAVs. It was evident very early on that the miniscule mass of the FWMAV was a major concern. As such, there is a desire to focus research on reducing the power requirements of the FWMAV therefore reducing the mass of the power supply. However, as of now, there is not a clear understanding of the current power requirements of the FWMAV. AFIT has developed a control theory called bi-harmonic amplitude and bias modulation (BABM) based on wing-beat shape modulation developed by the Air Force Research Laboratory (AFRL). [5, 14, 15] Research is under way to identify how the BABM scheme will be implemented to achieve mission worthiness. It is known that through BABM, five parameters can control the FWMAV in 5 degrees of freedom (DOF) but little is known about how much power is required to vary those five parameters. [6] Without knowledge of the power requirements, control logic cannot be designed to maneuver the FWMAV and minimize the mass of the power supply. This research focused on characterizing those power requirements for the BABM control scheme.

1.2 Research Goals

As stated above, the goal of this research was to investigate the power requirements of AFIT's current FWMAV using the BABM control scheme. Gathered data was processed and will be provided to other researchers for use in trajectory and control optimization and control optimization. With this data, the trajectories can be optimized to require the least amount of power and the control logic can be optimized to manipulate the five BABM parameters to minimize the power needed.

Data was collected on a single-wing flapper at first. Trends were applied to the model, and consistency among wings was verified. These practices removed any suspicion that the manufacturing process provides a large amount of variation between test samples.

The single-wing flapper also verified that the research approach is valid. After those requirements were met on the single-wing flapper, testing began on a dual-wing flapper. Testing was similar to that of the single-wing flapper but with expanded goals. The data collected from the dual-wing flapper indicated variations between the left and right wing. It also provided moment and force data more representative of an operational FWMAV.

Succinctly, the thesis statement for this research is: *How much power is required to vary each parameter and maintain lift? How do those power requirements relate to controllability?*

This work assumed that the results acquired will be representative of an operational FWMAV. It was also assumed that the measured power results are valid for any given set of electronics driving the actuator. There are some limitations to this research. To accelerate the development time of the AFIT FWMAV, multiple areas of research are being investigated simultaneously. As such, any findings from other research areas that affect the design or production of the FWMAV will not be represented in this research. It is important to state that the test methodology will remain the same for future testing of different FWMAV designs. The results were expected to show that an increase in any BABM control parameter would result in greater or equal power requirements. The conclusions developed during this research will aid in the control logic development.

1.3 Organization of Thesis

The organization of this thesis is chronological and increasing in technical detail. Chapter II discusses previous research in the area and lays the groundwork for this research. Chapter III dives into the methodology used for data collection. Chapter IV presents the processed data collected from testing and provides the basis for the conclusions. Chapter V presents the conclusions drawn from the data and suggestions for future work.

II. Background & Literature Review

THE history of research into FWMAVs is extensive. One may say it began when the military first started to investigate unmanned aircraft or it may have started when man first began to study the flight of our winged friends in hopes of achieving flight. The recent ramp in technology has brought UAVs into the forefront of military leadership. For instance, UAVs flew over 100,000 total flight hours by September 2004 in support of Operation ENDURING FREEDOM and Operation IRAQI FREEDOM. [37] An increased focus on ISR missions to clandestine or denied entry locations has concentrated research on biomimicry. [2] By studying our cohabitants, researchers have gained insight into small-scale aerodynamics. Bio-inspired MAVs may one day offer unparalleled capability. As such, a lot of previous research has been done on the development of FWMAVs.

AFIT researchers have found a niche to fulfill in the FWMAV community. The research conducted at AFIT focuses on a FWMAV with a wingspan around 10 centimeters and a mass around 1.5 grams. Multiple researchers have focused on smaller or larger FWMAVs. AFIT also developed the BABM control scheme and discrete harmonic plant compensation (DHPC) to manipulate the wings of the FWMAV. A clear understanding of what research has been done in all of the previous topics is required to place the research conducted herein in context.

2.1 The *Manduca sexta*

The first step to any bio-inspired system is a thorough understanding of the creature who serves as the inspiration. The FWMAV used for this research has been inspired by the *Manduca sexta*, or hawkmoth, shown in Figure 2.1. The *M. sexta* is a North American moth with long forewings, short hind wings, and the ability to hover and move side-to-side. [29] This extraordinary ability made the *M. sexta* the perfect candidate. [39] They are also

easily reared in a laboratory, have short life cycles, and are large, all of which aide in many scientific investigations. Due to these qualities, there is no shortage of literature on the study of *M. sexta*. The biological classification of the *M. sexta* is found in Table 2.1.



Figure 2.1: *Manduca sexta* [23]

2.1.1 Mass.

The size of the *M. sexta*, like with most creatures, varies based on gender. Figure 2.2 shows average mass values obtained for the *M. sexta* based on 30 samples. The total mass of the *M. sexta* averages only 1.55 ± 0.05 grams. [39] In order to create a FWMAV based on the *M. sexta*, the FWMAV must be of similar mass. The limitations to the FWMAV mass will be discussed later.

Table 2.1: *Manduca sexta* Classification [35]

Kingdom	<i>Animalia</i>
Phylum	<i>Arthropoda</i>
Class	<i>Insecta</i>
Order	<i>Lepidoptera</i>
Family	<i>Sphingidae</i>
Genus	<i>Manduca</i>
Species	<i>Manduca sexta</i>

2.1.2 Wings.

Much consideration was given to matching the FWMAV wing to the *M. sexta* wing. Insect exoskeletons are formed from a complex blend of polymer-based chains that make up the body, limbs, and wings, which act as a barrier between the living tissues of the insect and the environment. [22] Epidermal layers on the wing membrane are supported by the venation. The veins act as structural members, carry nerves, and carry hemolymph to the wings. Wing mass is dominated by the mass contributions of the venation (80%), membrane (10%), and scales (10%). The wing is discussed in terms of span, chord, and aspect ratio similar to fixed wings. The wingspan, R , is typically 45-55 millimeters. The wing area, S is typically 715 mm^2 . The aspect ratio, \mathcal{R} , of the *M. sexta* is approximately 14.0-15.0. The mass of the *M. sexta* forewing averages approximately 34.6 mg. The area centroid falls at roughly 37.3% of the wing length and at 59.5% of the maximum wing chord. [39]

When discussing the wing properties of the *M. sexta*, one will find separate discussion of the properties of the venation and the membrane informative. As stated above, the veins act as the structural members of the wing. Analysis has shown that the density of the

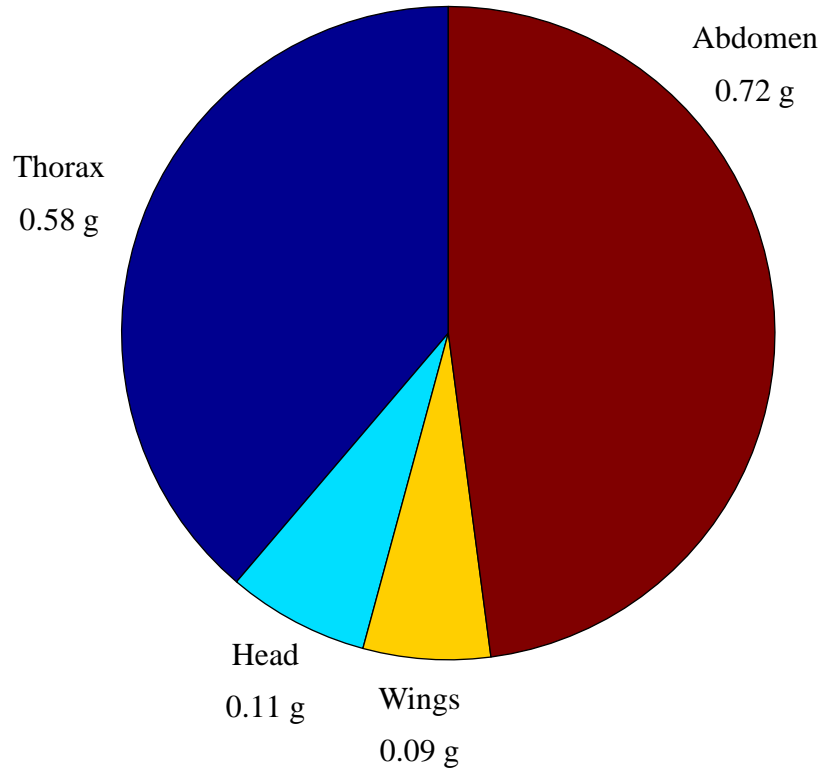


Figure 2.2: *Manduca sexta* average mass distribution [39]

veins to be 2.4258 g/cm^3 and the elastic modulus, E , approximately to be 7.41 gigapascals. The membrane elastic modulus has been calculated to be approximately 2.446 gigapascals. [39] In later sections, an examination will be made of prior efforts to match the physical characteristics of the biological wing.

2.1.3 Locomotion.

The *M. sexta* primarily uses two major muscles to produce the power required for flapping: the dorsal longitudinal muscles (DLMs) and the dorsal ventral muscles (DVMs).

These are common to the majority of flying insects and are located in the thorax. When the DVMs contract, they pull the dorsal surface of the thorax downward and the wings rotate upward. When the DLMs contract, they bow the dorsal surface upward and the wings rotate downward. The constant contraction and relaxations of these two muscles power the flapping wings of flying insects. Figure 2.3 shows the muscle motions and how they produce flapping.

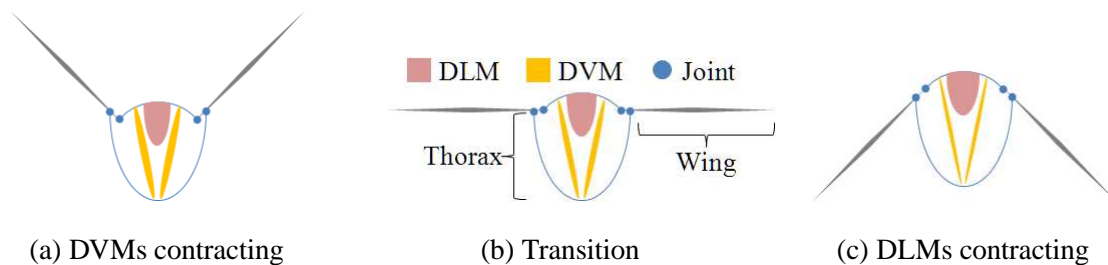


Figure 2.3: Cross-sectional view of the primary flight muscles (reproduced from [12])

The DLMs are the largest muscle in the *M. sexta*, comprising 5-8% of the total body mass. [43] Both the DVMs and the DLMs are comprised of multiple muscle units. The DLMs have five muscle units and the DVMs have six muscle units. Most research concludes that the power output of the *M. sexta* muscle structure outputs 81-202 W/kg. [12]

2.2 Design Considerations

The next step to the design of a bio-inspired system is to mimic the properties of the biological creature as closely as possible. The techniques used to manufacture FWMAVs must be simple enough to be repeatable and durable enough to operate for multiple testing cycles.

Manufacturing is a major concern when considering the development of a FWMAV. Without the capability to manufacture a FWMAV test bed, testing is not possible and so manufacturing is discussed. Above everything else in the design considerations is weight. Materials must be used that are durable to withstand the physics of small-scale flight but light enough to achieve flight. As a prefatory step, the FWMAV was split into similar proportions as the *M. sexta* resulting in the proposal in Figure 2.4. The thorax actuates the wings on the *M. sexta* and was therefore likened to the actuator; the abdomen holds the organs that process energy and was therefore likened to the power source; and, the head holds the eyes and antennae and was therefore likened to the sensors. The similarities can easily be seen between Figure 2.2 and Figure 2.4 and they simply demonstrate a reasonable mass allocation based on biomimicry.

Analysis showed that composites was an appropriate material for the structure and wings to obtain the mass and elastic modulus requirements. [39] They provide the strength to weight ratios desired for sustained flight in the insect-sized regime. Composites also simplify manufacturing compared to other methods. The choice of a composite relies on matching the characteristics of the *M. sexta*.

Once the FWMAV has been assembled with a reliable repeatable process, discussed in Chapter III, the wings must be actuated to achieve flight. There are two types of actuators being used in FWMAVs: linear and rotary. Much work has been done on the comparison of the two types of actuators for FWMAVs. Many designs use rotary direct current (DC) motors for actuation. [11, 13, 28] However, DC motors typically operate around 15,000 rpm so a gear reduction must be used to make them suitable for this application. A complex crank-rocker mechanism is then used to transform the rotary motion into the required linear motion. The crank-rocker must be designed so that it is only partially constrained allowing for some degree of controllability. [11] An unavoidable drawback to DC motors is the

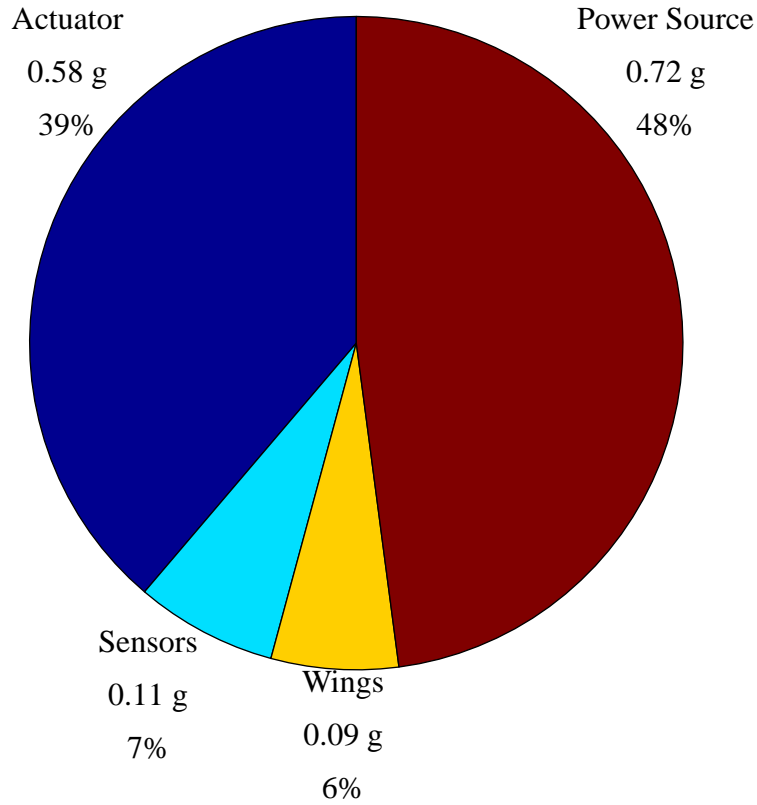


Figure 2.4: Proposed FWMAV mass properties for a 1.55 g vehicle

minimum size lower bound. The smallest DC motors currently weight approximately 200 mg. [3] The large size of DC motors places a lower bound on the size of FWMAVs, a lower bound that is larger than desired. An often overlooked key design goal is a low acoustic signature to make vehicles less susceptible to detection. [37] Current DC driven FWMAVs have significant acoustic noise, lowering their stealth capability. [27] Another option is the linear actuator. With the linear actuator, there is no need for a crank-rocker mechanism, which significantly simplifies the design. Linear acutators also have lower acoustic signatures than DC motors. Table 2.2 summarizes the actuator options and the

crank-rocker mechanisms. Note that Conn et al. published this summary in 2007, prior to the control scheme discussed in Section 2.4. From Table 2.2, the linear actuators provide the greatest number of adjustable parameters.

Table 2.2: Complexity and performance classification of two-winged MAV flapping mechanisms [11]

Mechanism	Five-bar coupler with four-bar	Four-bar coupler and Geneva wheel	Scotch Yoke and Geneva wheel	Double scotch yoke and Geneva wheel	Non-planar crank-rocker	Parallel crank-rocker	Parallel four-bars	Dipteran (two-winged insect)
Complexity								
Input Type	Rotary	Rotary	Rotary	Rotary	Rotary	Rotary	Linear	Linear
Control Inputs	1	1	1	1	1	3	8	12
Actuators	1	1	1	1	1	3	8	50
Performance								
Wing trajectory	Fixed two	Fixed two	Fixed one	Fixed two	Fixed one	Fixed one	Adjustable	Adjustable
Angle of Attack, α	DOF	DOF	DOF	DOF	DOF	DOF	one DOF	two DOF
Stroke amplitude, Φ	Fixed	Fixed	Fixed	Fixed	Fixed	Adjustable	Adjustable	Adjustable
Controllable body	Fixed	Fixed	Fixed	Fixed	Fixed	Fixed	Adjustable	Adjustable
DOF	1	1	1	1	1	4	4	4

2.3 The AFIT FWMAV

AFIT researchers have dedicated considerable time and resources to matching the characteristics of the *M. sexta*, and those efforts will be summarized here. The manufacturing techniques adopted by AFIT will also be reviewed in this section. For a more detailed discussion of the development of the AFIT FWMAV, the reader is encouraged to read reference 39.

2.3.1 Wings.

Previous work has been done to mimic the *M. sexta* wings. The goal of the engineered wing structure is to match the structural properties and the dynamic response of the *M. sexta*. The materials of the wings were investigated with relation to two parts of the wing: the venation and the membrane.

For the wing venation, AFIT researched multiple materials including isotropic metals, shape memory alloys, ultraviolet (UV) cured polymers and composite high modulus thin ply laminates. It was discovered early on that isotropic metals and shape memory alloys would be too massive to meet the requirements of a FWMAV. It was found that UV cured polymers did not provide the strength required to match the biological wing. The experimentation did prove that a composite high modulus lamina, YSH-70A, was identified as a potential match to the biological wing. YSH-70A fibers are a high modulus fiber that are produced with a larger yield size. The YSH-70A fibers are manufactured with a RS-3C epoxy resin embedded. To match the *M. sexta* characteristics, the YSH-70A fibers are layered in a 0-90-0 orientation. After further testing, this material and orientation were found to be a nearly ideal material for engineering wing venation. [39]

For the wing membrane, a focus was based on the mass and strength of possible choices. Two primary materials were investigated: Kapton and Mylar. Kapton is a polyimide film manufactured by DuPont. Kapton is available in thicknesses of 12.5, 25, and 75 μm . Measurements found that a Kapton membrane would weigh approximately

22.5 mg for an engineered wing similarly sized to a biological wing. This large mass proved to be too large. Mylar is a polyester film manufactured by DuPont used for high strength applications and its dimensional stability properties. The Mylar used is 2.5 μm thick with an elastic modulus of 3.7 gigapascals, which is similar to the representative biological value of 2.4 gigapascals. Measurements found that a Mylar membrane would weigh approximately 4.5 mg making it the best choice for the engineered wing. [39]

2.3.2 Locomotion.

AFIT researchers have chosen to pursue the use of two linear actuators over a single rotary actuator since linear actuators provide lower mass, provide lower acoustic signature, and simplify the transmission. Table 2.3 taken from [3] (adapted from [10]) shows a comparison between linear actuator options and the insect flight muscle. Since the table is taken from many varying sources, it was used as a general comparison tool. From the table, lead zirconate titanate (PZT) actuators are superior to insect muscles in all categories except strain. A linkage was created to increase the magnitude of the piezoelectric actuator tip displacement to overcome the strain deficiency.

AFIT researchers have chosen to use a bimorph piezoelectric actuator made of PZT to drive the FWMAV. A bimorph piezoelectric actuator uses two layers of PZT material and a passive layer sandwiched between them. [44] A bimorph piezoelectric actuator is shown in Figure 2.5. The piezoelectric actuator is driven using simultaneous drive. Simultaneous drive, also shown in Figure 2.5, is a more economical technique and prevents hysteresis techniques associated with other driving schemes. This method initially charges each actuator with a bias voltage, V_b , and then charges the central passive layer with the drive voltage, V_d . [45]

Table 2.3: Linear actuator characteristics [3]

Actuator Type	Strain (%)	Stress (MPa)	Frequency (Hz)	Specific Energy Density (J/g)	Efficiency (%)
Synchronous Flight Muscle	17	0.35	5.5-100	0.003	2-13%
Asynchronous Flight Muscle	2	-	100-1046	0.002	5-29%
PZT	0.2	110	108	0.013	90
PVDF	0.1	4.8	107	0.0013	90
SMA (TiNi)	5	200	101	15	10
Solenoid	50	0.1	102	0.003	90
EAP (Dielectric Elastomer)	63	3	104	0.75	90

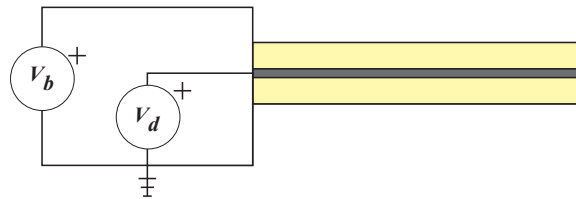


Figure 2.5: Simultaneous drive bimorph PZT actuator

2.4 Control in FWMAVs

An emphasis has been placed on reducing weight, increasing agility, and integrating robotics in future forces. [38] Increasing agility and integrating robotics indicates that control is a pivotal part of the future of MAVs. In the past, the aerodynamics and manufacturing proved to be such daunting tasks that control was set aside. However, as

our understanding of the flight mechanisms has increased as well as our ability to micro-fabricate small structures, control theory must make leaps and bounds to catch-up. In *Design and Control of Flapping Wing Micro Air Vehicles*, Anderson introduced a new method of control for FWMAVs actuated with piezoelectric actuators called bi-harmonic amplitude and bias modulation (BABM). [3] BABM control with DHPC allows two actuators to produce forces and moments in five DOF. It is with BABM that the AFIT FWMAV would be controlled.

The axis system taken from Doman et al. is used and defined in Figure 2.6. [14] Therefore, lift is in the positive X direction during hover and thrust is in the negative Z direction during hover. Note that the X and Z -axes are relative to the FWMAV and thus only align with lift and thrust direction while hovering. The side-force is out the FWMAV's right wing. Perhaps the most confusing aspect of transferring knowledge from fixed wing aircraft to flapping wing aircraft is the difference in moment definitions. A moment about the X -axis is still referred to as the rolling moment but it controls the direction of the thrust vector in a plane parallel to the ground during hover. A moment about the Y -axis is still referred to as the pitching moment but it controls the direction of the thrust vector in a plane perpendicular to the ground during hover. A moment about the Z -axis is still referred to as the yawing moment but it controls the direction of the lift vector in a plane perpendicular to the ground during hover. [36] Three angles define the wing position at any point during the flapping cycle: the wing angle of attack, α , the wing stroke angle, ϕ , and the wing elevation angle, θ . [8] Figure 2.6 identifies these three angles.

The rigid body equations of motion are presented here in the FWMAV body frame:

$$I \begin{bmatrix} \dot{p} \\ \dot{q} \\ \dot{r} \end{bmatrix} = \begin{bmatrix} L \\ M \\ N \end{bmatrix} - \begin{bmatrix} p \\ q \\ r \end{bmatrix} \times I \begin{bmatrix} p \\ q \\ r \end{bmatrix} \quad (2.1)$$

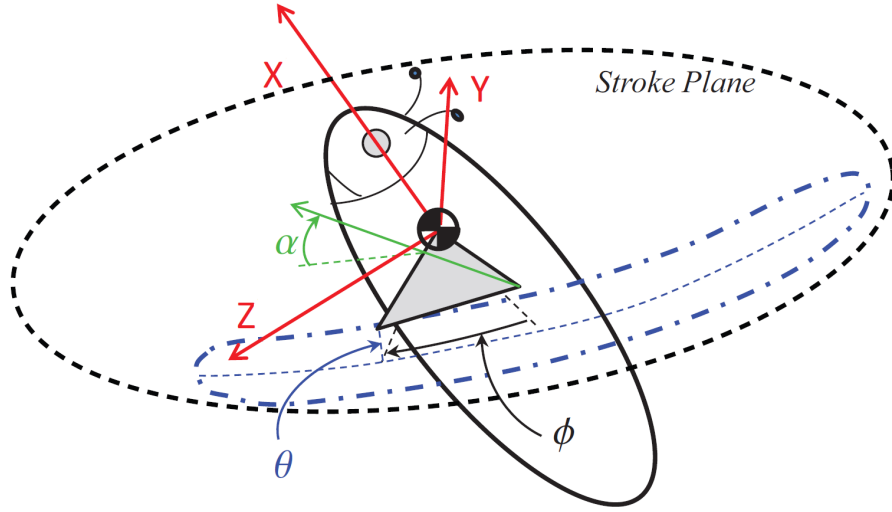


Figure 2.6: Defined axis system [30]

$$\begin{bmatrix} \dot{u} \\ \dot{v} \\ \dot{w} \end{bmatrix} = \begin{bmatrix} qw - rv \\ ru - pw \\ pv - qu \end{bmatrix} + \left(\frac{1}{m}\right) \begin{bmatrix} X \\ Y \\ Z \end{bmatrix} - R_I^B \begin{bmatrix} 0 \\ 0 \\ -g \end{bmatrix} \quad (2.2)$$

where I is the inertia matrix, $\begin{bmatrix} p & q & r \end{bmatrix}^T$ are roll, pitch, and yaw angular rates, $\begin{bmatrix} L & M & N \end{bmatrix}^T$ are the roll, pitch, and yaw moments, $\begin{bmatrix} u & v & w \end{bmatrix}^T$ are the translational velocities, m is the mass, $\begin{bmatrix} X & Y & Z \end{bmatrix}^T$ are the axial forces, R_I^B is a rotation matrix from the inertial frame to the body frame, and g is the gravitational acceleration. [41] This notation is common in aircraft control.

There is no commonly agreed-upon control scheme for FWMAVs and so each FWMAV designer has developed a unique control scheme to meet their requirements. Research has shown that discussions of FWMAV control can be split into two categories: single-DOF control and multi-DOF control. The only necessary angle for wing flapping is the wing stroke angle, and therefore, all controllers use that as a DOF. In the case of single-DOF controllers, it is the only DOF. Beyond that, developers have added the wing

angle of attack and the wing elevation angle, usually in that order, to achieve further control. The FWMAV with the most controllable DOF will be the most controllable vehicle. [6]

2.4.1 Flapping at Resonance.

Research shows that most biological fliers flap their wings at the first natural frequency of their muscle system. There is a tendency of a species to flap at a consistent frequency across all flight regimes. Furthermore, researchers found that by artificially shortening the insect's wings, the wing beat frequency increases. This agrees with the hypothesis that insects flap at their resonant frequency since the frequency varies inversely with the load on the system. There is advantageous energetic expenditure when mechanical systems operate at resonance. [16]

The advantage of low energetic expenditure is very useful to the designer of the power system for the FWMAV. Since the power system may be one of the heavier components, any reductions will be manifested as benefits in range, endurance, speed, and payload. Flapping at resonance does generate some concerns for the control developer though. For instance, vehicles flapping at resonance will make it difficult to drive the wings in a pattern other than harmonic motion. However, the need for energetic efficiency may overcome the desire to avoid resonance and therefore, techniques must be developed for non-harmonic resonant flapping. [6]

2.4.2 Bi-harmonic Amplitude and Bias Modulation.

The control used for this research will be BABM. BABM generates non-harmonic wing flapping creating non-zero cycle-averaged forces resulting in aerodynamic forces and moments. [5] BABM was adapted from the split-cycle theory presented by Doman et al. in reference 15. The idea is to combine two cosine waves with differing frequencies to create one wing beat cycle allowing control over the translational and rotational degrees of freedom of the vehicle. An example is shown in Figure 2.7. The blue line represents a

symmetric cosine wave and the green line represents a split-cycle cosine wave. The up and down-strokes are not symmetric, that is, the wing travels faster in one than the other.

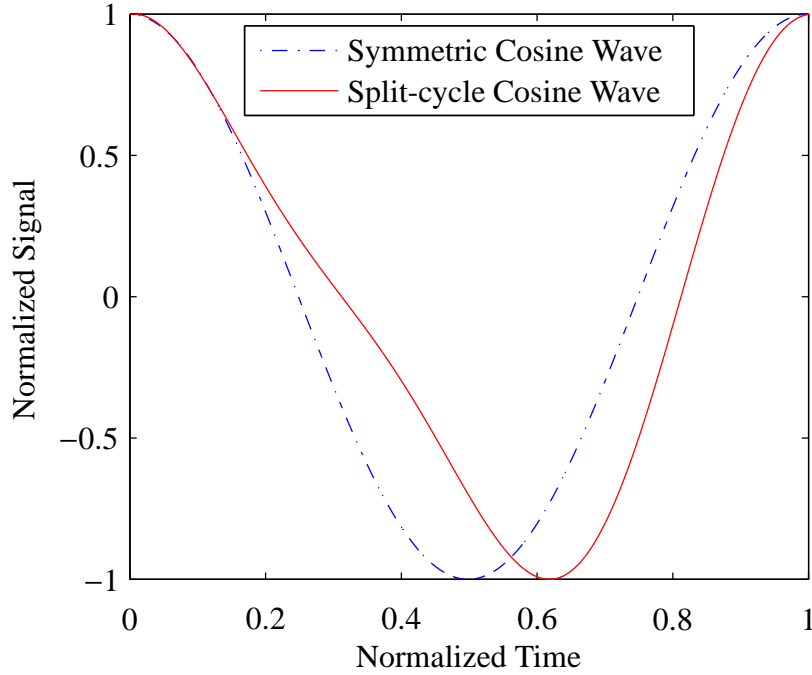


Figure 2.7: Split-cycle wing trajectory, $\tau = 0.25$

BABM control allows two piezoelectric actuators to produce forces and moments in five DOF. The piezoelectric actuators operate in one DOF, the stroke angle. The equations defining BABM were developed in reference 6. The stroke angle function, ϕ , in Equation 2.3, is used to define the wing stroke angle.

$$\phi(t) = A\{M_1(\tau) \cos[\omega t + \beta(\tau)] - M_2(\tau) \sin[2\omega t + 2\beta(\tau)]\} + \eta \quad (2.3)$$

where A is the stroke amplitude, τ is the split-cycle shift, η is the stroke bias, and ω is the flapping frequency. M_1 and M_2 are the Fourier coefficients and β is the phase shift. The first two Fourier terms provide an approximation to the split-cycle equations and provide

the title "bi-harmonic". [5, 30] M_1 , M_2 , and β are functions of the split-cycle shift and are defined by the following functions:

$$M_1(\tau) = \frac{\cos(2\tau)}{M_{\omega_n}} \quad (2.4)$$

$$M_2(\tau) = \frac{0.34 \sin(3.3\tau)}{M_{2\omega_n}} \quad (2.5)$$

$$\beta(\tau) = -2\tau - \phi_{\omega_n} \quad (2.6)$$

where M_{ω_n} is the magnitude of the wing displacement at the first system resonance, $M_{2\omega_n}$ is the magnitude of the wing displacement at twice the first system resonance, and ϕ_{ω_n} is the phase of the wing displacement at the first system resonance. [30] The introduction of the resonance terms was a result of using DHPC. BABM calculates the wing stroke angle using Equation 2.3 for one DOF; but, the wing angle of attack is not held constant. The wing angle of attack is left as a function of the aerodynamic forces on the wing, and is limited by mechanical rotation stops so that the wing does travel perpendicular to the lift vector. Future research is required to determine the optimal angle for rotation stops but the current design uses 45° .

For control, the BABM parameters are varied to produce the moments and forces required to both trim and maneuver the FWMAV. The expected forces and moments caused by varying the control parameters are listed in Table 2.4. These expectations serve as a starting point for data collection. [6]

Table 2.4: Summary of aerodynamic forces and moments caused by control variables [6]

	Insects	Berkeley	Caltech	Harvard 1	Harvard 2	AFRL 1	AFRL 2	AFIT BABM
Required Actuators	Dozens?	4	6?	3	2	3	2	2
Lift, X	Symmetric Amplitude	Symmetric Amplitude	Symmetric Amplitude	Symmetric Amplitude	Symmetric Amplitude	Symmetric Amplitude	Symmetric Amplitude	Symmetric Amplitude
Side Force, Y	?	-	-	-	-	-	Asymmetric Stroke Bias	-
Thrust, Z	?	-	-	-	-	Symmetric Split-cycle	Symmetric Split-cycle	Symmetric Bi-harmonic Split-cycle
Roll, L	Asymmetric Stroke Plane Angle & Amplitude	Asymmetric Rotation Timing	Asymmetric Stroke Plane Angle	-	-	Asymmetric Split-cycle	Asymmetric Split-cycle	Asymmetric Bi-harmonic Split-cycle
Pitch, M	?	Symmetric Amplitude & Rotation Timing	Symmetric Stroke Bias	Symmetric Stroke Bias	Symmetric Stroke Bias	Bob Weight	Symmetric Stroke Bias	Symmetric Stroke Bias
Yaw, N	Asymmetric Stroke Plane Angle & Amplitude	Asymmetric Amplitude	Asymmetric Amplitude	Asymmetric Amplitude	Asymmetric Amplitude	Asymmetric Frequency	Asymmetric Frequency	Asymmetric Amplitude

The amplitude controls the overall stroke angle of the FWMAV. It can be thought of as a scaling factor. Amplitude has units of voltage; for this research, the value of amplitude directly correlated to the voltage from the computer to the amplifier. An amplitude of 1 denotes a maximum and minimum value of the cosine wave. Therefore, a wave with an amplitude of 2 will have a maximum twice as high as a wave with an amplitude of 1. This is represented in Figure 2.8.

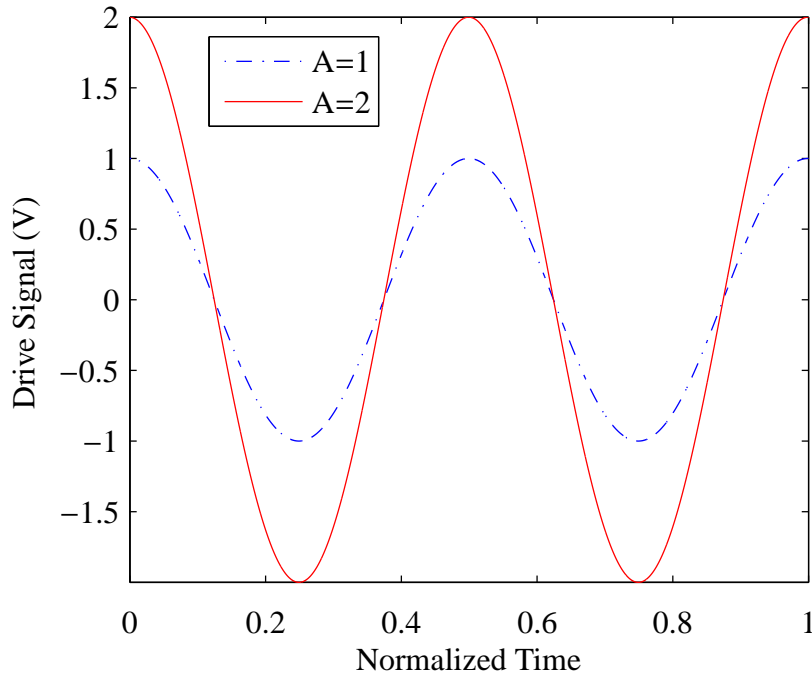


Figure 2.8: Effect of amplitude, A , on drive signal, $\tau = 0, \eta = 0$ V

The split-cycle shift controls how much the cosine wave is shifted. It has been shown that control could be achieved by limiting the split-cycle shift to a maximum of ± 0.3 and that the negative values exactly mirror the positive values. [4] The split-cycle shift effect on the drive signal is shown in Figure 2.9. Note that $\tau = 0$ is a pure sinusoid.

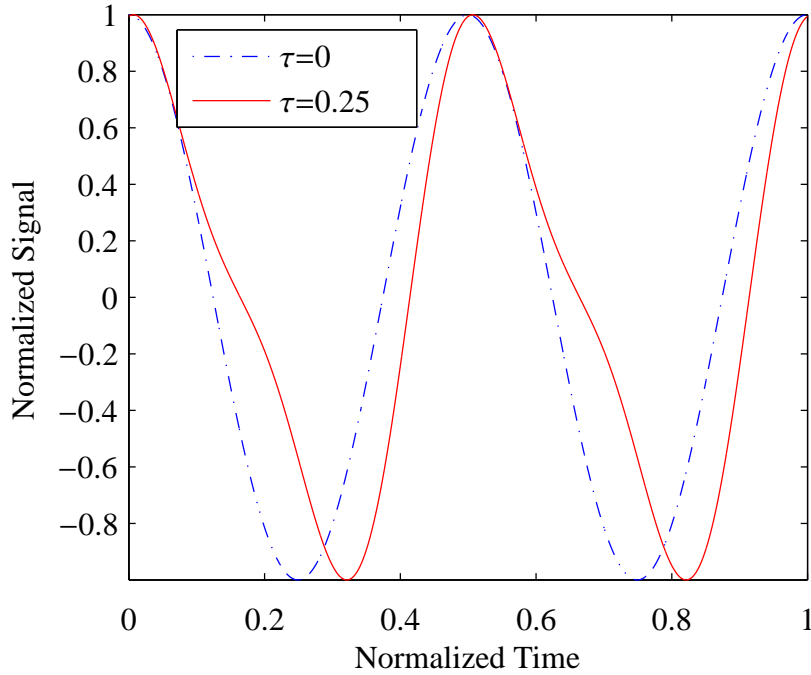


Figure 2.9: Effect of split-cycle shift, τ , on drive signal, $A = 1 \text{ V}$, $\eta = 0 \text{ V}$

While the amplitude scales the magnitude of the signal, the stroke bias adds a constant bias to the drive signal. The stroke bias is in the same units as the signal, and therefore a stroke bias of 1 shifts the signal 1 volt in the positive direction. This effect is shown in Figure 2.10.

2.5 Power

The focus on this paper is the cost of power. The power sources must also be low weight, and are, in this author's opinion, the greatest obstacle facing the future of FWMAVs. Recall that Figure 2.4 shows the mass properties of the FWMAV. The primary use of power is the locomotion of the FWMAV with secondary uses including powering the ISR sensors and communications. These secondary uses are disregarded for this research mostly due to uncertainty of future technological advancements. To power the selected

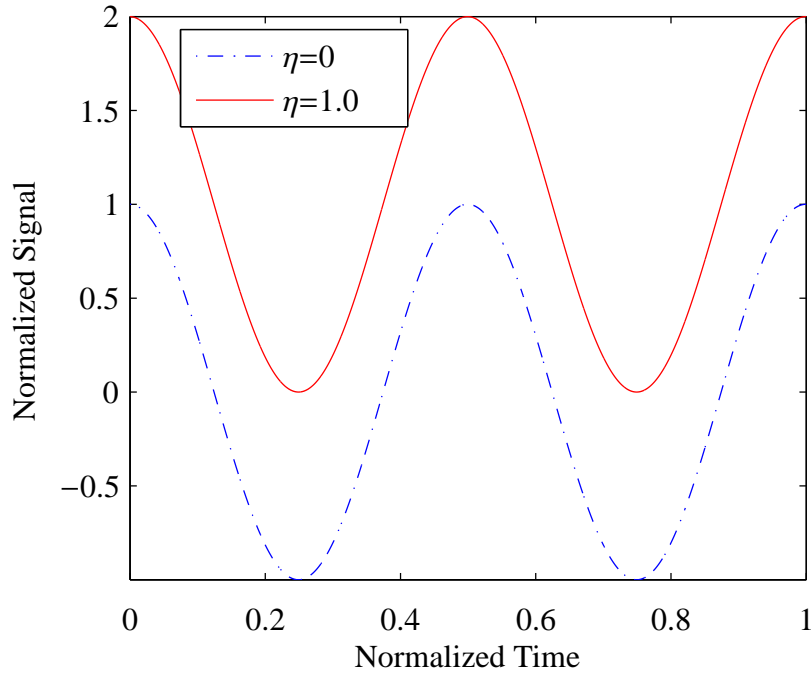


Figure 2.10: Effect of stroke bias, η , on drive signal, $A = 1 \text{ V}$, $\tau = 0$

piezoelectric actuators, the FWMAV requires high voltages and low currents. Storing power and supplying the power to the drive system will prove very challenging to the future designer. Understanding the power requirements of the BABM control scheme will help the designer optimize control logic to minimize the power requirements and save weight.

2.5.1 Power System.

The basic power system of a FWMAV will include a power supply and, due to the high-voltage required by piezoelectric actuators, a booster. Also included in the definition of a power system is the distribution network and the utilization system. [19] The piezoelectric actuator is the utilization system in the FWMAV and was discussed earlier in this chapter. The distribution network will not be discussed because the voltages and currents involved were within the realm of current wire and circuitry technology.

2.5.2 Proposed Power Boosters.

Karpelson et al. eloquently offer three techniques to achieve the high voltage/low current requirement: a boost converter/voltage multiplier hybrid, a boost converter combined with an autotransformer, and a power amplifier using a piezoelectric transformer. The following explanations appear in reference 26.

1. Hybrid Voltage Multiplier

A hybrid circuit consisting of a conventional boost converter cascaded with a switched-capacitor charge pump circuit, as shown in Figure 2.11, has been considered previously for piezoelectric microrobots and electrostatic microelectromechanical systems (MEMS) devices. Operating in a regime of high efficiency, the boost converter stage provides a moderate boost to the input voltage, while its pulsed output naturally charges up the capacitor ladder through the diodes. The charge pump multiplies the boost converter's output voltage, ideally by a factor equal to the number of charge pump stages. The maximum output power is limited by the size of the charge pump capacitors and the maximum output power of the boost converter.

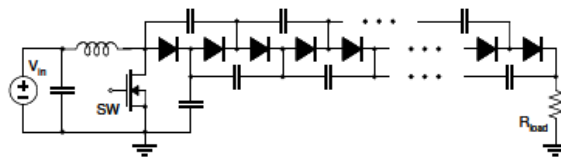


Figure 2.11: Hybrid voltage multiplier [26]

2. Converter with Autotransformer

Replacing the inductor in the standard boost converter with an autotransformer, as shown in Figure 2.12, results in a combination of the boost and flyback voltage converter topologies. Similar to the boost converter, current ramps up in the primary winding of the transformer when the switching transistor is conducting. When the switch turns off, the rectifier diode sees a combination of the input voltage, the primary winding voltage, and the secondary winding voltage, which depends on the turn ratio between the primary and secondary windings. Voltage gain is therefore determined by the duty cycle of the switching transistor and the turn ratio of the transformer. Maximum output power is limited by the current rating of the switching transistor and the transformer. For high voltage gains, this method has a much lower parts count than the hybrid converter. However, the rectifier diode and output capacitor must be rated for the output voltage. Additionally, a custom transformer may be required, since no commercial parts under 2g could be identified.

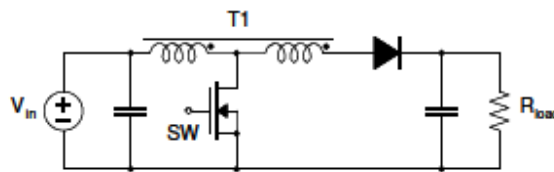


Figure 2.12: Boost converter with autotransformer [26]

3. Power Amplifier

Piezoelectric transformer (PT) have a high voltage gain ratio and high power density (up to 40 W/cm^3). Due to their simple geometries, they

scale better to small sizes than magnetic transformers and hold potential for on-chip integration. Many geometries exist with the same basic operating principle - the "primary" side of the PT excites mechanical oscillations in the piezoelectric material, while the "secondary" side generates a voltage. In order to obtain high voltage gain and efficiency, a PT has to operate close to the mechanical resonance frequency, where its electrical response can be approximated by the equivalent circuit in Figure 2.13(a). The gain of a PT is also highest at low loads, making it a good candidate for the high-voltage, low-current requirements of voltage-mode actuators. In order to reduce switching losses, as well as losses associated with charging and discharging the input capacitance of the PT, a resonant driving stage is used. Figure 2.13(b) shows the Class "E" resonant topology, selected here because it has a low number of additional components. The inductor is selected to resonate with the input capacitance C_{in} of the PT at a frequency close to the mechanical resonance frequency. The resonance transfers energy to the PT from the inductor when the switch is off. The switch is turned on again as soon as the voltage across C_{in} back down to zero. Regulation of the output voltage is achieved by varying the switching frequency. [25]

The first two options were tested by Karpelson et al. and found to be viable options for powering a FWMAV. The third option, a PT, was not able to be manufactured with sufficient voltage gain.

2.5.3 Power Supply.

During the development of other MAVs, researchers have investigated using power sources including internal combustion engines, fuel cells, micro turbines, solar cells, and

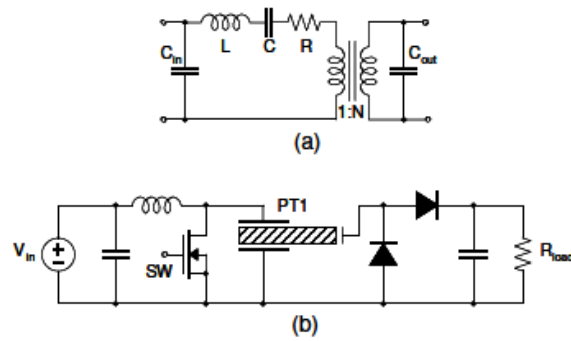


Figure 2.13: PT transformer equivalent circuit (a) and Class "E" power amplifier (b) [26]

batteries. [13, 21] Researchers have agreed that battery technology is the only power supply currently feasible for use in FWMAV by choosing batteries for their designs. [13, 21, 27] Researchers have found that flight endurance mainly depends on the battery. [46] Researchers have spent less time focused on the power applications of FWMAVs because controlled flight is still difficult and batteries are available to supply short flights for experimental use. However, before FWMAVs can be used in the field, battery technology must improve so that FWMAVs can perform longer duration missions.

2.6 Chapter Summary

The research presented in this chapter was only a small portion of the literature available on the topic of FWMAVs. Furthermore, hands-on training provided by researchers in the field was extremely beneficial. The knowledge obtained during the literature review paved the way for smooth testing and analysis, presented in Chapters III and IV.

III. Test Methodology

THIS chapter will focus on the methodology used to collect data for analysis. AFIT researchers have been working on the FWMAV project for many years and has seen many iterations of the fabrication process. This research used the most recent iteration, described in reference 39. Furthermore, a proven testing technique was previously developed for collecting the force, moment, and power data of the FWMAV. A more detailed explanation of the methods used can be found in References 3, 39, and 40.

3.1 Flapper

AFIT researchers have been developing the manufacture of engineered wings for many iterations and understanding the process was key to this research. As mentioned in Chapter II, AFIT researchers use a YSH-70A carbon fiber for the majority of structural members. The flapper tested, pictured in Figure 3.1, was constructed in multiple parts and assembled later. This flapper differs from the one that will likely be used in an operational FWMAV but serves as a good test-bed for experimentation.

3.1.1 Flapper Materials.

Few materials were used in the FWMAV construction, which simplified the manufacturing process. The flapper shown in Figure 3.1 was constructed of three main materials. The YSH-70A carbon fiber served as the main structural component. Kapton served as a flexible joint to allow for movement between carbon fiber parts. Mylar served as the wing membrane. Pyralux is a sheet adhesive that was used to bond the Kapton to the carbon fiber.

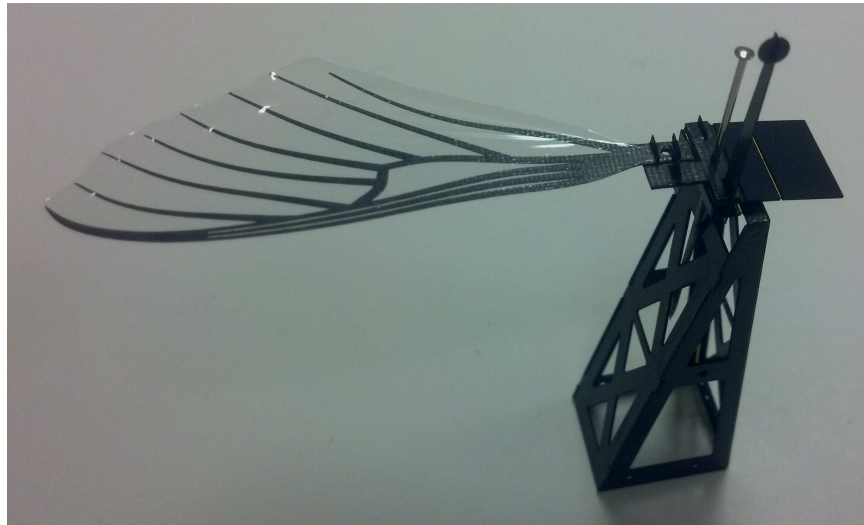


Figure 3.1: Constructed flapper

3.1.1.1 YSH-70A Carbon Fiber.

As stated above, the main structure of the flapper was made of YSH-70A carbon fiber. The carbon fiber provides an excellent stiffness-to-weight ratio. The carbon fiber was purchased in a roll of 12-inch wide "tape" that was pre-impregnated with RS-3C resin. All the fibers in the tape are oriented in the same direction. The fiber orientation provided excellent strength in one direction and allowed various layup orientations to determine the appropriate configuration. The carbon fiber was cut into appropriate size sheets to fit in the multilayer press. The sheets were oriented in the 0-90-0 configuration and inserted into the multilayer press. A multipress heats the carbon fiber to 192°C and applies 100 N/cm² for 120 minutes to cure the carbon fiber. These 3-layer carbon fiber sheets form the basis for construction.

3.1.1.2 Kapton.

As stated above, the Kapton was used as the flexible joints between carbon fiber parts. Kapton is a tough, aromatic polyimide film with a balance of properties over a

wide temperature range. [17] The Kapton used is Kapton HN 50 and 100. Kapton HN 50 is 12.7 μm thick and the Kapton HN 100 is 25 μm thick. Kapton HN 50 was used for the linkage and Kapton HN 100 was used for the passive rotation joint. Kapton HN 50 was also used as the joints for a fold-able main support structure as shown in Figure 3.1.

3.1.1.3 Mylar.

As stated above, the Mylar was used as the wing membrane. Mylar is a polyester film made from polyethylene terephthalate (PET) used for a broad array of applications. [18] Mylar was chosen for this application mainly for its superior weight qualities. It also bonds well with the RS-3C resin found in the carbon fiber.

3.1.2 Tools of Construction.

A few key apparatuses were required for the construction of the FWMAV. As expected, small hand tools such as razor blades, magnifying glasses, vises, medical harpoons, and picks were used in the assembly. These tools and their uses were semi-dependent on the assembler. Other than that, the multipress mentioned earlier, and a laser-machining center were all that was needed.

The multipress used is a LPKF MultiPress S, shown in Figure 3.2. The MultiPress S was designed to laminate multilayer composites. The user has the ability to program different profiles, consisting of different pressure, temperature, and durations settings, into the MultiPress S. [32] The MultiPress S was used to laminate the sheets of carbon fiber, to bond the Kapton to the carbon fiber via Pyralux, and to bond the Mylar to the carbon fiber.

The laser-machining center used is a LPKF Protolaser U, shown in Figure 3.3. The LPKF Protolaser U is designed to process micro-material by using an UV laser to ablate materials. [33] It allows the user the ability to program specific laser settings and tool



Figure 3.2: LPKF Multipress S

paths for repeatable results. The Protolaser U was used to cut carbon fiber and carbon fiber-Kapton layups into the parts needed for assembly.

3.1.3 Flapper Construction.

The flapper was constructed from a modular design. Parts were created and then assembled into the final product. The different parts are the structure (Figure 3.4a), the linkage (Figure 3.4b), the rotation joint (Figure 3.4c), the wing (Figure 3.4d), the passive rotation stops (Figure 3.4e), and the assembly clips (Figure 3.4f). Once the flapper was assembled, it was attached to a rapid prototyped base with a manufactured piezoelectric actuator. The piezoelectric actuator used was an 60/20/0.6 strip actuator (bimorph equivalent) purchased from Omega Piezo Technologies, Inc. since research is ongoing to optimize in-house PZT actuators.



Figure 3.3: LPKF Protolaser U

3.1.3.1 Structure and Linkage.

The structure and linkage, once constructed separately, are now constructed together to increase repeatability and reliability. The structure serves as the connection between the linkage and the mounting base. The structure was built so that the wing has room to

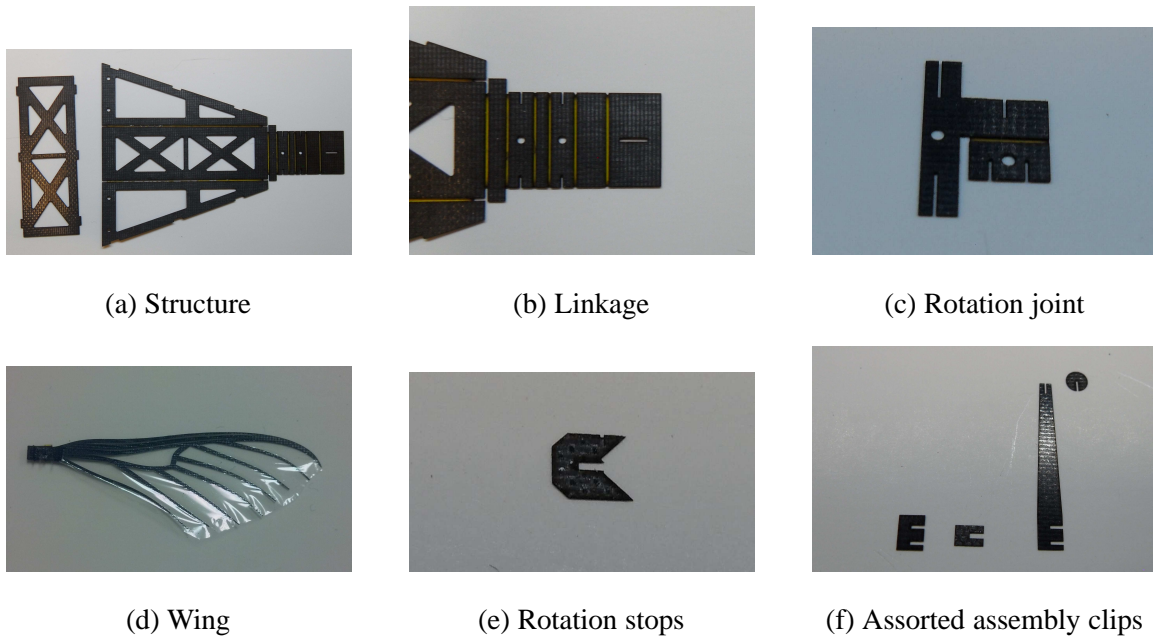


Figure 3.4: Flapper parts for assembly

actuate without interfering with the testing base. The structure was aligned in the positive Z-direction; for an operational FWMAV, the structure will likely be oriented in the negative Y-direction to provide static stability. The linkage was effectively the transmission for the FWMAV. The linkage connects the piezoelectric actuator to the rotation joint and translates the linear motion of the piezoelectric actuator to rotational motion of the wing. The linkage is a collection of four beams of different length, shown in Figure 3.5. These four lengths define the ratio between deflection and rotation. The linkage was designed to translate ± 1 mm deflection to $\pm 60^\circ$ travel with lengths of:

$$l_1 = 2.96 \text{ mm}, l_2 = 2.36 \text{ mm}, l_3 = 1.25 \text{ mm}, l_4 = 2.50 \text{ mm}.$$

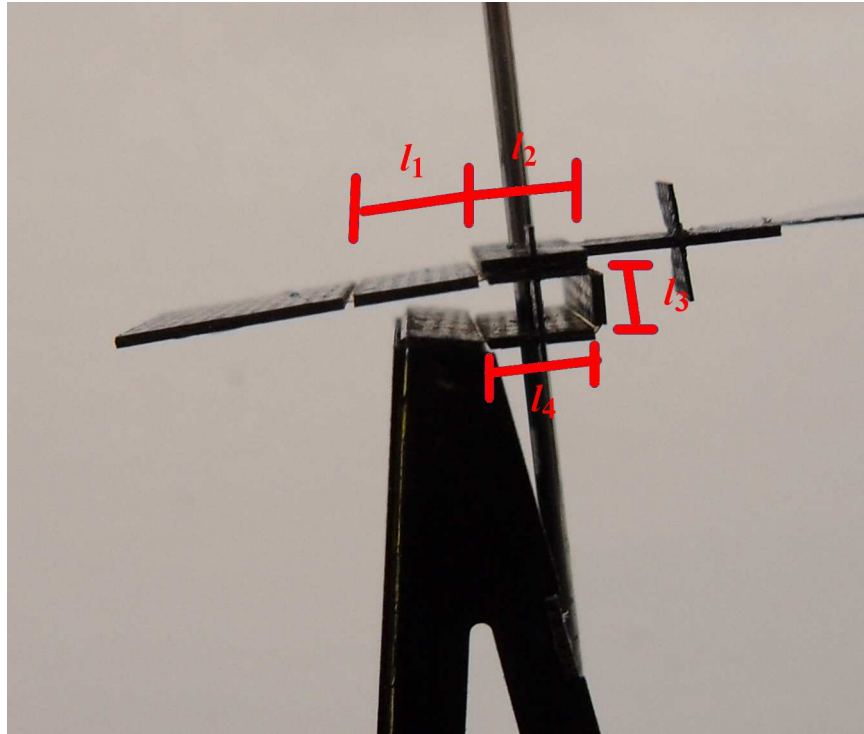


Figure 3.5: Final linkage configuration

To construct the structure/linkage, two sheets of Pyralux were applied to two 3-layer sheets of carbon fiber and were cured in the multipress at 192°C and 100 N/m^2 for 4 minutes. This step eases working with the fragile Pyralux. Kapton HN 50 was sandwiched between the two sheets of carbon fiber/Pyralux. That was loaded into the multipress and cured at 192°C and 30 N/m^2 for 60 minutes. The entire layup is shown in Figure 3.6. The final product was a large sheet that can then be machined to the proper dimensions. The final layup was loaded into the laser-machining center and the dimensions were loaded into the software. The laser-machining center follows the cutting routine and the structure/linkage was complete as shown in Figures 3.4a and 3.4b.

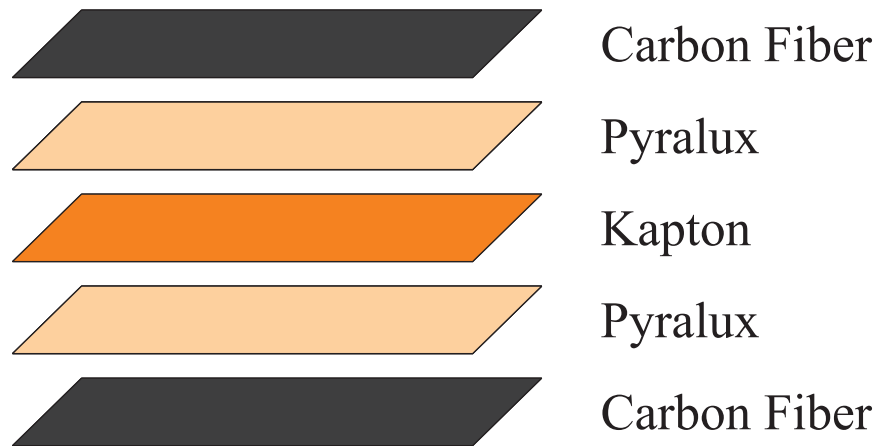


Figure 3.6: Layup for multipress to make parts for assembly

3.1.3.2 *Rotation Joint.*

The rotation joint connects the linkage to the wing, allowing the wing to rotate. The geometry of the rotation joint was designed to mimic the rotational stiffness of the *M. sexta*. The Kapton layer was also changed to match the rotational stiffness. It has also been designed to align in front of the mass and area centroids, again mimicking the *M. sexta*. All three variables resulted in a joint that closely replicates the *M. sexta*. Attached to the rotation joint are the passive rotation stops. They were simply pieces of carbon fiber that limit the amount the wing can rotate. As stated in Chapter II, rotation was limited to $\pm 45^\circ$.

The construction of the rotation joint was very similar to the construction of the structure/linkage. The main difference was the Kapton used. The rotation joint uses Kapton HN 100, which was 25 μm thick. This Kapton was used to match the rotational stiffness of the *M. sexta*. Once the entire layup was cured, it was then machined in the laser-machining center just as the structure/linkage. The complete product is shown in Figure 3.4c. The passive rotation stops were even simpler. A sheet of 3-layer carbon fiber was cut in the laser-machining center resulting in the stops shown in Figure 3.4e.

3.1.3.3 Wing.

The wing was discussed in detail in Chapter II. Much research was focused on the wing design. The result is a close match to the *M. sexta*. The construction of the wing was also simple. The wing was machined from a 3-layer sheet of carbon fiber on the laser-machining center. The result was the venation pattern of the wing. A piece of Mylar was then cured on the wing venation in the multipress at 192°C and 30 N/m² for 60 minutes. The remaining Mylar was then cut off in the laser-machining center resulting in Figure 3.4d.

A recent effort has been made to combine the wing and rotation joint. The effort has resulted in a more repeatable design. For the testing performed herein, both configurations were used. No variation in the performance was found between the non-combined and combined wing/rotation joint assemblies.

3.1.3.4 Assembly Clips.

The assembly clips were manufactured in the same way as the passive rotation stops. They come in three different configurations for different purposes. E-clips are shaped like an "E" and were used to make the square box of the linkage. The size of E-clips is dependent on the size of l_3 for the linkage. C-clips are shaped like a "C" and were used to attach the wing to the rotation joint. The last configuration was a modification of the E-clip, the extended E-clip is a taller E-clip, on which a tracking disc can be placed to measure the stroke angle using image-processing techniques. All configurations are shown in Figure 3.4f.

3.1.4 Assembly.

A systematic process for the flapper assembly can be found in Reference 39. The steps are summarized here for completeness.

1. Collect precut parts shown in Figure 3.4.
2. Fold the sides of the triangular part of structure shown in Figure 3.4a.

3. Bond the rectangular front plate of structure to the triangular part.
4. Bond the linkage shown in Figure 3.4b to the top of the assembled structure.
5. Fold the linkage into the shape shown in Figure 3.5 using a straight pin.
6. Insert and bond E-clips, Figure 3.4f, to the linkage to hold the shape.
7. Bond the passive rotation joint, Figure 3.4c, to the top of the linkage using the secured E-clips as guides.
8. Position the wing, Figure 3.4d, on the passive rotation joint using a straight pin.
9. Secure the wing to the passive rotation joint by bonding C-clips, Figure 3.4f, to the wing and passive rotation joint.
10. Attach the passive rotation stop, Figure 3.4e.
11. If an extended E-clip was used, attach the tracking disc. The assembled flapper is shown in Figure 3.1.
12. Attach assembled structure to plastic base and piezoelectric actuator.
13. Use pins to secure the structure to the base.
14. Prepare actuator tip with a thermoplastic adhesive.
15. Use heat gun to attach the linkage to the piezoelectric actuator so the wing is parallel to the floor.
16. The flapper is completed as shown in Figure 3.7.

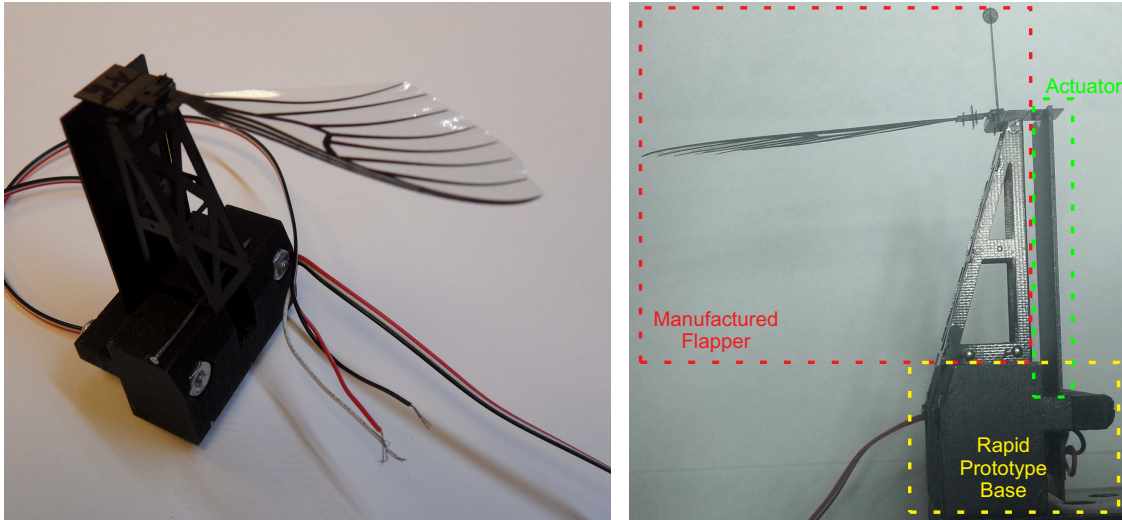


Figure 3.7: Constructed flapper with piezoelectric actuator

3.2 Experimental Setup

To test the effects of BABM on the FWMAV, a test rig was designed and constructed by AFIT. It provides the ability to prescribe an input signal to drive the stroke angle and measure resulting forces in all six DOF. The entire experimental setup is shown in Figure 3.8.

A computer running MATLAB software was connected to the equipment via a data acquisition (DAQ) module. MATLAB was used to generate a signal based on user-specified values of amplitude, split-cycle shift, and stroke bias. The signal was then sent to a voltage amplifier via the DAQ module. The signal traveled via coaxial cables to the piezoelectric actuator on the flapper. The flapper was attached to the force/moment balance, which collected data and transferred it back to the computer via the DAQ module. A displacement laser was setup to measure the tip displacement of the piezoelectric actuator. This system provided very repeatable and reliable test results.

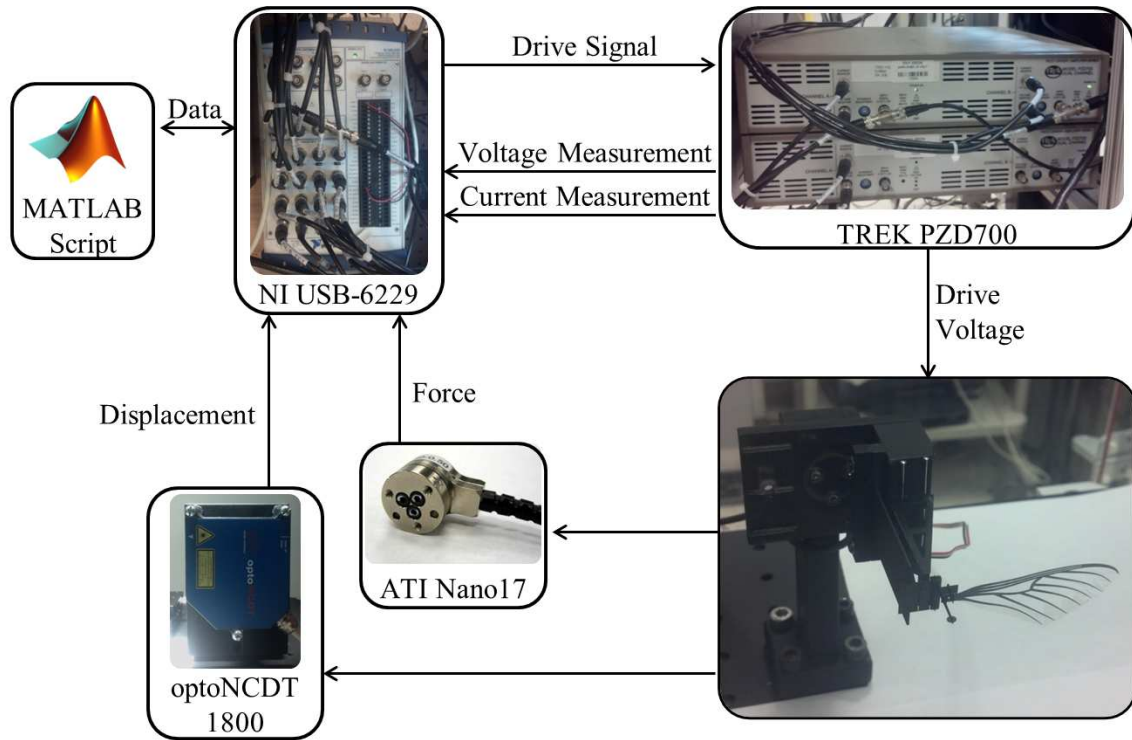


Figure 3.8: Experimental setup

The DAQ module used is a National Instrument USB-6229. This DAQ allows for inclusion of all data with 16 inputs and 4 outputs. The DAQ module also interfaces easily with the computer and MATLAB. [9] The amplifier used is Trek’s PZD700A. The PZD700A is specifically designed to drive piezoelectric actuators. It offers adjustable voltage gain by use of a potentiometer. [42] The voltage gain was set to 30 V/V for all tests in this report. The voltage and current sent to the piezoelectric actuator was directly measured from the amplifier out port. The displacement sensor used is an optoNCDT 1800. This non-contact displacement sensor uses optical triangulation to measure distance and has a measuring range of 20 mm with a resolution of 2 μm at a measuring rate of 5000 Hz. [34]

A very sensitive force/moment balance was needed to measure the small forces and moments created by the FWMAV. The force/moment balance used is an ATI Nano17 Titanium. The ATI Nano17 Titanium was the most sensitive commercially available six DOF balance to AFIT's knowledge at the time of purchase. Prior testing at AFIT has shown that this transducer is able to sense forces in the x , y , and z directions greater than 3.3 mg, 2.8 mg, and 1.91 mg. [7] The ATI Nano17 Titanium was mounted to a stand with an interface for the flapper. Previous AFIT research has validated the measured values of the force/moment balance. The balance used, like most six DOF balances, has interactions between the forces and moments. Those interactions were corrected in post processing. The data were collected by an ATI Netbox at 5000 Hz and provided to the computer for processing.

3.3 Experimental Procedure

After the entire flapper was assembled and attached to the rapid prototyped base and piezoelectric actuator, it was attached to the test rig. The first step was to determine the natural frequency of the system so that the flapper could be driven at resonance. A frequency response function (FRF) was calculated by exciting the flapper with a linearly swept chirp between 0 Hz and 100 Hz. The output of the piezoelectric actuator was recorded and the input voltage was recorded. The data was split into five samples with no overlap. A Hanning window was then applied to the data. The auto and cross power spectral density (PSD) were calculated for each of the five samples and then averaged. The FRFs were calculated from the PSDs. A sample FRF is shown in Figure 3.9. Resonant frequencies of the system were around 20-25 Hz. A state-space model of the system was obtained using an eigenvalue realization algorithm. The natural frequency of the system was determined from the FRF and the state-space model was used to generate the drive signal with BABM. The signal would last for sixty cycles, approximately three seconds.

At this point, a drive signal had been generated with specified BABM parameters specific to the system. These techniques came from Reference 3.

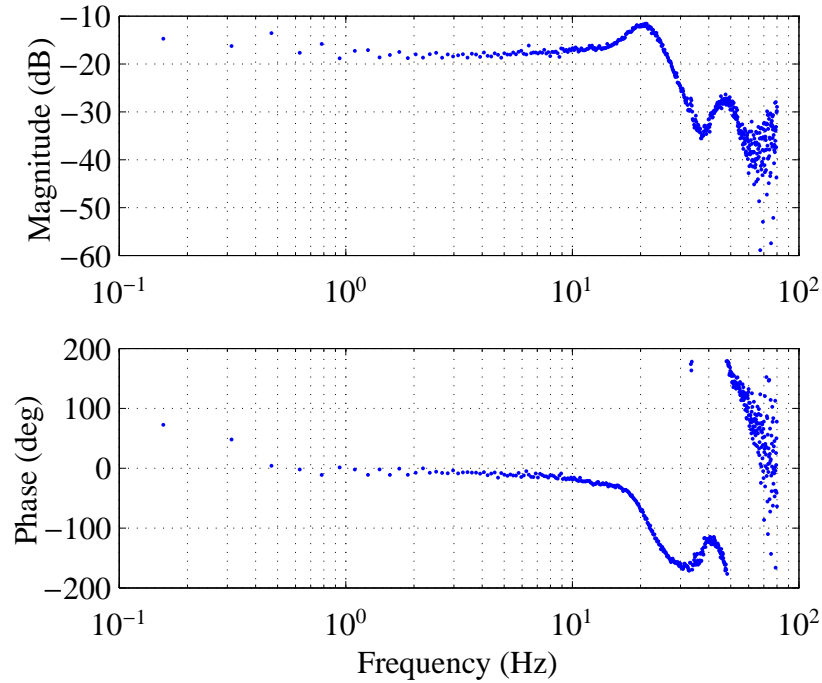


Figure 3.9: Sample FRF for a flapper

The drive signal was sent from the computer, through the amplifiers to increase the signal voltage, and on to the piezoelectric actuator to drive the flapper. The drive signal was also sent back to the DAQ module for collection and later analysis. The forces and moments from the wing motion were collected from the balance and sent to the DAQ module. The data samples were averaged and cycle average forces and moments were calculated and saved to the computer along with the raw data for later analysis.

For each sample point, at least three tests were run, consisting of sixty cycles each. Different flappers were also used to account for any manufacturing variation. Because it was difficult to identify malfunctioning piezoelectric actuators without applying a voltage,

before each test, the actuators were excited and the deflection was qualitatively assessed for proper functionality.

3.3.1 *BABM Parameters.*

A benefit of first completing single-wing flapper testing was obtaining an understanding of the BABM parameters. From examining Equations 2.3 to 2.6, some conclusions can be drawn on the values of the BABM parameters. It can be seen from Equations 2.4 and 2.6 that a split-cycle shift from $-\pi/2$ to $\pi/2$ would affect the stroke angle. From Equation 2.3, it can be seen that a stroke bias from $-\pi$ to π would affect the stroke angle. For the author's and reader's edification, these ranges were evaluated with a single-wing flapper, at least where possible. Voltage limitations on the actuator placed limitations on the BABM parameter values available for testing and ultimately for later implementation. These tests identified the limitations of the split-cycle shift originally identified by Anderson and will be discussed in Chapter IV. [4] In a dual-wing flapper, only the operationally representative ranges of the BABM parameters were used for testing.

3.3.2 *Design of Experiments.*

Critical to the analysis were any interactions between the power and the forces/moments of the flapper. A design of experiments (DOE) was made with the help of a statistical analysis program. The DOE would identify any second-order interactions not predicted between the BABM parameters and the resulting forces and moments. For the DOE, JMP was used. JMP is statistical software that gave a graphical interface to display and analyze data. [24] Two DOEs were made, one for a single flapper and one for a dual-wing flapper. They are presented below in Tables 3.1 and 3.2.

JMP provided two main services used in these analyses: the *prediction profiler* and the *screening* tool. Both tools were based off of actual data. The prediction profiler provided a trace for each of the adjustable variables, the BABM parameters, and returns predictions

Table 3.1: DOE parameters for a single-wing flapper

Amplitude, A	Split-cycle Shift, τ	Stroke Bias, η
0.5	-0.3927	-0.7854
0.5	-0.3927	0.7854
0.5	0	0
0.5	0.3927	-0.7854
0.5	0.3927	0.7854
1.5	0	0
1.5	0	-0.7854
1.5	0	0
1.5	0	0
1.5	0	0.7854
1.5	0.3927	0
2.5	-0.3927	-0.7854
2.5	0.3927	0.7854
2.5	0	0
2.5	0.3927	-0.7854
2.5	0.3927	0.7854

for each of the outputs, the power, and the forces and moments. This proved very useful in determining the relations of variables and outputs. The screening tool identified which parameter(s) had second-order effects on the outputs. This proved helpful to determine which BABM parameter had the greatest effect on power and lift. [24]

3.4 Chapter Summary

A foundation has been set to proceed with testing. This chapter was laid out to prepare the reader for Chapter IV where the results are presented.

Table 3.2: DOE parameters for a dual-wing flapper

Amplitude		Split-cycle Shift		Stroke Bias, η
Right Wing, A_R	Left Wing, A_L	Right Wing, τ_R	Left Wing, τ_L	
0	0	-0.25	-0.25	0.75
0	0	-0.25	0	0
0	0	-0.25	0.25	-0.75
0	0	0.25	-0.25	-0.75
0	0	0.25	0.25	0.75
0	1.25	0	-0.25	0.75
0	1.25	0.25	0.25	0
0	2.5	-0.25	-0.25	-0.75
0	2.5	-0.25	0.25	0.75
0	2.5	0.25	-0.25	0.75
0	2.5	0.25	0.25	-0.75
1.25	0	0	0.25	-0.75
1.25	0	0.25	-0.25	0
1.25	1.25	-0.25	-0.25	-0.75
1.25	1.25	-0.25	0.25	0.75
1.25	2.5	0.25	0	0.75
2.5	0	-0.25	-0.25	-0.75
2.5	0	-0.25	0.25	0.75
2.5	0	0	0	0.75
2.5	0	0.25	-0.25	0.75
2.5	0	0.25	0.25	-0.75
2.5	1.25	0.25	0	-0.75
2.5	2.5	-0.25	-0.25	0.75
2.5	2.5	-0.25	0.25	-0.75
2.5	2.5	0	-0.25	-0.75
2.5	2.5	0	0.25	0
2.5	2.5	0.25	-0.25	-0.75
2.5	2.5	0.25	0.25	0.75

IV. Analysis and Results

DATA collected according to the process outlined in Chapter III are presented here. This chapter follows a chronological layout, testing first a single-wing flapper and then a dual-wing flapper. Analysis techniques are presented prior to their use to prevent repeated figures and confusion. The importance of each figure is also discussed in this chapter.

4.1 Analysis

Once raw data was collected, a series of data processing techniques were applied. These techniques averaged multiple tests, generated cycle average values, and centered the moments on the center of pressure.

4.1.1 Data Processing.

The data collected by the DAQ module immediately went through post-processing in MATLAB. The data from the balance came in six columns (one for each force and moment) of voltage measurements. Tare data was removed from the data and averaged to obtain an average tare to remove from the data. The tare value was also removed from the sample data. The sample data were then passed through a balance interaction matrix to remove coupling between the sensors in the balance. The balance interaction matrix also converts the voltages measured by the balance into forces and moments. The result was sample data in nanograms and nanogram-millimeters for the entire sample. The output of the amplifier (input to the flapper) was central to this research. The data was received as voltage and current measurements in voltage. The measurements was converted to the correct units per manufacturer specifications and tare data were removed. A sample of raw data for two flap cycles is presented in Figure 4.1.

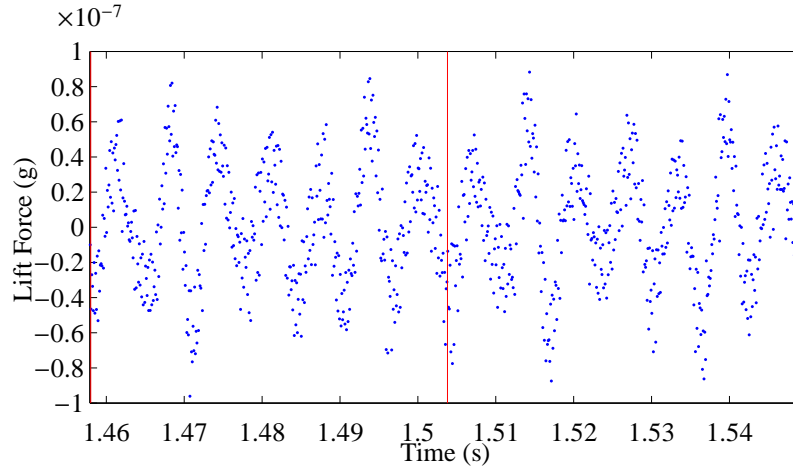


Figure 4.1: Sample of raw lift data

Since this data occurred over multiple wing cycles and there was no good way to account for instantaneous aerodynamic forces and moments that the flapping generates, cycle-averaged values for forces and moments were used. Only 80% of the collected data was used in the cycle-averaging to avoid any ramp up or down transients associated with the flapper as the sample begins and ends. The cycle-average lift for the data in Figure 4.1 is 115 milligrams. Since multiple tests were taken at each sample, the data were then averaged over the tests resulting in one value. The power was calculated from the collected voltage and current values from the amplifier. The data was passed through the Simulink model shown in Figure 4.2. The power equation for each cycle that is incorporated into the model is given by

$$P = \frac{1}{T} \sum_{t-T}^t V_{rms}(\omega_s t) I_{rms}(\omega_s t) \cos(\gamma) \Delta t \quad (4.1)$$

where P is the power, T is the cycle period, t is the instantaneous time, V_{rms} is the root mean square of the voltage data, ω_s is the sample rate, I_{rms} is the root mean square of the current data, γ is the phase angle between the current and voltage, and Δt is the time between samples. The power data was then cycle-averaged in the same manner as the force and moment data. These data sets were later analyzed.

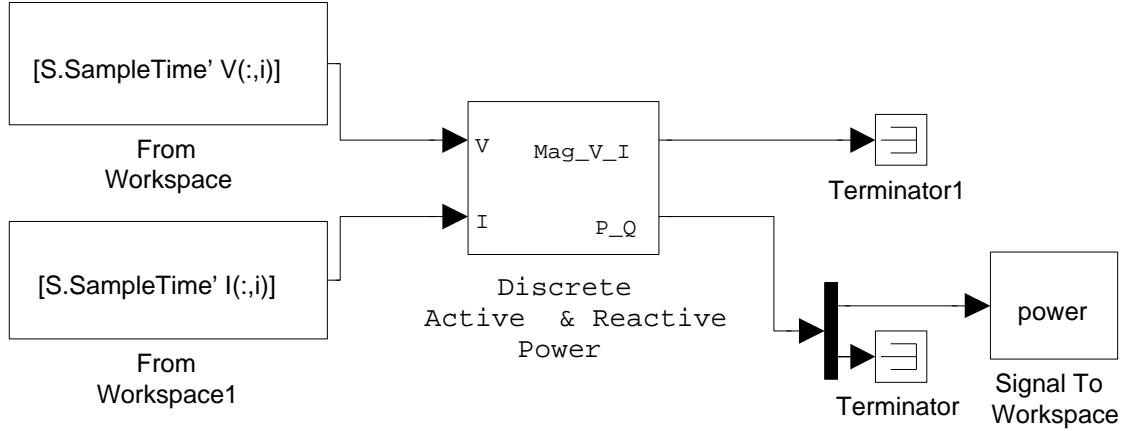


Figure 4.2: Simulink model to compute power

4.1.2 Center of Pressure.

To evaluate the true effect that the BABM parameters had on the moments generated by the flappers, the measured moments had to be calculated about the center of pressure. The nomenclature used in this section is a combination of nomenclature from References 1 and 14. Figure 4.3 shows the dual-wing flapper and the center of pressure and balance axes systems. Since the wing moves, the center of pressure for a flapping wing is varies over the stroke of the wing. The center of pressure can be approximated on the wing by

$$x_{cp} = \frac{-c}{5} \left(\frac{3b^2 + 2bR + R^2}{b^2 + bR + R^2} \right) \quad (4.2)$$

$$y_{cp} = \frac{3}{5} \left(\frac{b^3 + b^2R + bR^2 + R^3}{3b^2 + 2bR + R^2} \right) \quad (4.3)$$

$$z_{cp} = 0 \quad (4.4)$$

where c is the maximum chord length, b is the distance from the wing root to the wing break point (the point were the chord length begins to decrease) along the y -axis, and R is the length of the wingspan. [14] Figure 4.4 shows the dimensions of the wing used for

testing. These measurements resulted in $x_{cp} = -10.41$ mm, $y_{cp} = 20.16$ mm, and $z_{cp} = 0$ mm. These measurements defined the location of the center of pressure on the wing, but the center of pressure in relation to the balance was needed.

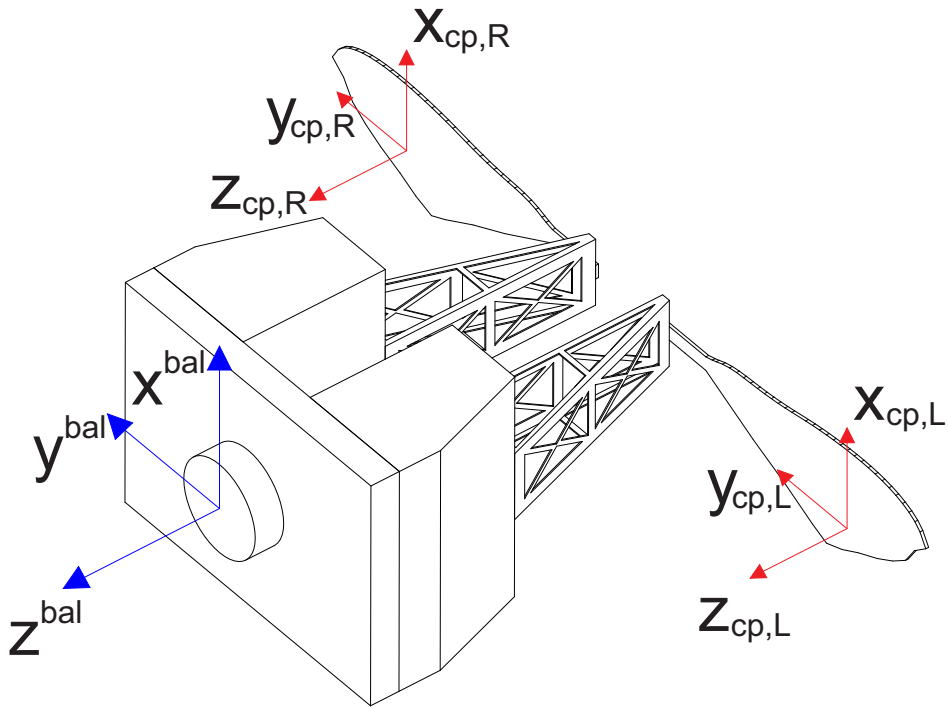


Figure 4.3: Dual-wing flapper center of pressure and balance axes

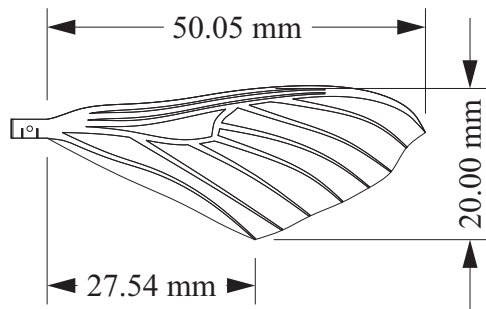


Figure 4.4: Aerodynamic dimensions of FWMAV wing

In order to find the center of pressure in relation to the balance, the instantaneous location of the wing was needed. To determine the stroke angle of the wing, the deflection of the piezoelectric actuator was used with Equation 4.5. [20, 39]

$$\theta = -\frac{\pi}{2} + \arccos \left\{ \left[l_3^2 + (l_1 + l_2 - l_4 - \delta)^2 + l_3^2 + (l_2 - l_4)^2 - l_1^2 \right] \right. \\ \left. \times \left[2 \sqrt{l_3^2 + (l_2 - l_4)^2} \times \sqrt{l_3^2 + (l_1 + l_2 - l_4 - \delta)^2} \right]^{-1} \right\} \\ + \arctan \left(\frac{l_3}{l_1 + l_2 - l_4 - \delta} \right) + \arctan \left(\frac{l_2 - l_4}{l_3} \right) \quad (4.5)$$

For the dual-wing flapper, the displacement sensor could not record deflection because the second flapping wing was obstructing it and so an approximation was used. An approximation for cycle-average displacement was developed for amplitude, split-cycle shift, and stroke bias. Figures 4.5, 4.6, and 4.7 show the actual measurements and the tests. Recall that, for this research, the amplitude voltage directly correlates to the signal sent to the amplifier. The red lines are polynomial fits of the data. The resulting approximations are

$$d_A = -0.037A^3 + 0.116A^2 + 0.153A + 0.028 \\ d_\tau = 0.002\tau - 0.002 \\ d_\eta = 0.157\eta - 0.003 \quad (4.6)$$

where $d_{\text{parameter}}$ is the displacement of the actuator. The total displacement is simply the summation of the parameter displacements. The data showed that the contribution of split-cycle shift was minimal and was therefore ignored. From the equations above, a cycle-average displacement for the actuator was calculated and used for Equation 4.5 for the dual-wing flapper. The total distance including contributions from the mounting configuration and the wing angle were summed to get an average distance between the center of pressure and the balance.

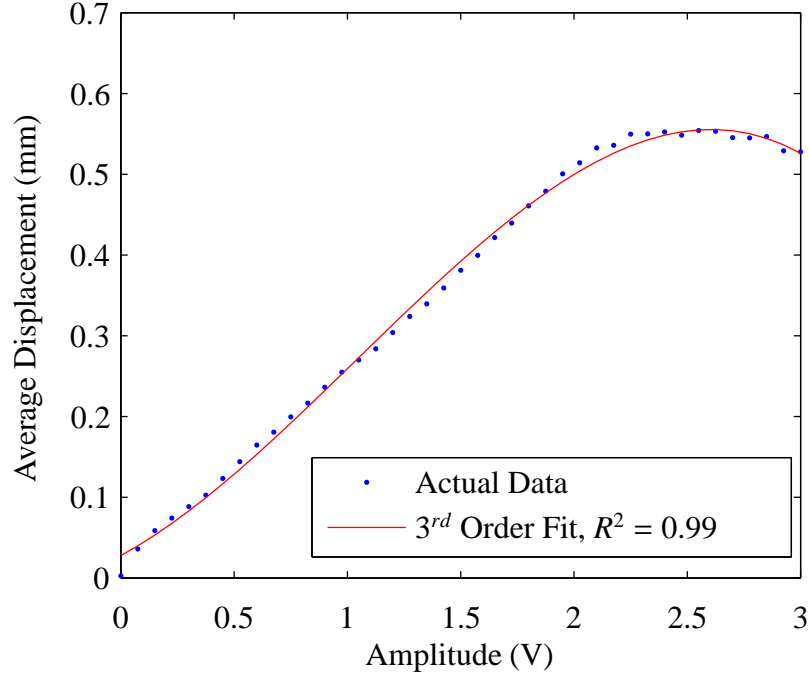


Figure 4.5: Actuator displacement vs. amplitude, $A(n)$

From this point, Equations 4.7, 4.8, and 4.9 were used to remove the lift, side force, and thrust contributions from the roll, pitch, and yaw moments.

$$L = M_x^{\text{bal}} - c_R d_{R,z} Y - c_L d_{L,z} Y - c_R d_{R,y} Z + c_L d_{L,y} Z \quad (4.7)$$

$$M = M_y^{\text{bal}} + c_R d_{R,z} X + c_L d_{L,z} X - c_R d_{R,x} Z - c_L d_{L,x} Z \quad (4.8)$$

$$N = M_z^{\text{bal}} + c_R d_{R,x} Y + c_L d_{L,x} Y + c_R d_{R,y} X - c_L d_{L,y} X \quad (4.9)$$

where L , M , and N are the roll, pitch, and yaw moments respectively; M_i^{bal} is the balance measured moment about the i -axis; c_R and c_L are the contribution factors of the right and left wing respectively; $d_{R,i}$ and $d_{L,i}$ is the distance to the center of pressure along the i -axis to the right and left wing respectively; and, X , Y , and Z are the axial forces. The contribution factor accounted for the difference in amplitude between the left and right wing and were

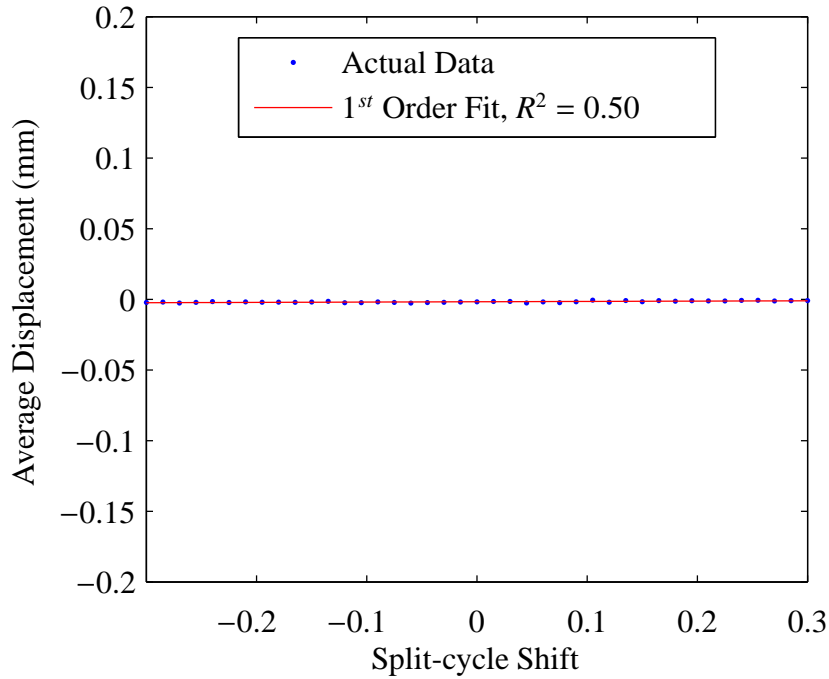


Figure 4.6: Actuator displacement vs. split-cycle shift, $\tau(n)$

calculated from

$$c_R = \frac{A_R}{A_R + A_L} \qquad c_L = \frac{A_L}{A_R + A_L}$$

For example, when the amplitudes were symmetric, the contributions were each 0.5 and half the force was attributed to the left wing and half the force was attributed to the right wing. These calculations were performed at each sample point and then cycle-average values were calculated as described in Chapter III.

A sample of the results of correcting the moments is shown in Figure 4.8. These data points were obtained by varying the amplitude of the right wing. The resulting data from that test is shown in Figure 4.29. The pitch moment about the balance closely followed the trend of the lift data, which makes sense because it was the largest force with the

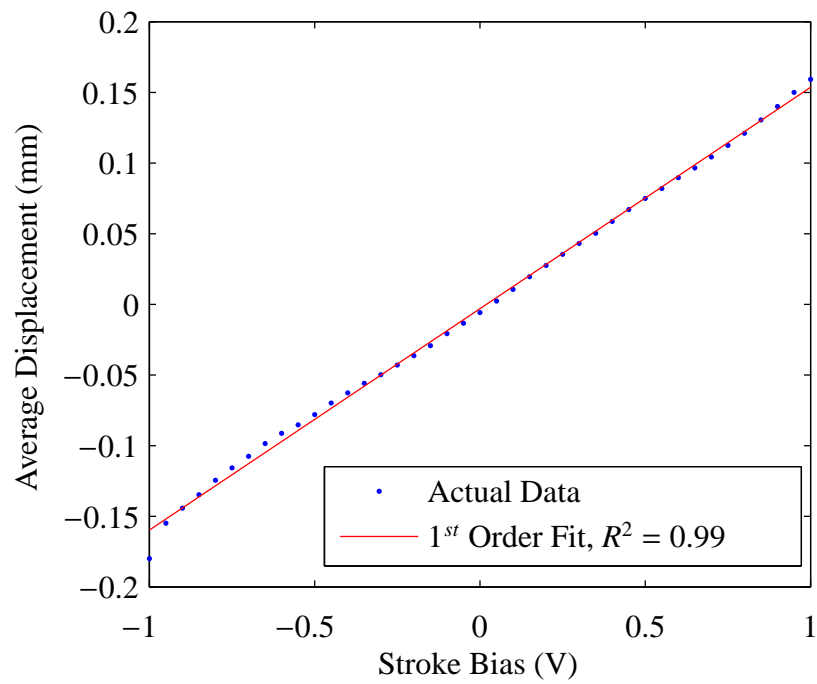


Figure 4.7: Actuator displacement vs. stroke bias, $\eta(n)$

largest moment arm. Moving the moment to the center of pressure provided moments that represent the FWMAV in free flight.

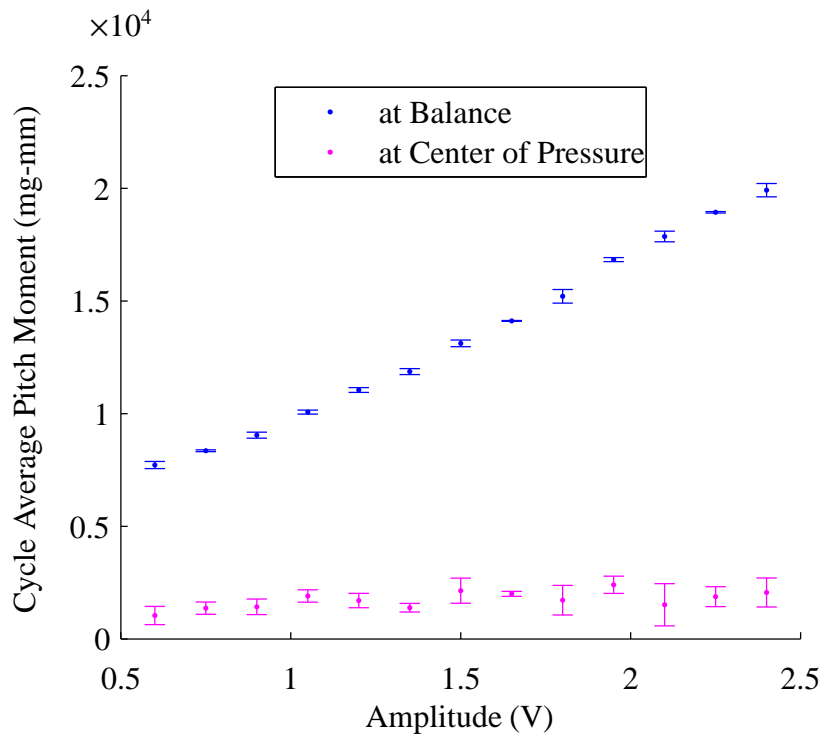


Figure 4.8: Measured pitch moment correction to center of pressure

4.2 Single Wing Flapper

The single-wing flapper was used to investigate the effects of power on the three BABM parameters independently. The tests were also used to familiarize the author with the BABM control theory. Thirty-five test matrices were evaluated on the single-wing flapper resulting in 879 test cases of data. Some data sets were not used because analysis revealed various errors such as broken actuators or malfunctioning equipment. In all, approximately 275 test cases were kept for analysis. It is obvious from the number of tests that there was a steep learning curve. For the single-wing flapper forces and moments, only the lift, thrust, and pitch are shown because they can be correlated to a dual-wing flapper configuration. The side force, roll, and yaw of single-wing flapper are not correlatable to the results of a dual-wing flapper. Table 4.1, a partial reproduction of Table 2.4 in Chapter II, served as a basis for comparison to the forces and moments generated.

Table 4.1: Baseline of aerodynamic forces and moments caused by BABM parameters [6]

Lift, X	Symmetric Amplitude, $A_L = A_R$
Side Force, Y	-
Thrust, Z	Symmetric Bi-harmonic Split-Cycle, $\tau_L = \tau_R$
Roll, L	Asymmetric Bi-harmonic Split-Cycle, $\tau_L \neq \tau_R$
Pitch, M	Symmetric Stroke Bias, $\eta_L = \eta_R$
Yaw, N	Asymmetric Amplitude, $A_L \neq A_R$

4.2.1 Amplitude.

The first test performed varied the amplitude of the stroke angle from the range of zero to three. Of course, with zero amplitude the flapper did not flap. At an amplitude

of three, the wing began to interact with the structure. For those reasons, only data from $A = 0.5 \rightarrow 2.5$ are presented here.

Figure 4.9 shows the change in the cycle average power as a function of the amplitude. The curve follows an exponential relation. Reference 31 shows that the power requirements of amplitude follow a linear path, but that research was performed over a smaller range. Over the range most likely to be used, $A = 1.5 \rightarrow 2.5$, amplitude was linear to the power requirements.

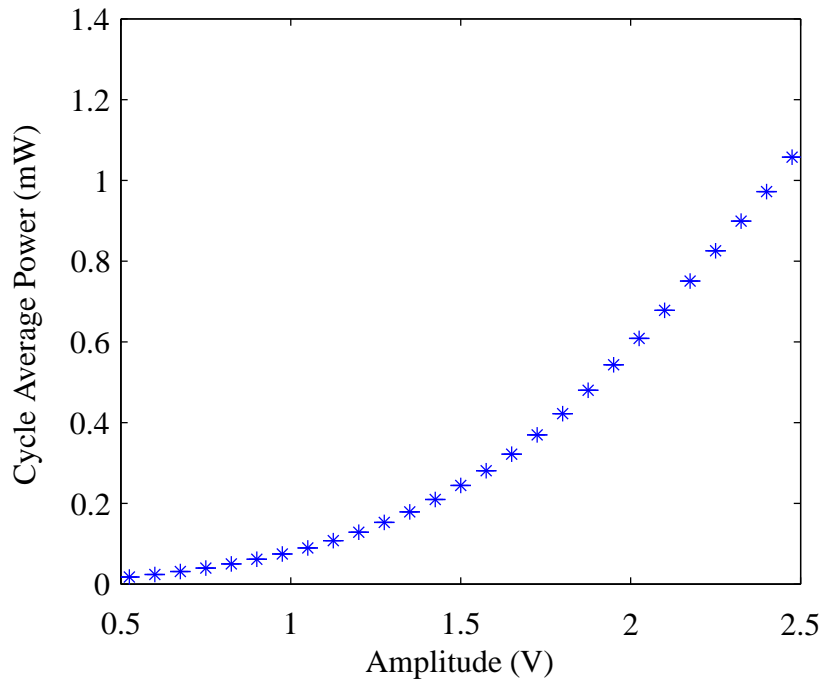


Figure 4.9: Power vs. amplitude, $A(n)$, $\tau = 0$, $\eta = 0$ V

Figure 4.10 shows the forces and moments as a function of the amplitude. Amplitude affected the lift the greatest, which agrees with Table 4.1 for the case of symmetric amplitude. By comparison, the thrust was insignificant compared to the lift generated.

There also seemed to be little relation between amplitude and thrust when the error bars were considered. Amplitude also greatly affected the pitch moment of the FWMAV.

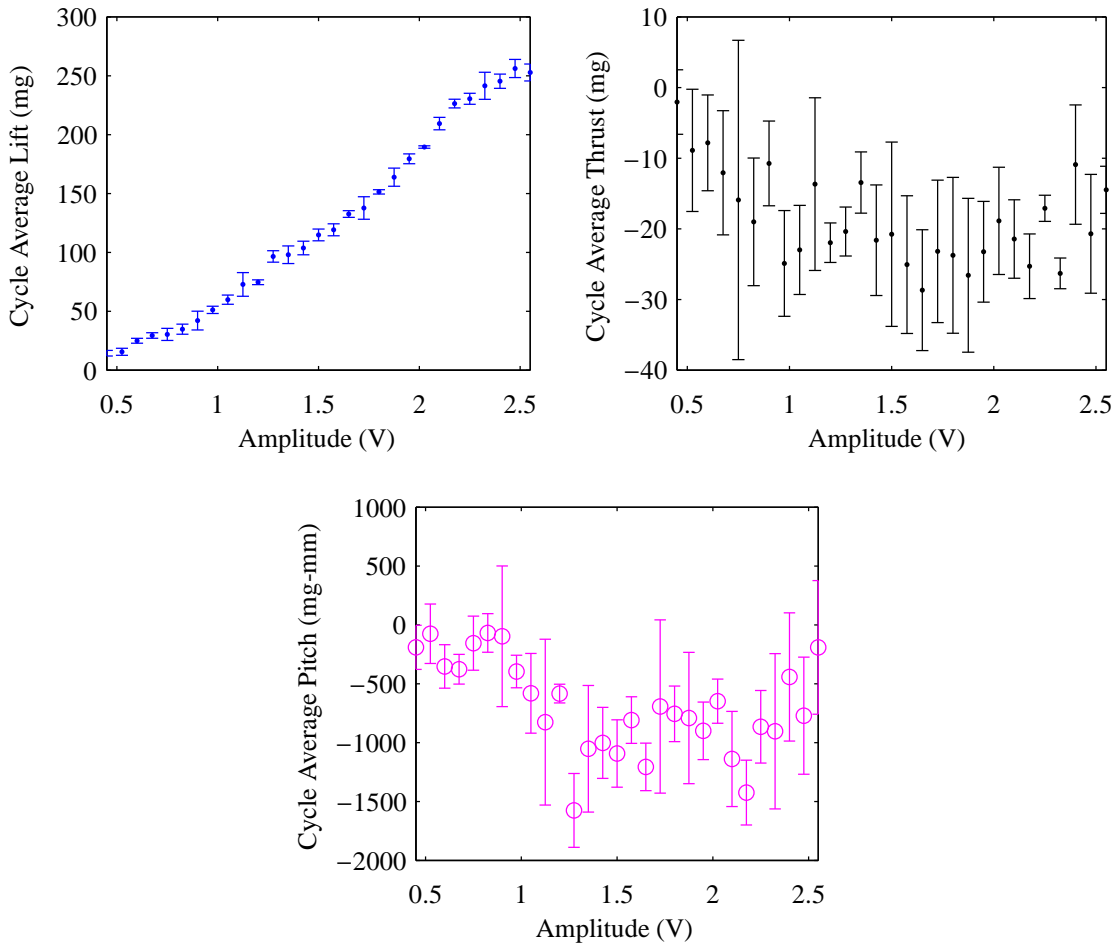


Figure 4.10: Forces and moments about the balance center vs. amplitude, $A(n)$, $\tau = 0, \eta = 0$ V

Plots for the ratio of power to lift as a function of parameter were also generated. For this figure and similar figures, keep in mind that a smaller number is preferred. A value of $A = 1$ served as a baseline of comparison for the single-wing flapper. Figure 4.11 shows the relation between power and lift as a function of the amplitude. The data showed that

increasing the amplitude resulted in more power per lift, or the power requirement rose faster than the lift provided.

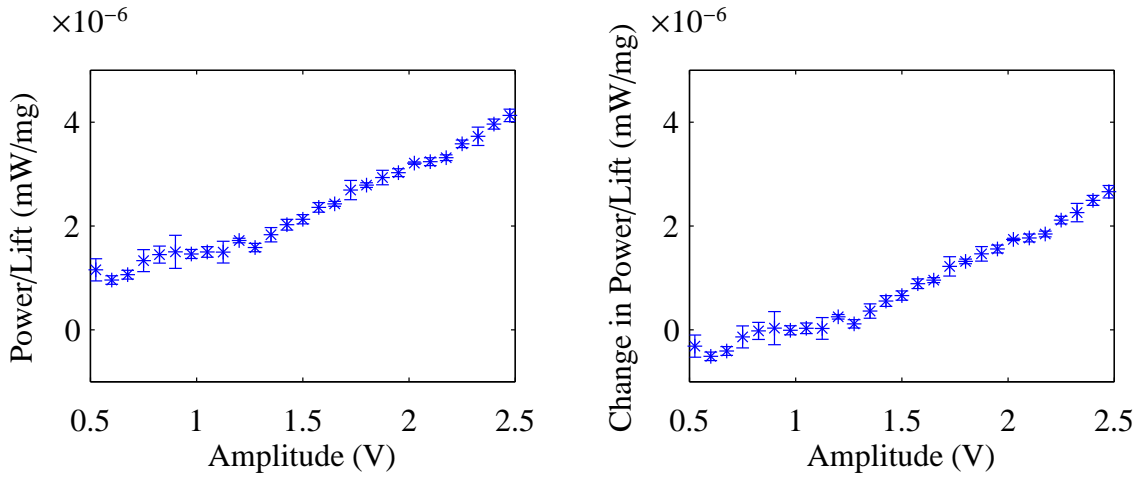


Figure 4.11: Power per lift vs. amplitude, $A(n)$, $\tau = 0$, $\eta = 0$ V

4.2.2 Split-cycle Shift.

For the split-cycle shift and the stroke bias, power was evaluated as a change in power from the case with zero split-cycle shift and stroke bias. As stated earlier, a split-cycle shift of ± 0.3 is sufficient for control, but for the author's edification, split-cycle was evaluated from $-\pi/2$ to $\pi/2$. The results are shown in Figure 4.12. A clear spike in power could be seen that correlated to $\pi/4$. This could more accurately be seen when a cosine with split-cycle shift of $\pi/4$ was compared to a symmetric cosine wave, shown in Figure 4.13. A split-cycle shift of $\pi/4$ changes the frequency of the cosine wave causing the wing to flap faster drawing more power.

Figure 4.14 shows change in power as a function of the split-cycle shift for a more reasonable range. One could see that in the range of $\tau = -0.3 \rightarrow 0.3$, the split-cycle shift was inversely related to the change in power. In comparing the ordinate to the ordinate in

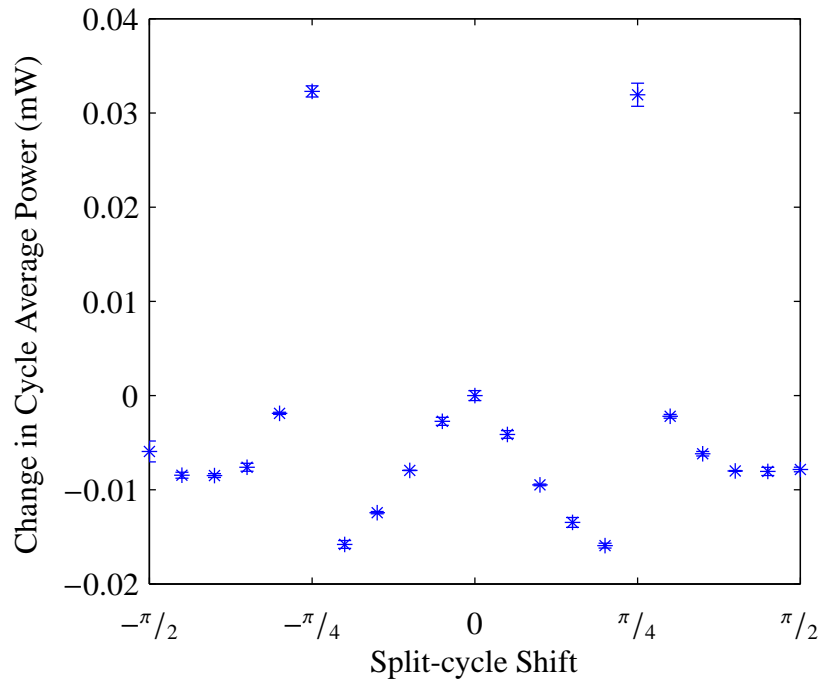


Figure 4.12: Power vs. split-cycle shift, $\tau(n)$, $A = 1$, $\eta = 0$ V

Figure 4.9, it can be observed that the change in power was multiple orders of magnitude less than the overall power. It is also important to note that the relation was symmetric about zero split-cycle shift. The symmetry will be important when designing a controller.

Figure 4.15 shows forces and moments as a function of the split-cycle shift. These tests were performed with an amplitude of one. With no split-cycle shift, the flapper should produce a lift of approximately 58 mg, a thrust of approximately -23 mg, and a pitch of approximately -300 mg-mm (from Figure 4.10). These values match closely with the values in Figure 4.15. Furthermore, the lower power requirements of split-cycle shift were manifested as a loss of lift and pitch control. It appears that split-cycle shift has little effect on the thrust, which remains at much lower values than the lift. This did not agree with the predictions in Table 4.1.

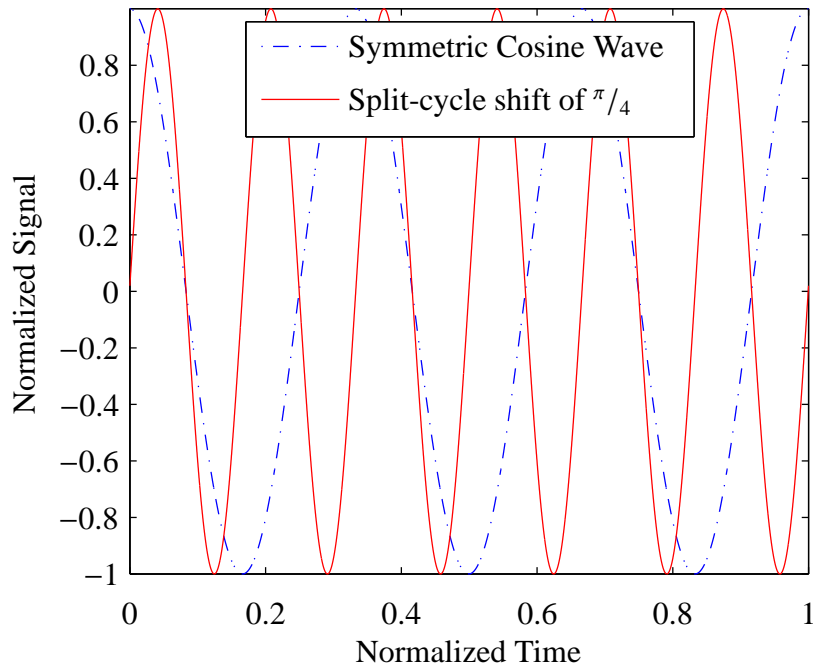


Figure 4.13: Drive signal with a split-cycle shift of $\pi/4$

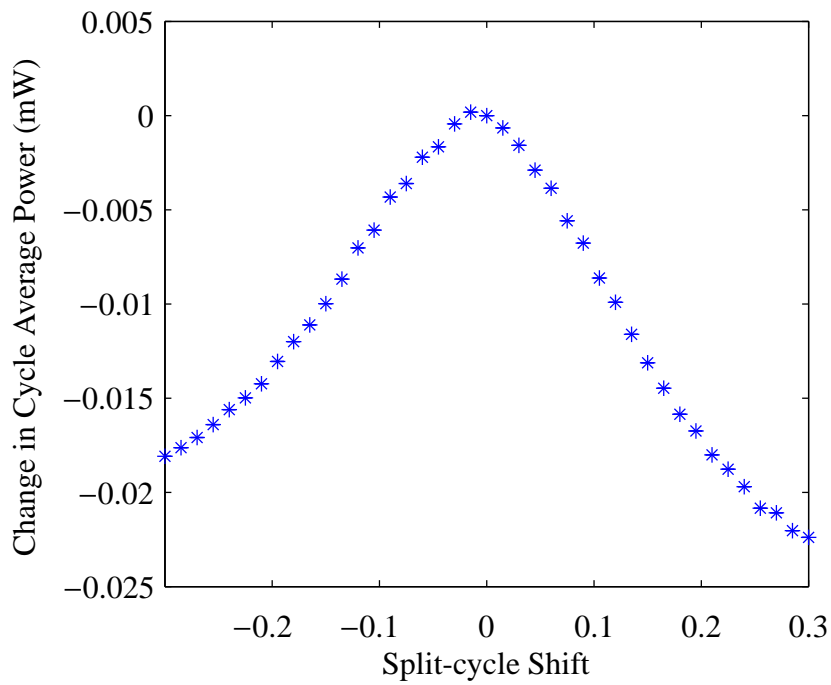


Figure 4.14: Power vs. split-cycle shift, $\tau(n)$, $A = 1$, $\eta = 0$ V

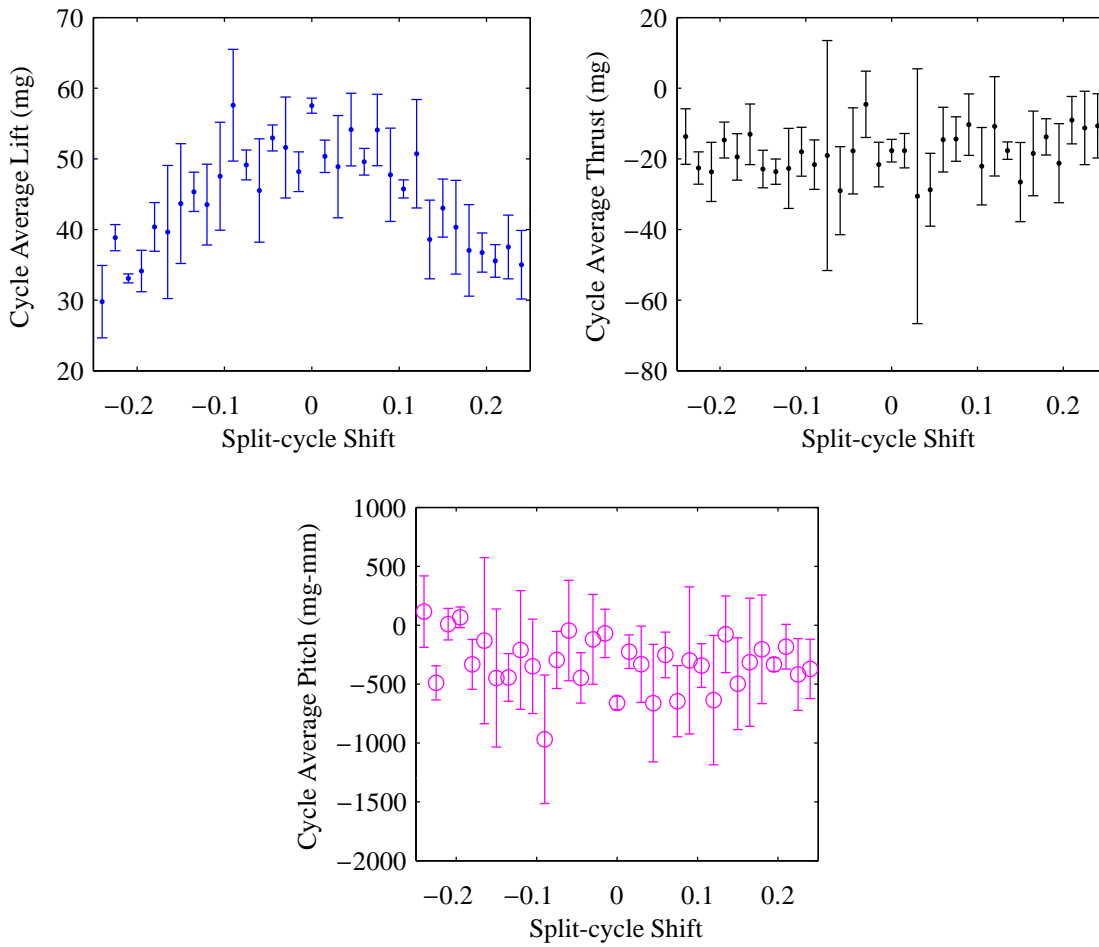


Figure 4.15: Forces and moments about the balance center vs. split-cycle shift, $\tau(n)$, $A = 1, \eta = 0 \text{ V}$

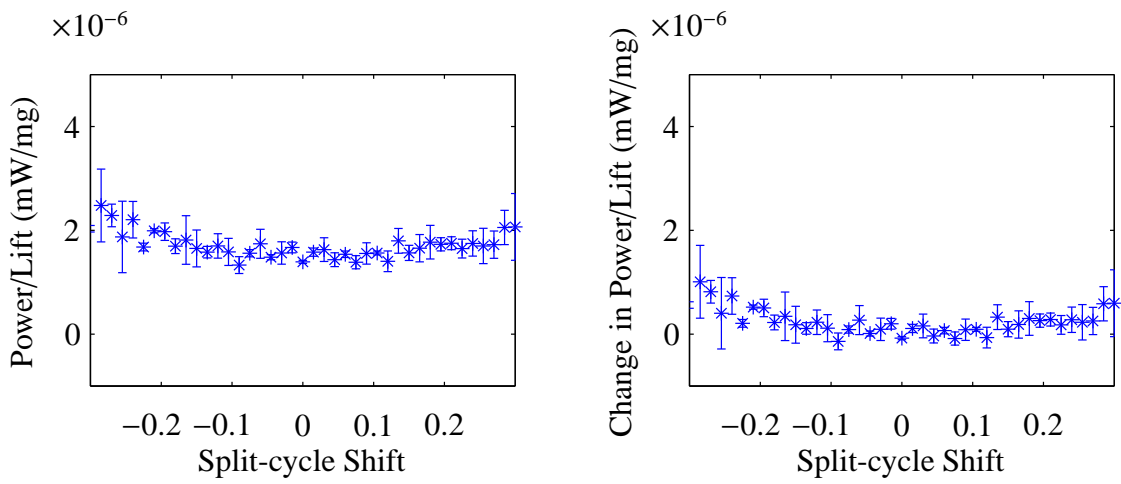


Figure 4.16: Power per lift vs. split-cycle shift, $\tau(n)$, $A = 1$, $\eta = 0$ V

Figure 4.16 shows the relation between power and lift as a function of the split-cycle shift. Note that the range of the ordinate for the change in power per lift is an order of magnitude lower than that of Figure 4.11. The data showed that increasing the split-cycle shift resulted in more power per lift. Since additional split-cycle shift resulted in lower power requirements, the increasing power per lift indicates that the lift produced decreased more rapidly than the power requirements.

4.2.3 Stroke Bias.

Stroke bias was evaluated from -1 to 1 for a single-wing flapper. These tests were also performed with an amplitude of one. Greater values of stroke bias caused the wing to interfere with the structure. The data showed that the power requirements of stroke bias were not symmetric about zero, as shown in Figure 4.17. To ensure that this was not an effect of the bimorph nature of the piezoelectric actuator, the test was performed in reverse order. Figure 4.17 also shows the data from that test. The data showed that the results were not a function of the testing order but rather that the power did in fact decrease as stroke bias increased. This is counter-intuitive and is explained in detail later when the dual-wing flapper results are presented. It is important to note that the change was on the order of 1% of the total power. This information will be very useful to the control designer.

Data was also collected for the effect that stroke bias had on forces and moments. Figure 4.18 shows that data. Recall that an amplitude of 1 would supply lift of approximately 58 mg, thrust of approximately -23 mg, and pitch moment of approximately 3100 mg-mm (from Figure 4.10). The stroke bias had a detrimental effect on lift. The stroke bias did not have an effect on the thrust. Stroke bias did affect the pitch moment, reducing the pitch moment by approximately 130 mg-mm as the stroke bias was increased or decreased to 0.75 as indicated by a best fit curve. These results agreed with the prediction for symmetric stroke bias in Table 4.1.

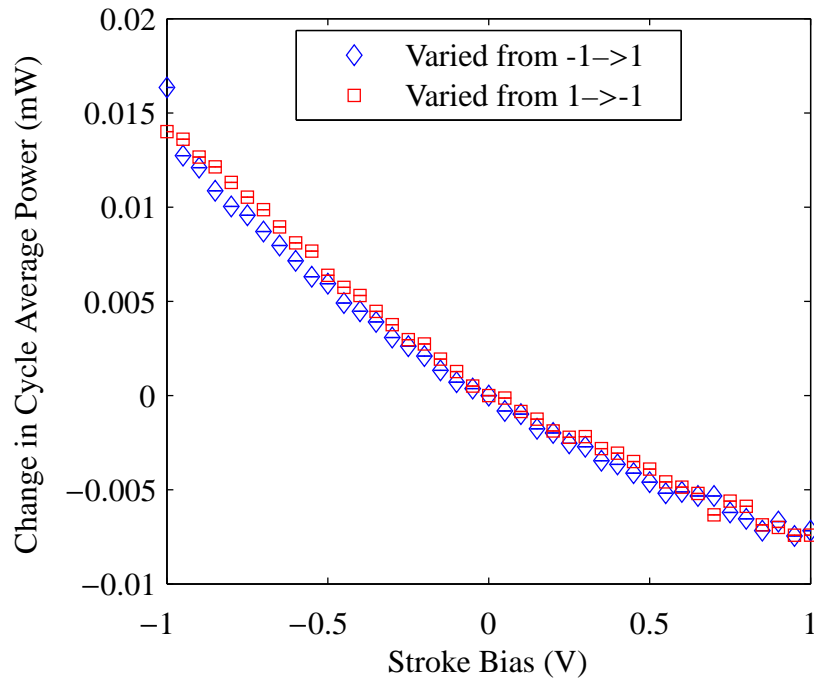


Figure 4.17: Power vs. stroke bias, $\eta(n)$, $A = 1$, $\tau = 0$

Figure 4.19 shows the relation between power and lift as a function of the stroke bias. Again, note that the range of the ordinate for the change in power per lift is an order of magnitude lower than that of Figure 4.11. The data showed that increasing the stroke bias resulted in less power per lift, but at smaller magnitudes than amplitude and split-cycle shift.

4.2.4 Design of Experiments.

Figure 4.20 shows the results from the DOE run accomplished using Table 3.1. The data showed the correlation between the three BABM parameters and the four measurements: power, lift, thrust, and pitch moment. The blue dashed lines represent confidence intervals to one standard deviation. The importance of the parameter can be assessed by the slope of the relation. Figure 4.20 also places all three parameters on the

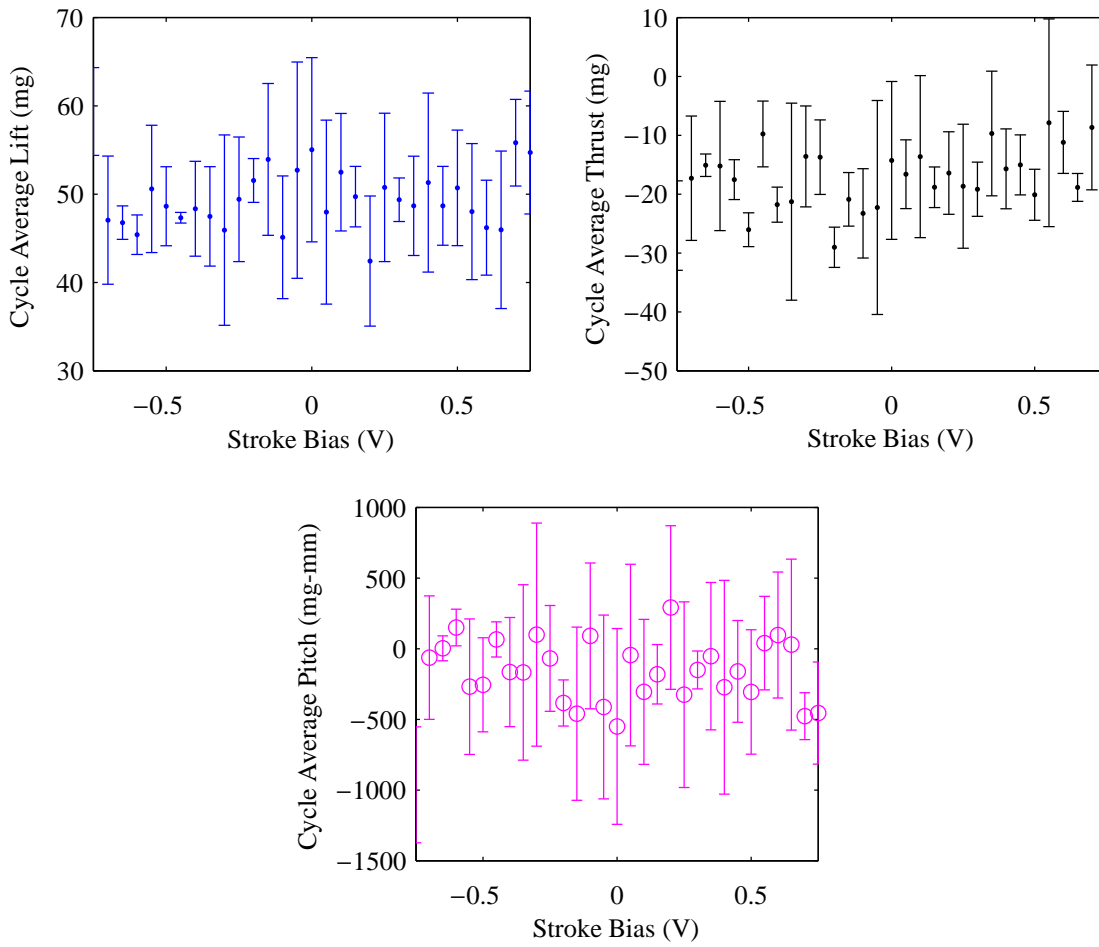


Figure 4.18: Forces and moments about the balance center vs. stroke bias, $\eta(n)$, $A = 1$, $\tau = 0$

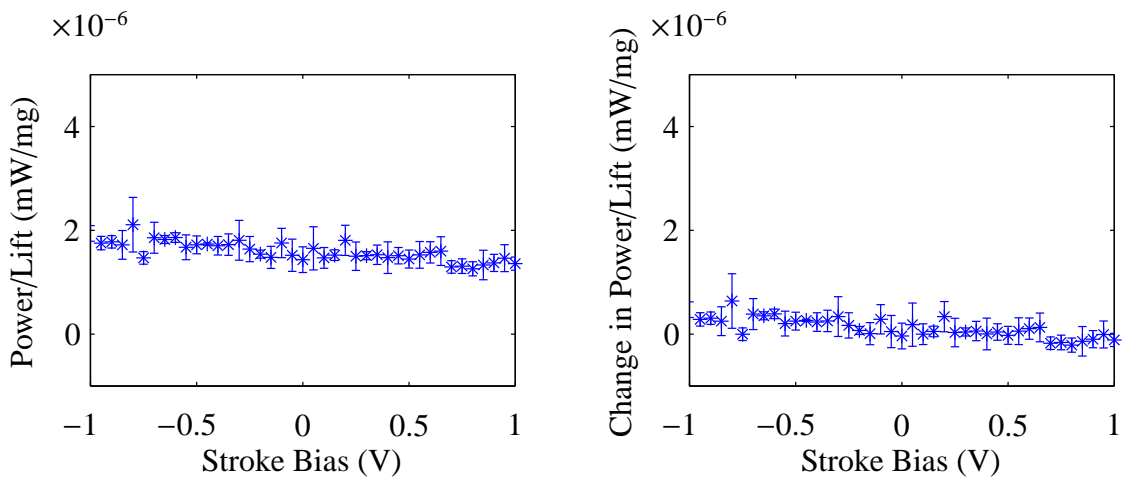


Figure 4.19: Power per lift vs. stroke bias, $\eta(n)$, $A = 1$, $\tau = 0$

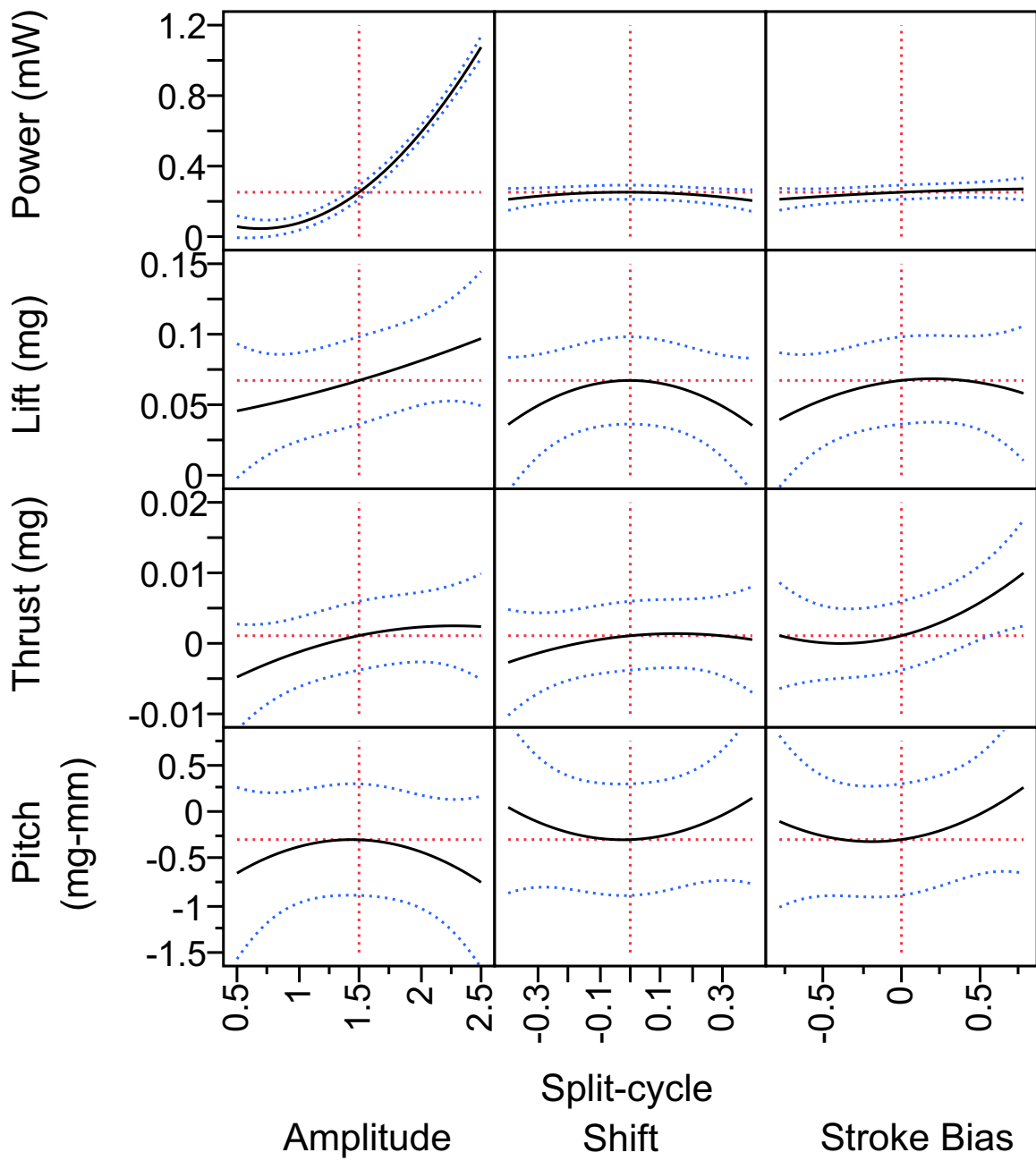


Figure 4.20: DOE results for single-wing flapper

same scale. It was easy to determine that amplitude had the greatest effect on power. The data also showed that the stroke bias had the greatest effect on thrust, unlike predicted in Table 4.1. The data show that symmetric split-cycle shift may be most useful to control the pitch moment.

Figures 4.21 and 4.22 show the relations for the power and lift. The bars are scaled estimates normalized between -1 and 1 where a negative relationship is detrimental to the output. The blue lines on the charts mark a value of 0.2 indicating a strong relationship. The figures also show secondary interactions. The data agreed that amplitude had the strongest effect on power. The data also agreed that amplitude had the greatest effect on lift but a strong secondary interaction appeared between amplitude and stroke bias squared. This indicates that changes in amplitude and large changes in stroke bias may detrimentally affect lift in a significant way.

4.2.5 Randomized Verification.

In order to ensure that the testing methodology was sound prior to moving forward with dual-wing flapper testing, data were collected for randomly selected values of the BABM parameters. Figures 4.23, 4.24, and 4.25 show the results of those tests. The data was in close correlation with the other data. These results helped verify that the data for the single-wing flapper was collected and analyzed properly.

Parameter(s)

- Amplitude
- Stroke Bias
- Split-cycle Shift
- Amplitude*Amplitude
- Amplitude*Stroke Bias
- Stroke Bias*Stroke Bias
- Amplitude*Split-cycle Shift
- Stroke Bias*Split-cycle Shift
- Split-cycle Shift*Split-cycle Shift
- Amplitude*Amplitude*Stroke Bias
- Amplitude*Stroke Bias*Stroke Bias
- Amplitude*Amplitude*Split-cycle Shift
- Amplitude*Stroke Bias*Split-cycle Shift

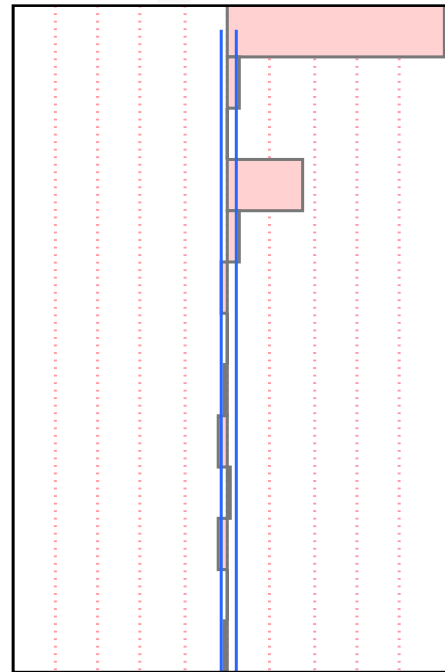


Figure 4.21: BABM parameter effects on power for a single-wing flapper

Parameter(s)

- Amplitude
- Stroke Bias
- Split-cycle Shift
- Amplitude*Amplitude
- Amplitude*Stroke Bias
- Stroke Bias*Stroke Bias
- Amplitude*Split-cycle Shift
- Stroke Bias*Split-cycle Shift
- Split-cycle Shift*Split-cycle Shift
- Amplitude*Amplitude*Stroke Bias
- Amplitude*Stroke Bias*Stroke Bias
- Amplitude*Amplitude*Split-cycle Shift
- Amplitude*Stroke Bias*Split-cycle Shift

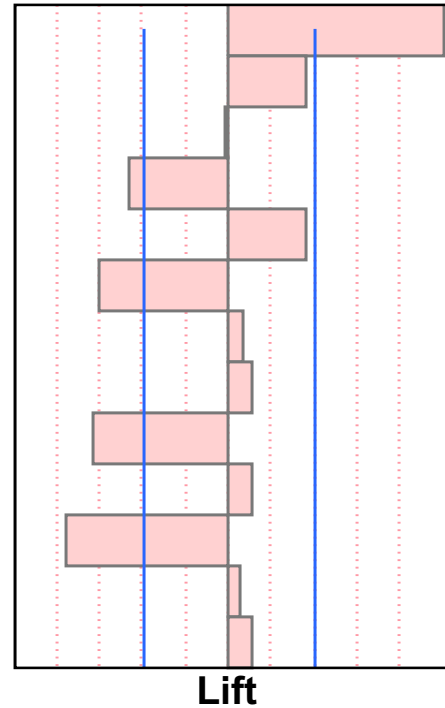


Figure 4.22: BABM parameter effects on lift for a single-wing flapper

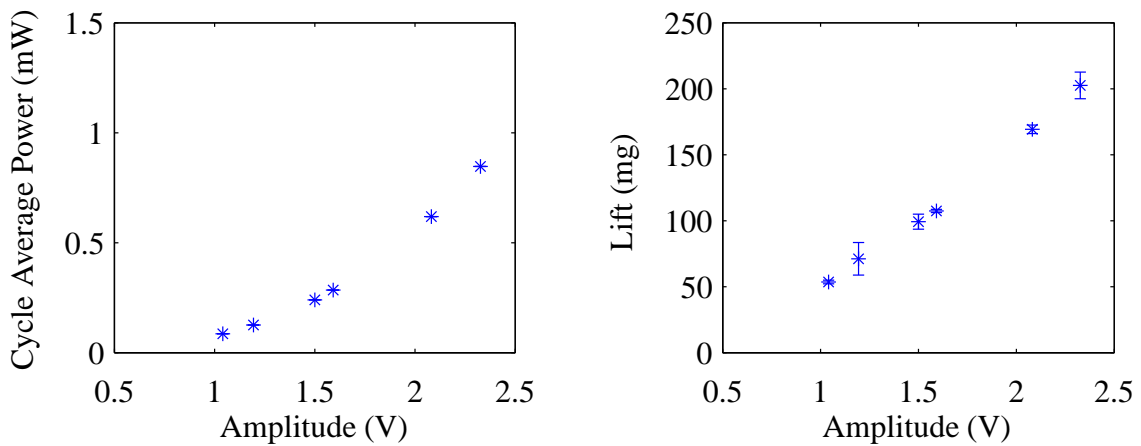


Figure 4.23: Power vs. amplitude, $A(n)$, random sampling, $\tau = 0, \eta = 0$ V

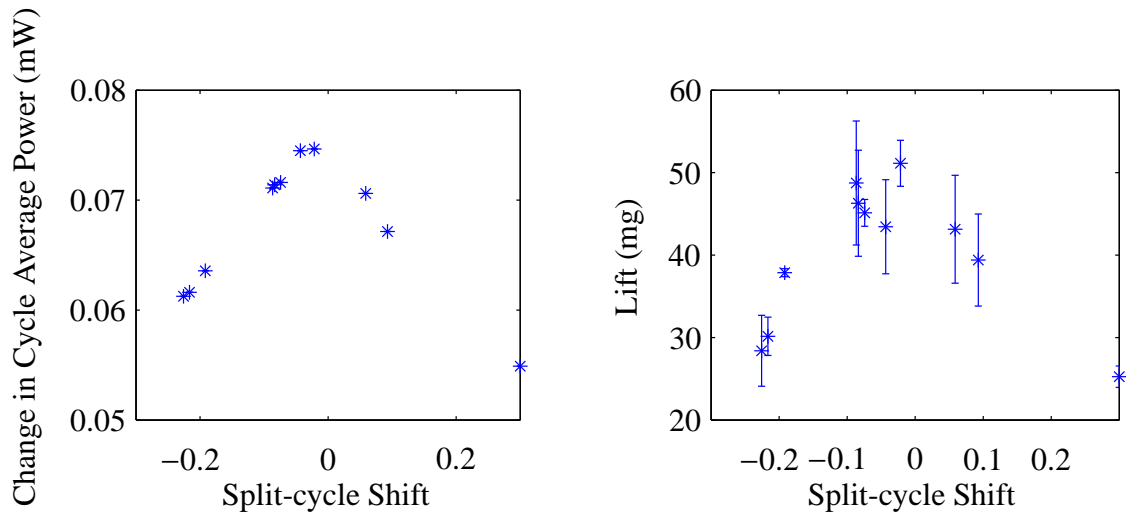


Figure 4.24: Power vs. split-cycle shift, $\tau(n)$, random sampling, $A = 1, \eta = 0$ V

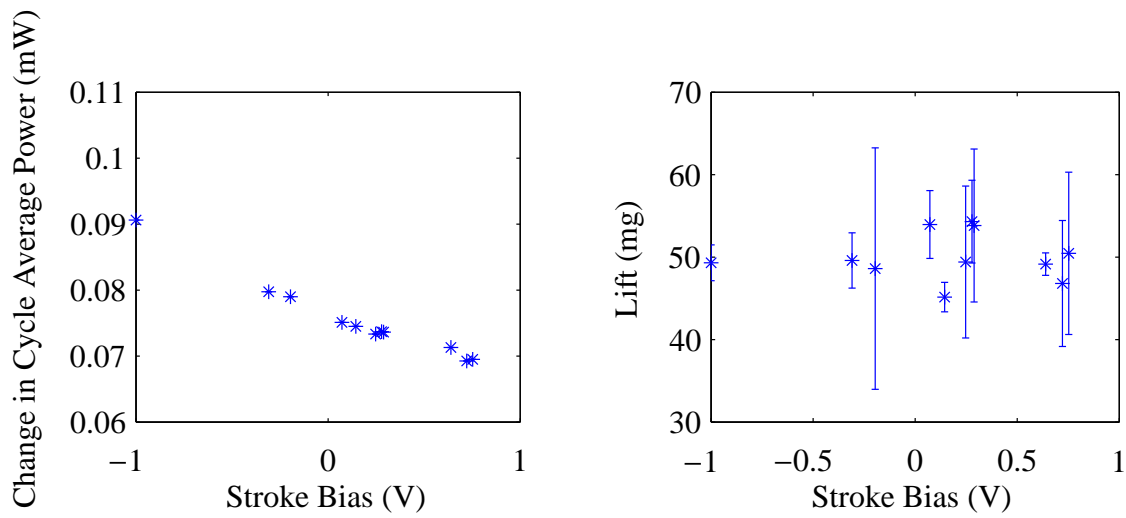


Figure 4.25: Power vs. stroke bias, $\eta(n)$, random sampling, $A = 1, \tau = 0$

4.3 Dual Wing Flapper

After completion of the single-wing flapper testing, a dual-wing flapper was constructed to test. The dual-wing flapper allowed investigation into the side force, the rolling moment, and the yaw moment. Testing on the dual-wing flapper was much quicker due to the lessons learned with the single-wing flapper, mostly in regards to proper test setup. Fifteen test matrices were run resulting in 226 test cases. Approximately 133 cases were used for final analysis. The test setup allowed for separate power measurements on the left and right wing so the results were split into power requirements for each wing. Since power was calculated in Watts as described in Chapter III, the two were additive for total power required. Table 4.1 again served as a basis for comparison to the forces and moments generated.

4.3.1 Amplitude.

Figures 4.26 and 4.27 show the power requirements as a function of the amplitude. Data were collected by varying amplitude from 0.5 to 2.5. The data showed a good trend when compared to the single-wing flapper shown in Figure 4.9. Data agreed between the wings, as the amplitude increased on either wing the power increased in an exponential manner. In addition, the power required matched when both wing amplitudes were at 2.

Data were also collected for the forces and moments as a function of amplitude for each wing. Figures 4.28 and 4.29 show these data. Knowing that the *M. sexta* has a mass averaging 1.55 grams, a lift equal to that would be required to result in flight. From either Figure 4.28 or 4.29, it could be seen that, with this flapper configuration, an amount of lift was not achievable to overcome the mass. As such, an amplitude of 2 was selected to serve as a baseline for later comparison. The plots in Figures 4.28 and 4.29 show, like in the single-wing flapper case, that there was strong correlation between amplitude and lift and between amplitude and pitch with little correlation between amplitude and

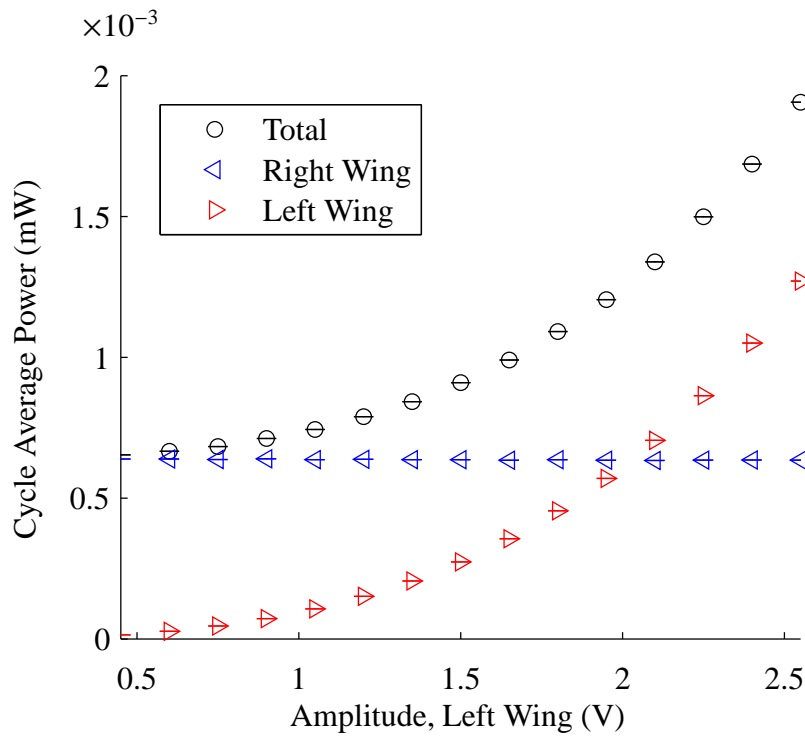


Figure 4.26: Power vs. amplitude, left wing, $A_L(n)$, $A_R = 2 \text{ V}$, $\tau_L = 0$, $\tau_R = 0$, $\eta = 0 \text{ V}$

thrust. Figures 4.28 and 4.29 also show little correlation between amplitude and side force, although a side force of zero at symmetric amplitudes would have been more desirable. The slight difference suggested some differences existed between the left flapper and the right flapper. The roll moment did react to the asymmetric amplitude, an unpredicted result in Table 4.1. This was not unusual though, since the amplitude of a single flapper does affect the thrust (Figure 4.10), a roll moment would result as a difference in thrust between the two wings. As shown in Table 4.1, the yaw moment was greatly affected by the asymmetric change in amplitude. This data suggested that, as in fixed wing aircraft, the roll and yaw moments were coupled.

Figures 4.30 and 4.31 show the relation between power and lift as a function of the amplitude for the left and right wings. The data contradicted each other as to whether

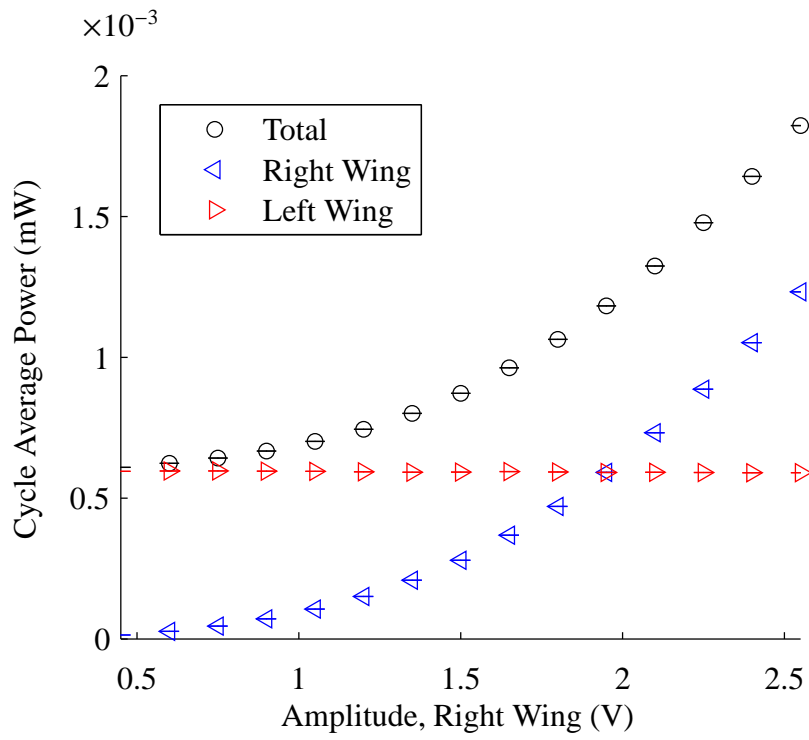


Figure 4.27: Power vs. amplitude, right wing, $A_R(n)$, $A_L = 2$ V, $\tau_L = 0$, $\tau_R = 0$, $\eta = 0$ V

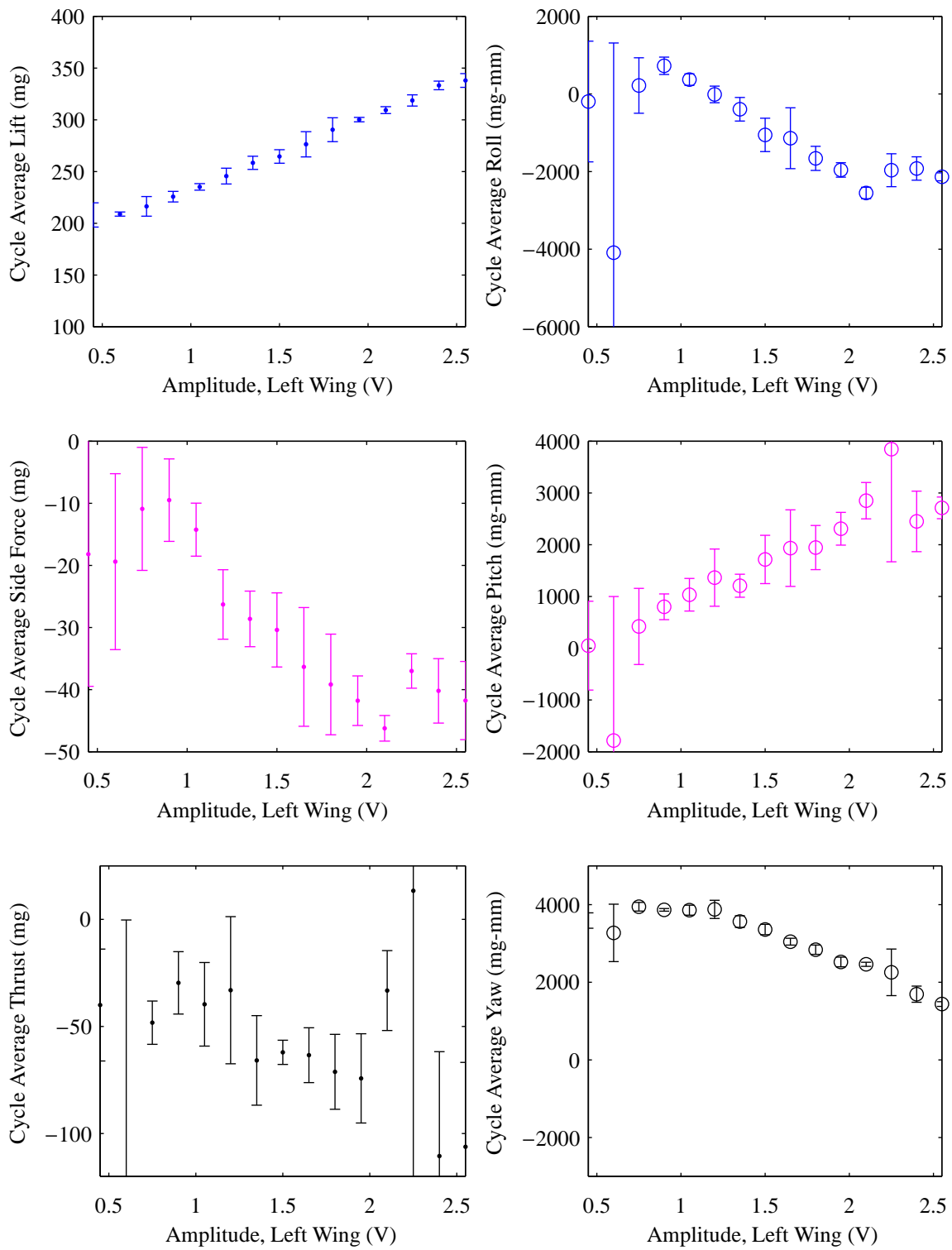


Figure 4.28: Forces and moments about the balance center vs. amplitude, left wing, $A_L(n)$,

$$A_R = 2 \text{ V}, \tau_L = 0, \tau_R = 0, \eta = 0 \text{ V}$$

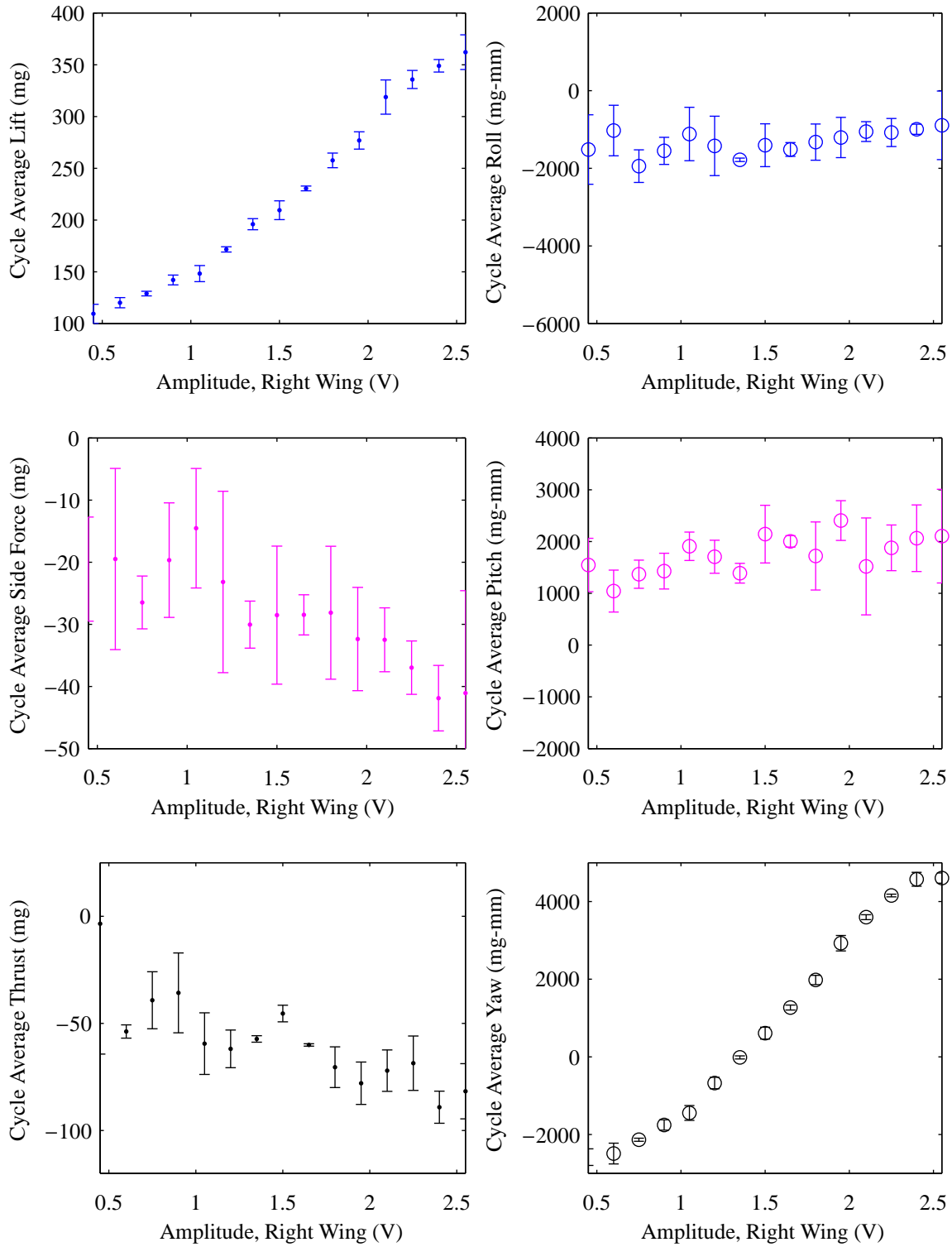


Figure 4.29: Forces and moments about the balance center vs. amplitude, right wing, $A_R(n)$,

$$A_L = 2 \text{ V}, \tau_L = 0, \tau_R = 0, \eta = 0 \text{ V}$$

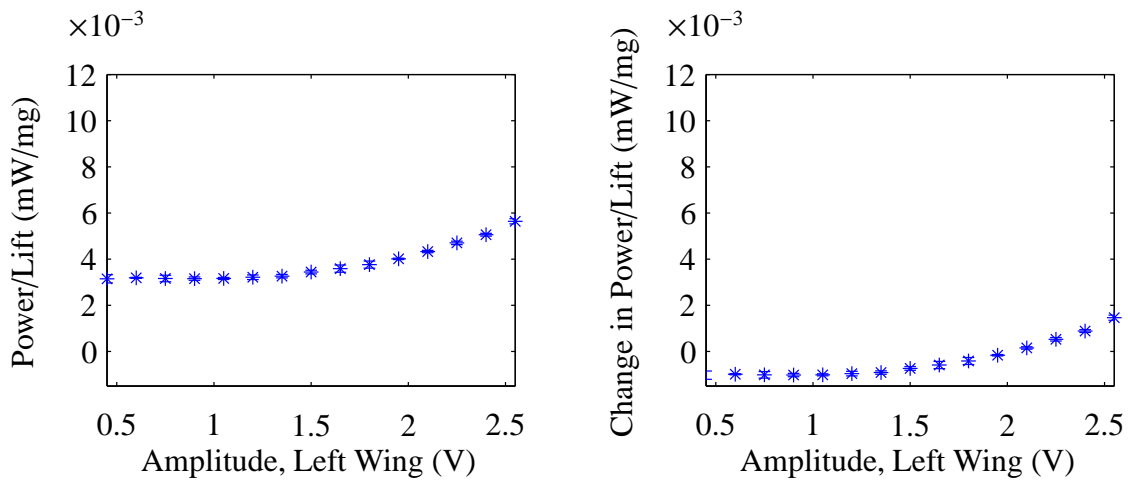


Figure 4.30: Power per lift vs. amplitude, left wing, $A_L(n)$, $A_R = 2$ V, $\tau_L = 0$, $\tau_R = 0$, $\eta = 0$ V

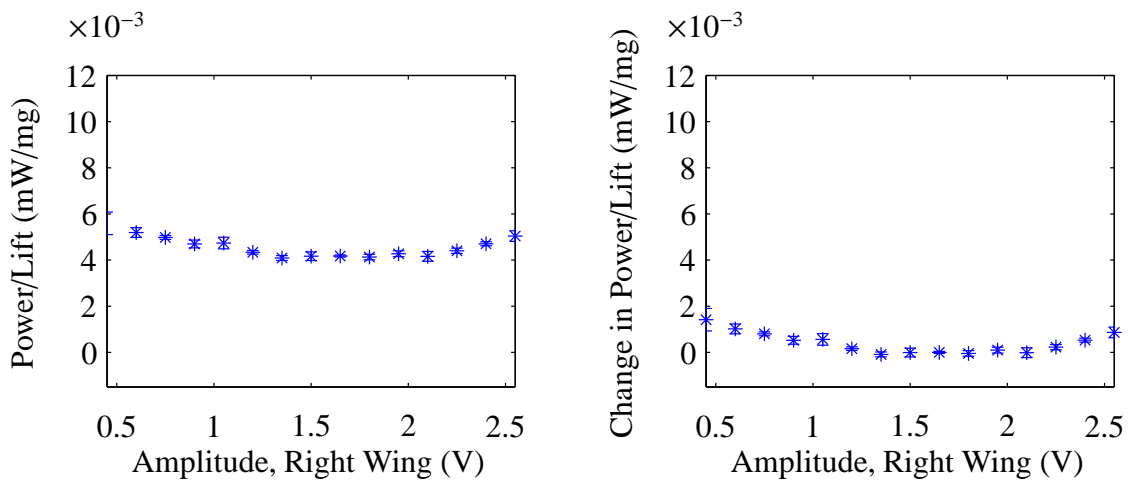


Figure 4.31: Power per lift vs. amplitude, right wing, $A_R(n)$, $A_L = 2$ V, $\tau_L = 0$, $\tau_R = 0$, $\eta = 0$ V

increasing the amplitude resulted in more or less power per lift. Again, the difference suggested some differences existed between the left flapper and the right flapper and were magnified in the power per lift data.

4.3.2 Split-cycle Shift.

Figures 4.32 and 4.33 show the power requirements as a function of the split-cycle shift. Data were collected by varying the split-cycle shift from -0.25 to 0.25, the expected values of usefulness. The power here is not shown as a change from the case of zero split-cycle but rather the total power of the system. As expected, the wing with a constant split-cycle shift of zero required constant power while the wing with varying split-cycle shift required less power. These results agreed with the results of the single-wing flapper.

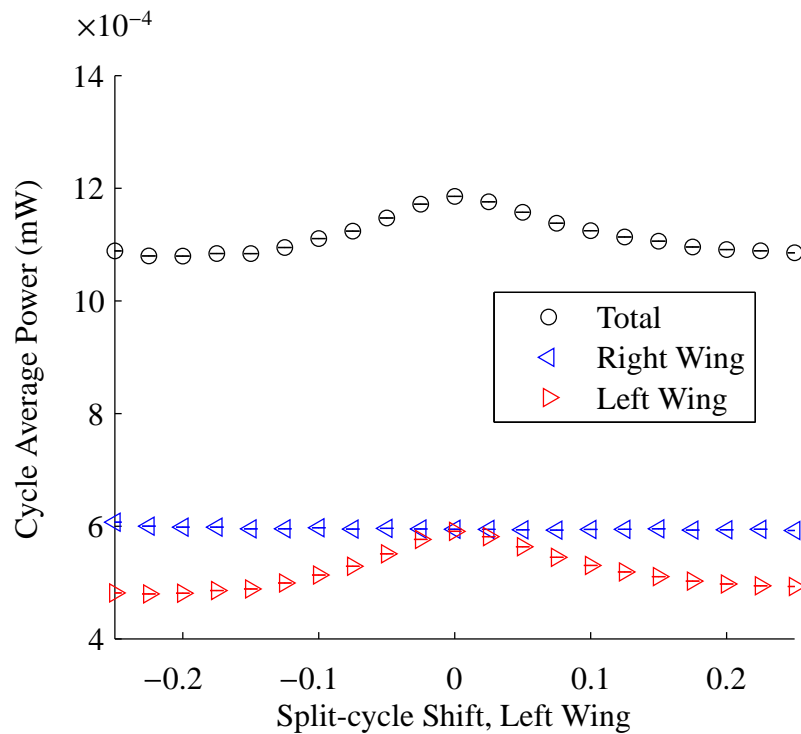


Figure 4.32: Power vs. split-cycle shift, left wing, $\tau_L(n)$, $A_L = 2$, $A_R = 2$ V, $\tau_R = 0$, $\eta = 0$ V

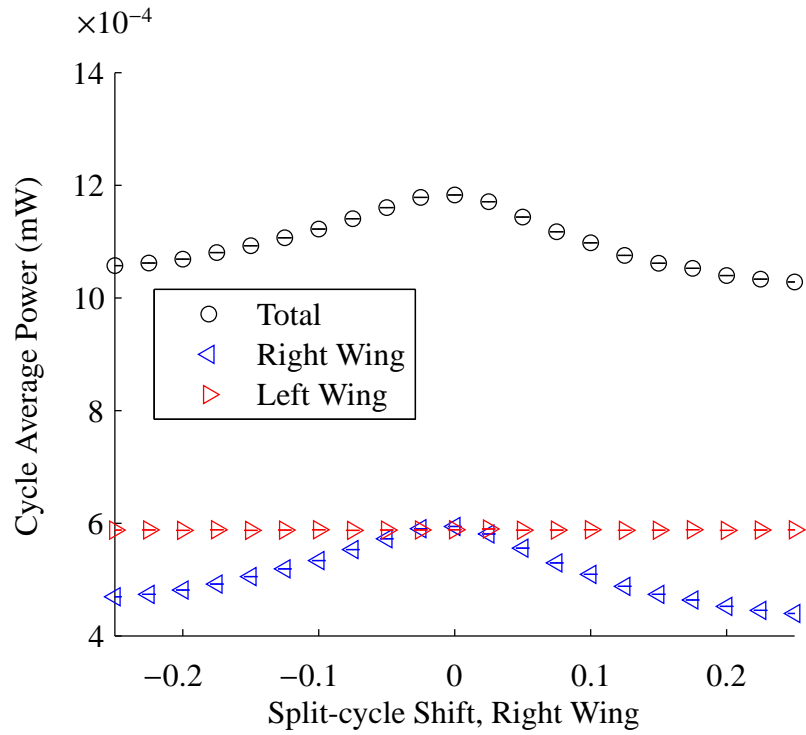


Figure 4.33: Power vs. split-cycle shift, right wing, $\tau_R(n)$, $A_L = 2, A_R = 2$ V, $\tau_L = 0, \eta = 0$ V

Data were also collected for the forces and moments as a function of split-cycle shift for each wing. These data are shown in Figures 4.34 and 4.35. Similar correlations between the lift, thrust, pitch moment and split-cycle shift occurred with the single-wing flapper and the dual-wing flapper. Split-cycle shift had little effect on the side force. The yaw moment was effected by the change in the split-cycle shift, as predicted in Table 4.1. As the split-cycle shift was asymmetrically increased or decreased from zero, the yaw increased or decreased depending on which wing had a greater split-cycle shift. This made sense with knowledge from Figure 4.15 on how the split-cycle shift affected the lift on one wing. As

suggested by the dual-wing flapper amplitude tests, the yaw and roll moments were again coupled.

Figures 4.36 and 4.37 show the relation between power and lift as a function of the split-cycle shift for the left and right wings. The data showed that increasing or decreasing the split-cycle shift on either wing resulted in more power per lift. The results agreed with the results shown in Figure 4.16.

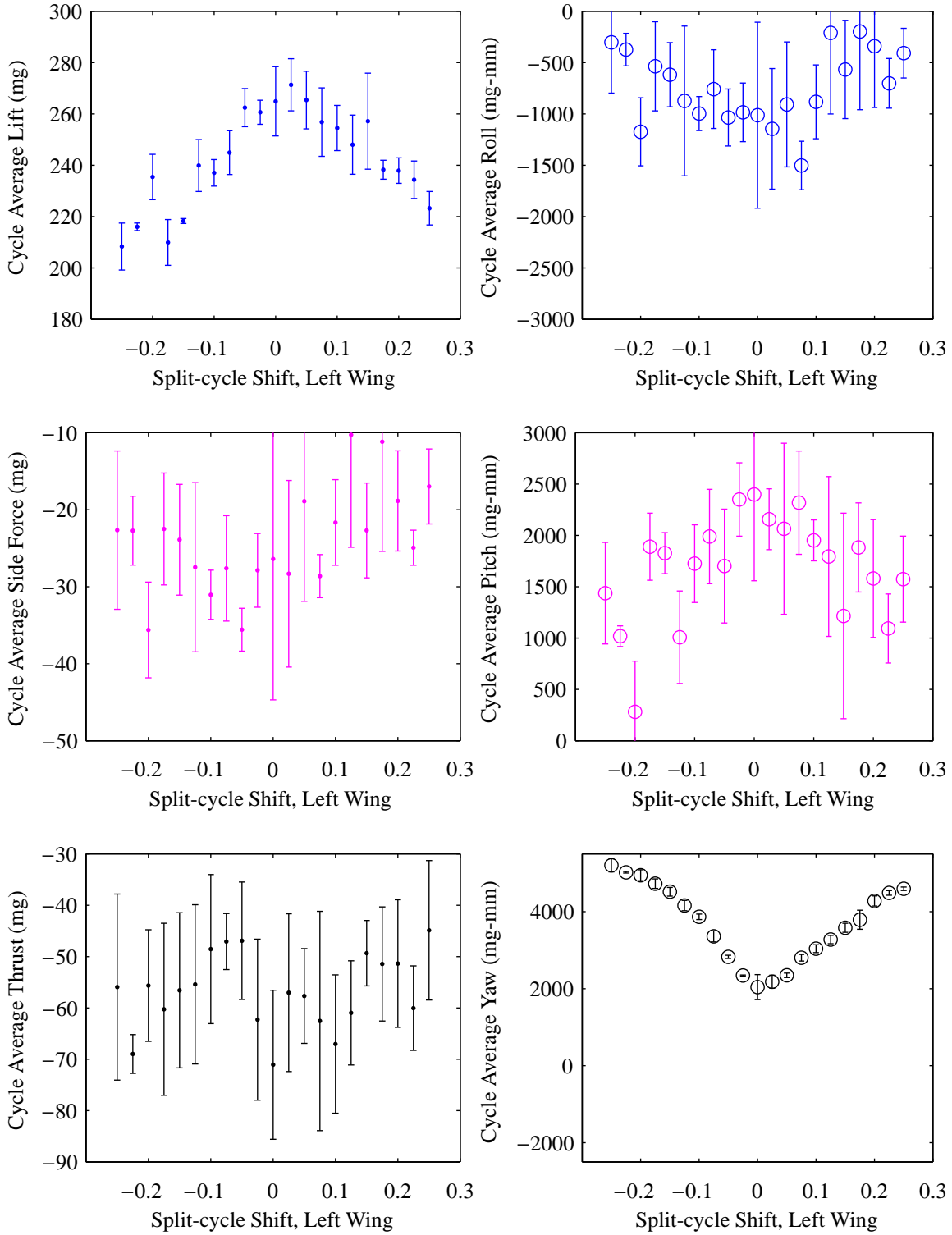


Figure 4.34: Forces and moments about the balance center vs. split-cycle shift, left wing,

$$\tau_L(n), A_L = 2, A_R = 2 \text{ V}, \tau_R = 0, \eta = 0 \text{ V}$$

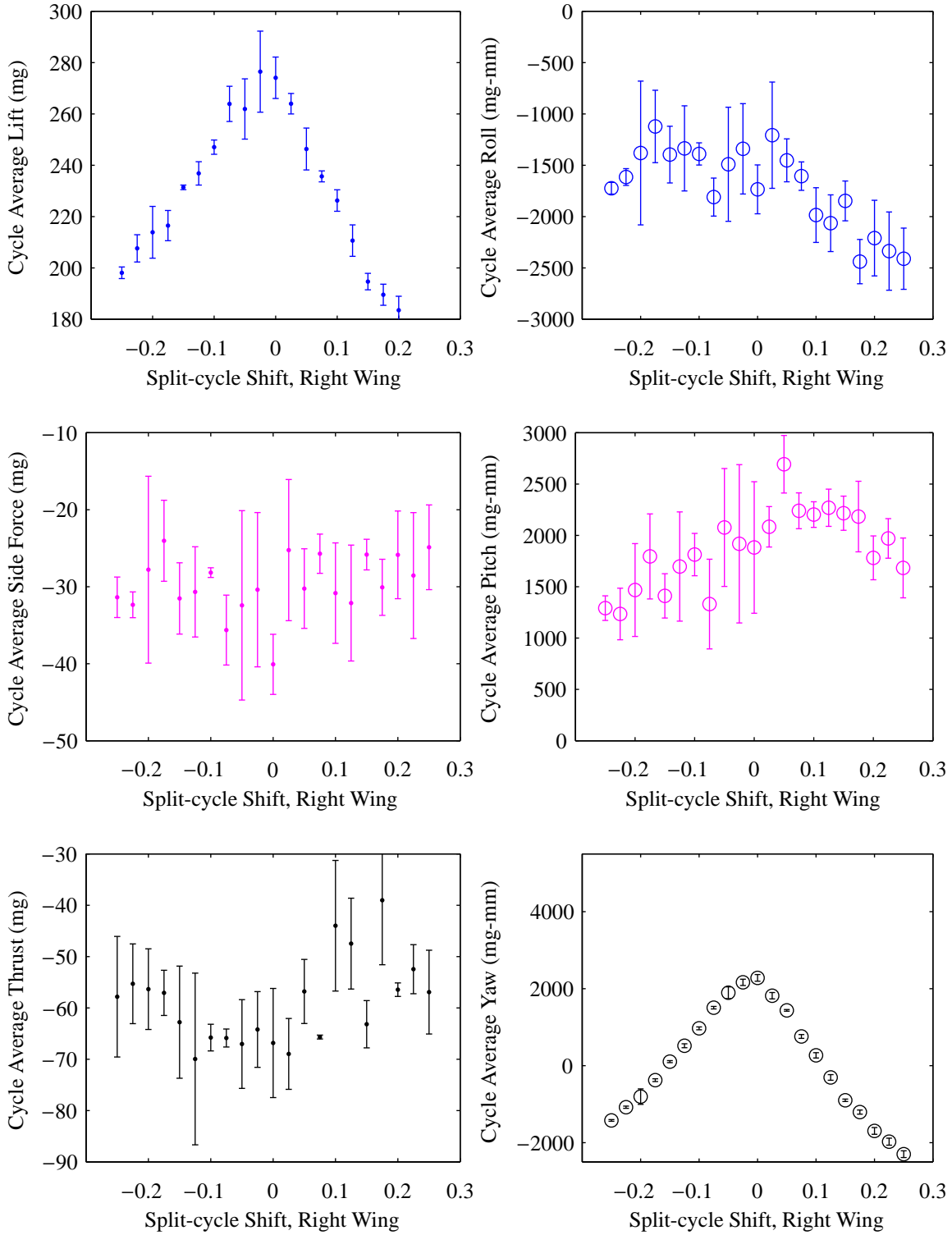


Figure 4.35: Forces and moments about the balance center vs. split-cycle shift, right wing,

$$\tau_R(n), A_L = 2, A_R = 2 \text{ V}, \tau_L = 0, \eta = 0 \text{ V}$$

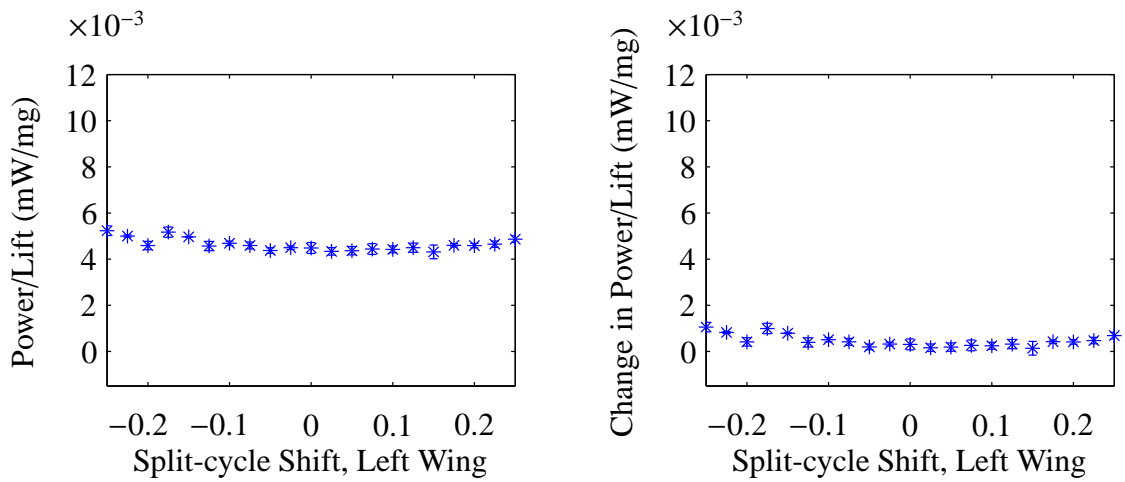


Figure 4.36: Power per lift vs. split-cycle shift, left wing, $\tau_L(n)$, $A_L = 2$, $A_R = 2$ V, $\tau_R = 0$, $\eta = 0$ V

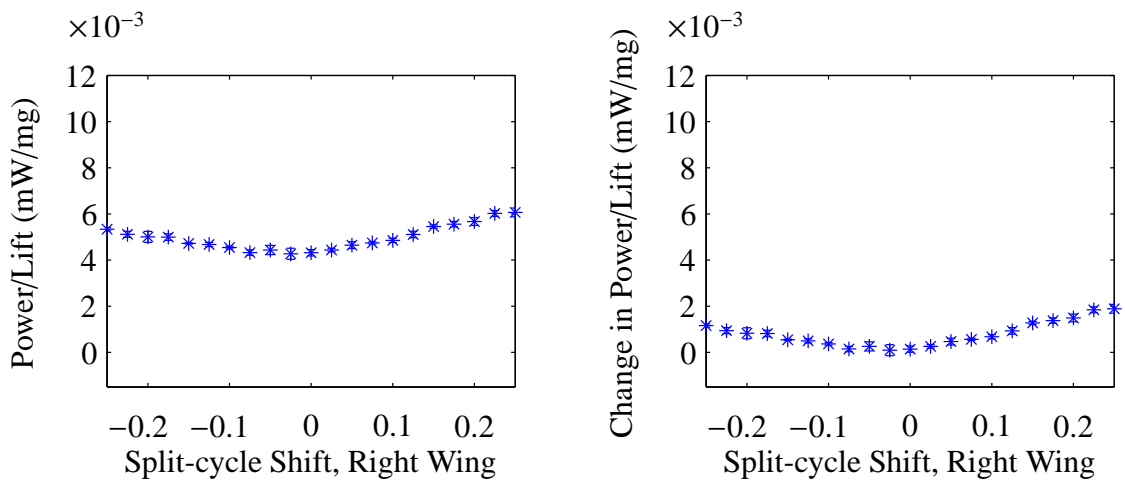


Figure 4.37: Power per lift vs. split-cycle shift, right wing, $\tau_R(n)$, $A_L = 2$, $A_R = 2$ V, $\tau_L = 0$, $\eta = 0$ V

4.3.3 Stroke Bias.

Figure 4.38 shows the results of data collected for symmetric change of stroke bias. Referring to the data shown in Figure 4.17, the power requirements should have been similar for the left and right wing, but that was not the case. In fact, the data from the left wing showed what was to be expected, that as the stroke bias was changed, there was little effect on the power requirements. These data suggested asymmetry in the piezoelectric actuator. Further investigation is required to identify these differences.

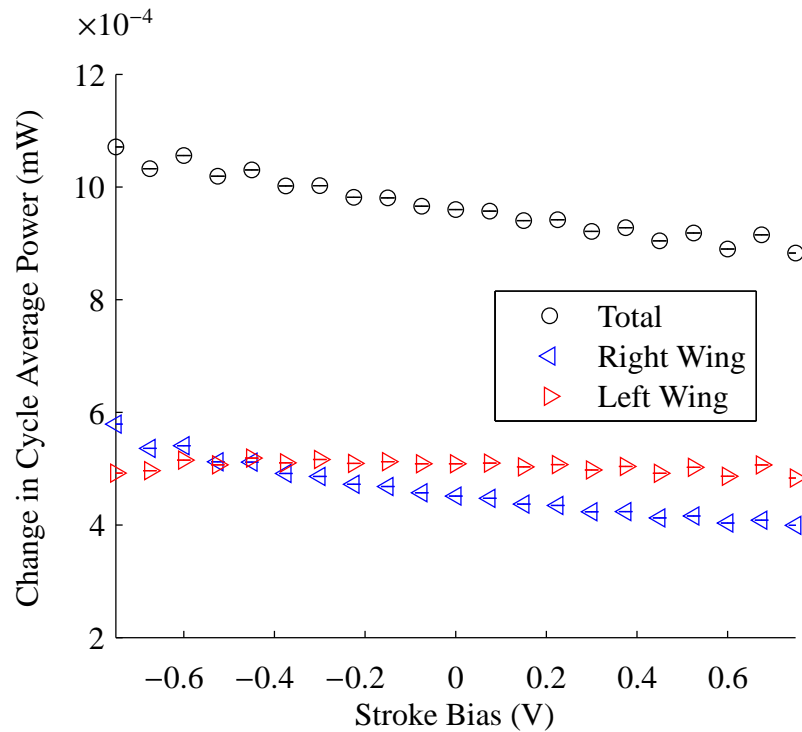


Figure 4.38: Power vs. stroke bias, $\eta(n)$, $A_L = 2$, $A_R = 2$ V, $\tau_L = 0$, $\tau_R = 0$

Data were also collected for the forces and moments as a function of symmetric stroke bias. Since these data were for symmetric stroke bias, similar trends were expected between the single-wing flapper case (Figure 4.18) and the dual-wing flapper case shown in Figure 4.39. This was true for the thrust and pitch moment, albeit that the effect on pitch

moment was magnified. But in this case, stroke bias had a small detrimental effect on lift that may not have been detectable in the single-wing flapper case. Even more interesting, was the effect stroke bias had on roll and, by coupling, yaw moment. Which of these effects were due to stroke bias and which were a result of power difference were difficult to discern. More testing is required, preferably once a final piezoelectric actuator has been chosen.

Figure 4.40 shows the relation between power and lift as a function of the stroke bias. The data showed that increasing or decreasing the stroke bias resulted in more power per lift. The results are much closer to what was expected but did not agree with the results presented in Figure 4.19. This further suggested that asymmetries were present between the flappers.

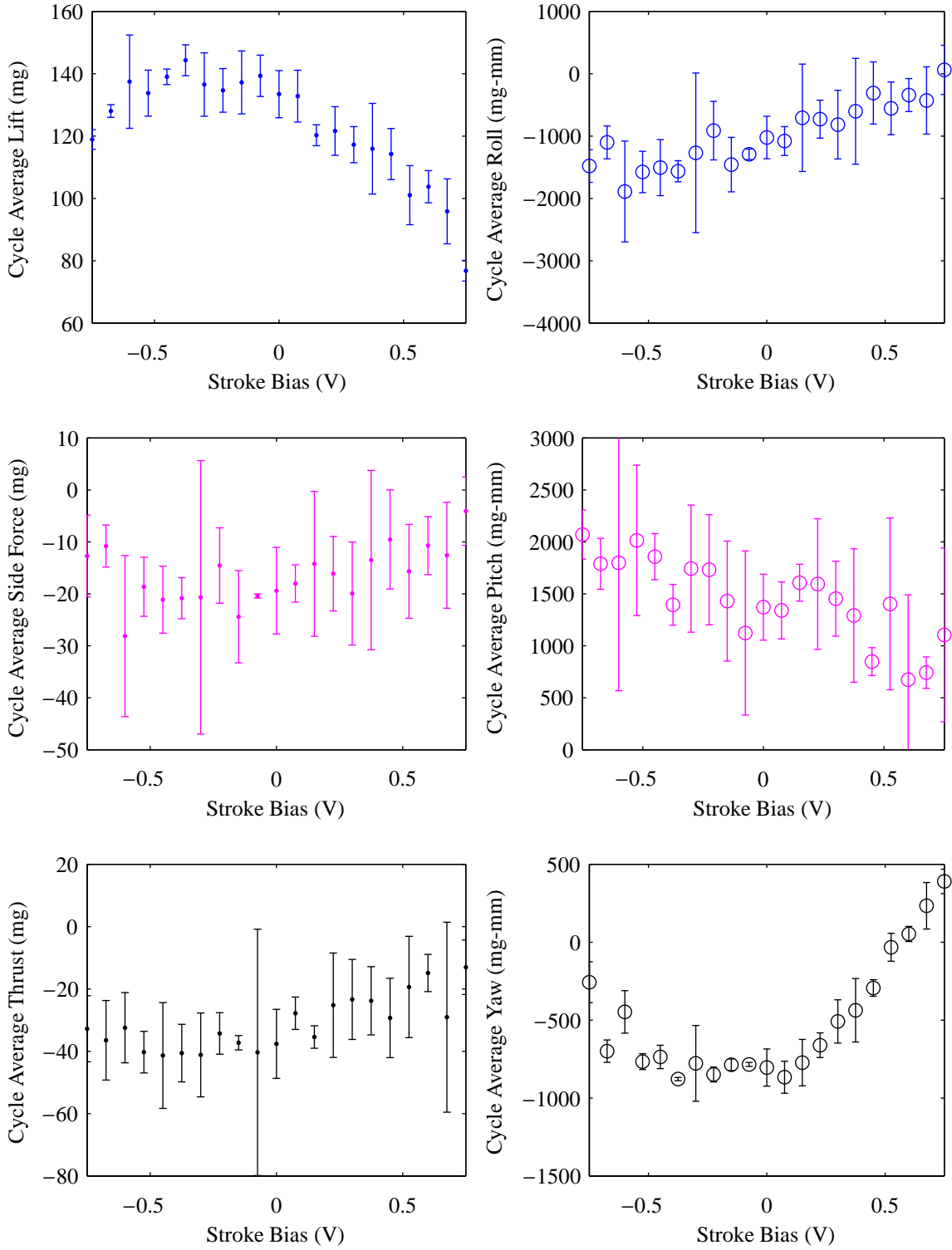


Figure 4.39: Forces and moments about the balance center vs. stroke bias, $\eta(n)$, $A_L = 2$, $A_R = 2$ V, $\tau_L = 0$, $\tau_R = 0$

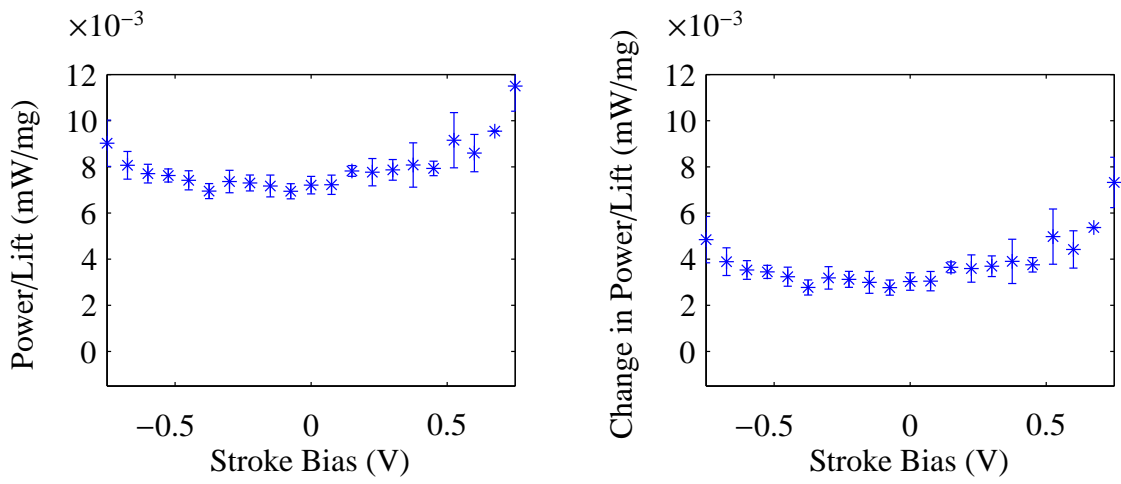


Figure 4.40: Power per lift vs. stroke bias, $\eta(n)$, $A_L = 2$, $A_R = 2$ V, $\tau_L = 0$, $\tau_R = 0$

4.3.4 Design of Experiments.

Figure 4.41 shows the results from the DOE run accomplished using Table 3.2. The data showed the correlation between all five BABM parameters and the seven measurements. Again, the blue dashed lines represent confidence intervals to one standard deviation. It is important to note that fewer data runs were accomplished to generate the plots in Figure 4.41. Examining data for the amplitude from both left and right flapper and its effect on side force produce some concerns. In fact, close analysis of all the data from the left and right flapper indicate the conclusion made above when investigating the stroke bias on the dual-wing flapper; that there were asymmetries in the piezoelectric actuators. Ideally, these tests would be performed again, but piezoelectric actuators were in low supply when these differences manifested. In any case, these relations were important, because consistent operation in the field is difficult to ensure. An emphasis was placed on the results for the left flapper since the left piezoelectric actuator was less used. The data indicated that to manipulate the roll moment, an asymmetric amplitude would be most affective, contrary to Table 4.1. The data also shows that asymmetric split-cycle shift may be as effective as asymmetric amplitude to control yaw.

Figures 4.42 and 4.43 show the relations for power and lift associated with a dual-wing flapper. Recall that the bars are scaled estimates normalized between -1 and 1 where a negative relationship is detrimental to the output and that the blue lines on the charts mark a value of 0.2 indicating a strong relationship. The data agreed that amplitude has the greatest and only significant affect on the power. The lift data identified a strong effect from stroke bias squared and split-cycle squared. The lift data also identified a strong benefit from right wing amplitude and stroke bias, but the fact that it was not symmetric with left wing amplitude and stroke bias cause further speculation of the stroke bias measurements.

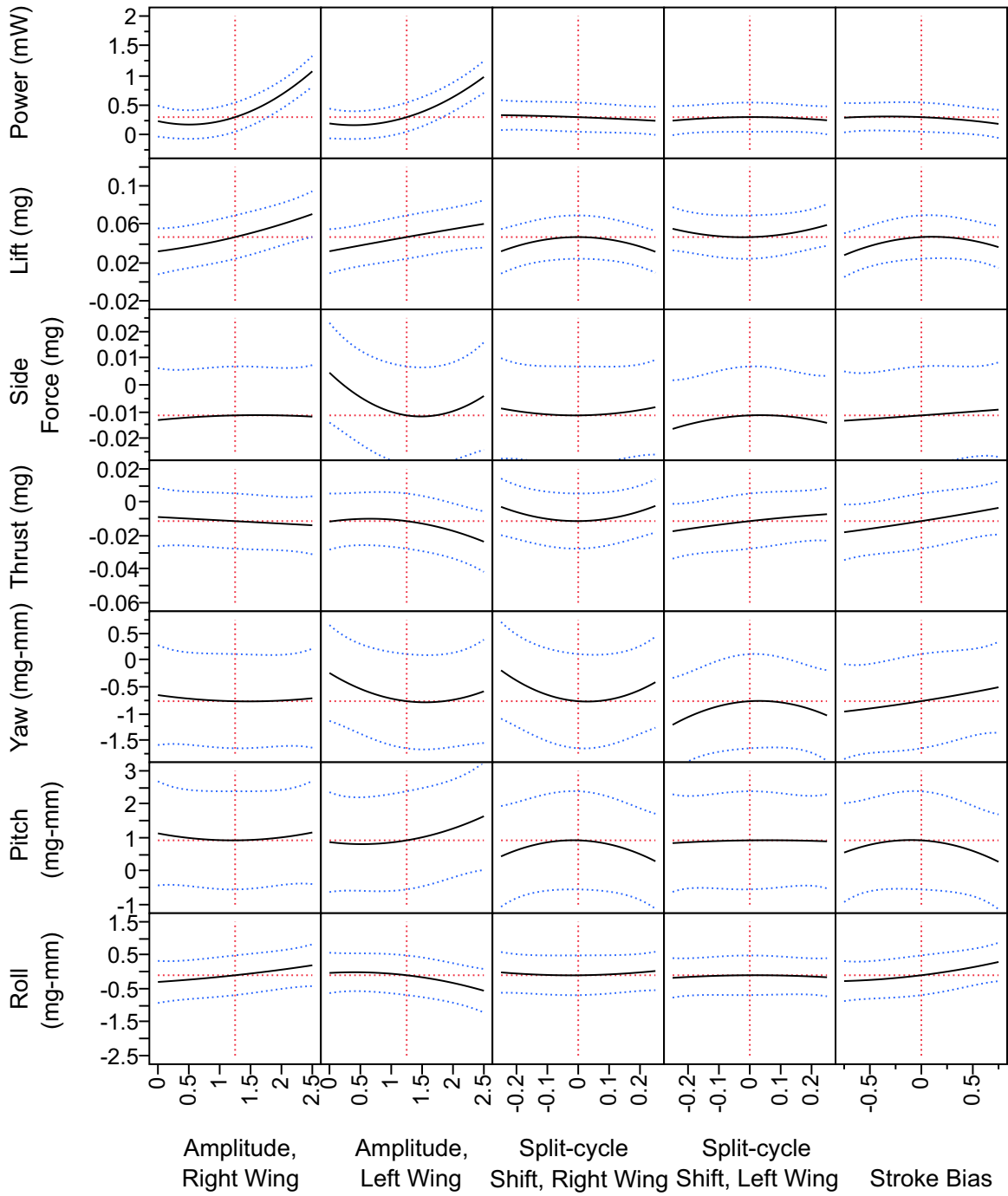


Figure 4.41: DOE results for dual-wing flapper

Parameter(s)

- Amplitude, Right Wing
- Amplitude, Left Wing
- Stroke Bias
- Split-cycle Shift, Right Wing
- Split-cycle Shift, Left Wing
- Amplitude, Right Wing*Amplitude, Right Wing
- Amplitude, Right Wing*Amplitude, Left Wing
- Amplitude, Left Wing*Amplitude, Left Wing
- Amplitude, Right Wing*Stroke Bias
- Amplitude, Left Wing*Stroke Bias
- Stroke Bias*Stroke Bias
- Amplitude, Right Wing*Split-cycle Shift, Right Wing
- Amplitude, Left Wing*Split-cycle Shift, Right Wing
- Stroke Bias*Split-cycle Shift, Right Wing
- Split-cycle Shift, Right Wing*Split-cycle Shift, Right Wing
- Amplitude, Right Wing*Split-cycle Shift, Left Wing
- Amplitude, Left Wing*Split-cycle Shift, Left Wing
- Stroke Bias*Split-cycle Shift, Left Wing
- Split-cycle Shift, Right Wing*Split-cycle Shift, Left Wing
- Split-cycle Shift, Left Wing*Split-cycle Shift, Left Wing
- Amplitude, Right Wing*Amplitude, Right Wing*Amplitude, Left Wing
- Amplitude, Right Wing*Amplitude, Left Wing*Amplitude, Left Wing
- Amplitude, Right Wing*Amplitude, Right Wing*Stroke Bias
- Amplitude, Right Wing*Amplitude, Left Wing*Stroke Bias
- Amplitude, Left Wing*Amplitude, Left Wing*Stroke Bias
- Amplitude, Right Wing*Stroke Bias*Stroke Bias
- Amplitude, Left Wing*Stroke Bias*Stroke Bias

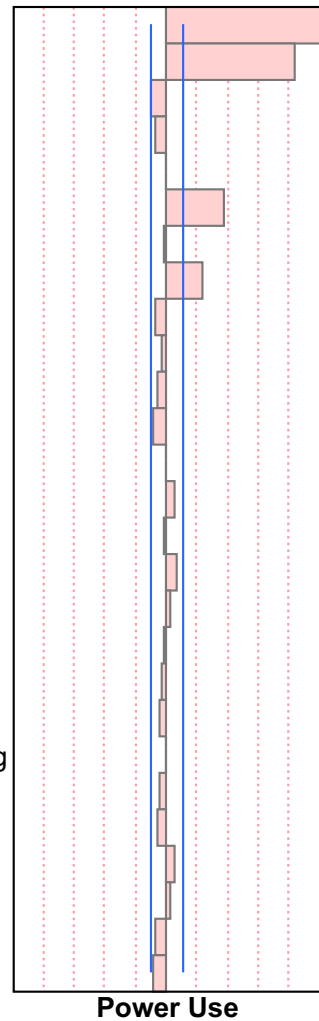


Figure 4.42: BABM parameter effects on power for a dual-wing flapper

Parameter(s)

- Amplitude, Right Wing
- Amplitude, Left Wing
- Stroke Bias
- Split-cycle Shift, Left Wing
- Split-cycle Shift, Right Wing
- Amplitude, Right Wing*Amplitude, Right Wing
- Amplitude, Right Wing*Amplitude, Left Wing
- Amplitude, Left Wing*Amplitude, Left Wing
- Amplitude, Right Wing*Stroke Bias
- Amplitude, Left Wing*Stroke Bias
- Stroke Bias*Stroke Bias
- Amplitude, Right Wing*Split-cycle Shift, Left Wing
- Amplitude, Left Wing*Split-cycle Shift, Left Wing
- Stroke Bias*Split-cycle Shift, Left Wing
- Split-cycle Shift, Left Wing*Split-cycle Shift, Left Wing
- Amplitude, Right Wing*Split-cycle Shift, Right Wing
- Amplitude, Left Wing*Split-cycle Shift, Right Wing
- Stroke Bias*Split-cycle Shift, Right Wing
- Split-cycle Shift, Left Wing*Split-cycle Shift, Right Wing
- Split-cycle Shift, Right Wing*Split-cycle Shift, Right Wing
- Amplitude, Right Wing*Amplitude, Right Wing*Amplitude, Left Wing
- Amplitude, Right Wing*Amplitude, Left Wing*Amplitude, Left Wing
- Amplitude, Right Wing*Amplitude, Right Wing*Stroke Bias
- Amplitude, Right Wing*Amplitude, Left Wing*Stroke Bias
- Amplitude, Left Wing*Amplitude, Left Wing*Stroke Bias
- Amplitude, Right Wing*Stroke Bias*Stroke Bias
- Amplitude, Left Wing*Stroke Bias*Stroke Bias

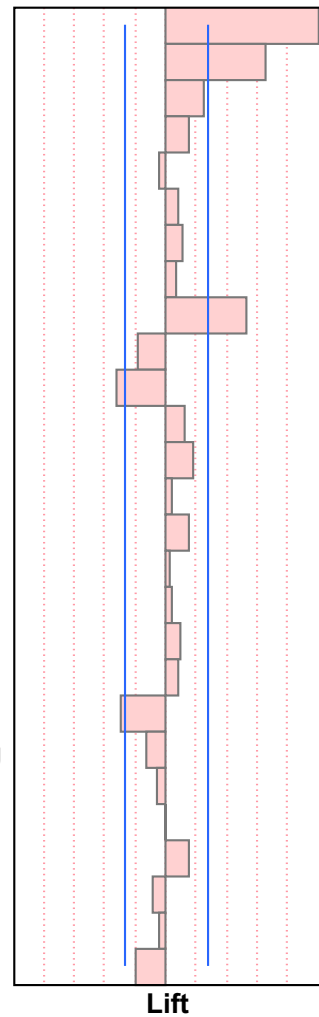


Figure 4.43: BABM parameter effects on lift for a dual-wing flapper

4.4 Comparison to Earlier Work

Little work has been done in this area for comparison. Reference 31 tested a small range of amplitude and stroke bias and a similar range to split-cycle shift tested here. The power results, the only ones presented in Reference 31, followed similar trends as the power results presented here except in the case of stroke bias. The results presented in Reference 31 showed no correlation between stroke bias and power, similar to the left wing in the dual-wing flapper case above. This further suggested that the power amplifier provided asymmetric signals when supplied the same input.

Some of the results presented in Reference 6, Table 4.1 did not hold true for this flapper configuration. It is important to note that the results found in this work do not dispute the work in Reference 6, this work in fact compliments it. The data gathered in Reference 6 was on a different wing configuration and flapper structure. Recall that the wing used for this research was optimized to match the inertial moments of the *M. sexta*.

4.5 Chapter Summary

A lot of data was presented in this chapter, but few conclusions were discussed. Chapter V will discuss the impacts these results will have on the way forward for the AFIT FWMAV.

V. Conclusions

CONCLUSIONS from the data presented in the previous chapters are presented here. The data was combined with the knowledge from the research to draw conclusions that address the research goals.

5.1 Research Goals

Recall the goals stated in Chapter I: *How much power is required to vary each parameter and maintain lift? How do those power requirements relate to controllability?* These goals were set forth to provide future researchers and control designers a reference when considering the power requirements of the FWMAV. Since one mission of the FWMAV is ISR, which is inherently lengthy, then power concerns are of high importance, especially when a FWMAV uses the same power source for flight and sensors. Therefore, this research was performed to quantify the power requirements of BABM, the control scheme proposed by AFIT.

5.2 Summary of Results

The data from the figures in Chapter IV are summarized in Table 5.1. The only data that was inconclusive was in regards to the stroke bias. An understanding of the dynamics at play might indicate that the power and lift should not change as the stroke bias is changed. Data indicated that power was constant with varying stroke bias in the left wing during dual-wing flapper testing, Figure 4.38, but not in the right wing. Data further indicated that lift was constant with varying stroke bias for the single-wing flapper, Figure 4.18, but not for the dual-wing flapper, Figure 4.39. Recall that the condition with $A_L = A_R = 2$ and $\tau_L = \tau_R = \eta = 0$ was chosen as a baseline for hover. This condition provided $P = 1.24$ mW, $X = 297$ mg, $Y = 37$ mg, $Z = 68$ mg, $L = 1650$ mg-mm, $M = 2300$ mg-mm, $N = 2800$ mg-

mm. Ideally, this condition would provide lift exclusively but since it did not, a routine will have to be incorporated in the future to trim the FWMAV.

Table 5.1: Effects of BABM parameters on power and lift

BABM Parameter	Effect on Power	Effect on Lift
Amplitude \uparrow	\uparrow	\uparrow
Amplitude \downarrow	\downarrow	\downarrow
Split-cycle Shift \uparrow	\downarrow	\downarrow
Split-cycle Shift \downarrow	\downarrow	\downarrow
Stroke Bias \uparrow	Inconclusive	Inconclusive
Stroke Bias \downarrow	Inconclusive	Inconclusive

5.2.1 Power.

From the data, some specific relations between power and the BABM parameters can be identified. A symmetric increase of amplitude by 10% required an increase in power by 0.38 milliwatts, approximately 30%. A symmetric decrease of amplitude by 10% allowed a decrease in power by 0.33 milliwatts, approximately 26%. An asymmetric increase of amplitude by 10% required an increase in power by 0.20 milliwatts, approximately 16%. An asymmetric decrease of amplitude by 10% allowed a decrease in power by 0.16 milliwatts, approximately 13%. A symmetric change of split-cycle shift to ± 0.3 (the maximum change) allowed a decrease in power by approximately 25%. An asymmetric change of split-cycle shift to ± 0.25 allowed a decrease in power by approximately 14%. A change of stroke bias to ± 0.75 (the maximum tested on the dual-wing flapper) required

an increase in power by approximately 1%. Clearly, amplitude has the greatest effect on power while the effect of stroke bias may be negligible.

5.2.2 Controllability.

Some of the results presented in Reference 6 did not hold true for this flapper configuration. Table 5.2 summarizes the effects of control on the forces and moments for the current wing and structure of the AFIT FWMAV. In some cases, the side-force, thrust, and moments were not zero, indicating that the FWMAV would need to be trimmed. Since there is currently no trim routine, the forces and moments will be discussed as percentages. Furthermore, the research demonstrated what has been known about fixed-wing aircraft for decades, that moments are closely coupled and an active control scheme is required for stability.

Table 5.2: Summary of forces and moments generated by changing BABM parameter

	BABM
Lift, X	Symmetric Amplitude (Very Strong Correlation)
Side Force, Y	Asymmetric Amplitude (Very Weak Correlation)
Thrust, Z	Symmetric Split-Cycle (Weak Correlation) & Symmetric Stroke Bias (Weak Correlation)
Roll, L	Asymmetric Split-Cycle (Weak Correlation)
Pitch, M	Symmetric Stroke Bias (Strong Correlation) & Asymmetric Split-Cycle (Weak Correlation)
Yaw, N	Asymmetric Amplitude (Strong Correlation) & Asymmetric Split-Cycle (Strong Correlation)

From the data, specific relations between control and the BABM parameters can be identified. A symmetric increase in amplitude by 10% provided an increase in lift by approximately 22%, while requiring an increase in power by approximately 30%. An asymmetric increase in amplitude by 10% provided more lift but the goal is to maintain lift. The data showed that an asymmetric change of equal magnitude, i.e. increasing one wing by 10% and decreasing the opposite wing by 10%, would maintain lift and power at the baseline. An asymmetric change in amplitude by 10% in both wings provided an increase in side-force by approximately 12%. An asymmetric change of split-cycle to ± 0.25 increased the roll moment by approximately 14%, increased the pitch moment by approximately 29%, and decreased the yaw moment by approximately 100%. The asymmetric split-cycle shift also decreased the lift by approximately 25%, which would require an increase in amplitude to maintain lift. While the asymmetric split-cycle shift requires less power, the increase in amplitude to maintain lift would require a net increase in power by approximately 16% over the baseline. A change of stroke bias to ± 0.75 provided a change in thrust by 56%. The change in stroke bias also caused a loss of lift by approximately 27% but did not affect the power required. The loss of lift would have to be overcome by an increase in amplitude.

5.3 Future Work

The author suggests that some of these tests be completed again once the piezoelectric actuator and the passive rotation stops are finalized. In addition, an effort should be made to mount the final flight vehicle to the balance rather than using a different structure. Since power and control are such complex problems associated with FWMAV flight, it would be best to finalize other aspects of design prior to designing a controller.

Research is on going to study the aerodynamic effects of flight on a FWMAV. Once conclusions are made regarding these effects, the forces and moments can be related to actual maneuverability of the FWMAV.

As stated earlier, a routine to trim the FWMAV will be required prior to flight. Such a routine should be designed using this research to simulate expected forces and moments given certain BABM parameters. If changes to the vehicle design are made, the model can then be updated to reflect the most current design iteration.

Efforts should also be made to design control logic for minimum power path optimization based on the data obtained in this research. During those efforts, careful documentation should be taken to ease the future redesigns should the FWMAV change significantly.

Appendix: Explanation of MATLAB Scripts

THE MATLAB code that was used for this research is summarized here. This appendix identifies the custom code prepared and outlines the required inputs and outputs for each of the scripts.

I. DWF_Test_non_Bias.m

This script performed the designed set of experiments on a dual-wing flapper without a bias drive. It would perform single test cases or multiple cases by varying the frequency or the BABM parameters. The data was stored in a array of structures. The script is largely based on the work of Captain Garrison Lindholm.

Inputs

maxA →Maximum voltage for PZT actuator

w →Frequency (rad/sec)

eta →Stroke bias

AR →Amplitude, right wing

tauR →Split-cycle shift, right wing

AL →Amplitude, left wing

tauL →Split-cycle shift, left wing

M1pR →Magnitude 1st harmonic, right wing

M2pR →Magnitude 2nd harmonic, right wing

beta1pR →Phase 1st harmonic, right wing

beta2pR →Phase 2nd harmonic, right wing

M1pL →Magnitude 1st harmonic, left wing

`M2pL` → Magnitude 2nd harmonic, left wing

`beta1pL` → Phase 1st harmonic, left wing

`beta2pL` → Phase 2nd harmonic, left wing

`samples` → Number of sample runs per test point

`simFlag` → 1 = simulation, 0 = hardware test

`testFlag` → 2 = BABM test, 1 = Frequency test, 0 = Single test case

Outputs

`data` → Data structure with inputs, outputs, units, and information pertaining to the tests

II. `DWFt.m`

This script ran the tests for `DWF_Test_non_Bias.m` with the selected number of sample runs. This script also performed the cycle-average analysis. The script is largely based on the work of Captain Garrison Lindholm.

Inputs

`maxA` → Vector of time

`w` → Frequency (rad/sec)

`BABMs` → A structure containing BABM constants for each test case

`samples` → Number of samples at test case

`simFlag` → 1 = simulation, 0 = hardware test

Outputs

`out` → Data structure with inputs, outputs, units, and information pertaining to the tests

III. DWFs.m

This script ran the individual test runs for DWFt.m. The script is largely based on the work of Captain Garrison Lindholm.

Inputs

maxA → Vector of time

w → Frequency (rad/sec)

BABMs → A structure containing BABM constants

simFlag → 1 = true (simulation), 0 = false (hardware test)

Outputs

P → Power in amps

V → Raw voltage

I → Raw current

forceX → Tared forces in x-direction in grams

forceZ → Tared forces in z-direction in grams

forceY → Tared forces in y-direction in grams

input → Input parameters used in this sample run

dis → Tared displacement in millimeters

S → Sampling information used in this sample run

IV. SWF_Test_non_Bias.m

This script performed the designed set of experiments on a dual-wing flapper without a bias drive. It would perform single test cases or multiple cases by varying the frequency or the BABM parameters. The data was stored in a array of structures. The script is largely based on the work of Captain Garrison Lindholm.

Inputs

`maxA` →Maximum voltage for PZT actuator

`w` →Frequency (rad/sec)

`eta` →Stroke bias

`A` →Amplitude

`tau` →Split-cycle shift

`M1pR` →Magnitude 1st harmonic

`M2pR` →Magnitude 2nd harmonic

`beta1pR` →Phase 1st harmonic

`beta2pR` →Phase 2nd harmonic

`samples` →Number of sample runs per test point

`simFlag` →1 = simulation, 0 = hardware test

`testFlag` →2 = BABM test, 1 = Frequency test, 0 = Single test case

Outputs

`data` →Data structure with inputs, outputs, units, and information pertaining to the tests

V. SWFt.m

This script ran the tests for `SWF_Test_non_Bias.m` with the selected number of sample runs. This script also performed the cycle-average analysis. The script is largely based on the work of Captain Garrison Lindholm.

Inputs

`maxA` →Vector of time

w → Frequency (rad/sec)

BABMs → A structure containing BABM constants for each test case

samples → Number of samples at test case

simFlag → 1 = simulation, 0 = hardware test

Outputs

out → Data structure with inputs, outputs, units, and information pertaining to the tests

VI. SWFs.m

This script ran the individual test runs for SWFt.m. The script is largely based on the work of Captain Garrison Lindholm.

Inputs

maxA → Vector of time

w → Frequency (rad/sec)

BABMs → A structure containing BABM constants

simFlag → 1 = true (simulation), 0 = false (hardware test)

Outputs

P → Power in amps

V → Raw voltage

I → Raw current

forceX → Tared forces in x-direction in grams

forceZ → Tared forces in z-direction in grams

forceY → Tared forces in y-direction in grams

input →Input parameters used in this sample run

dis →Tared displacement in millimeters

S →Sampling information used in this sample run

VII. BABM.m

Function was designed to take the desired signal length, drive frequency, BABM parameters, and FRF plant information and then output the DHPC compensated signals corresponding to the BABM parameters. Used with in *DWFs.m* and *SWFs.m*. The script was written by Captain Garrison Lindholm.

Inputs

t →Vector of time

w →Frequency (rad/sec)

eta →Stroke bias

AR →Amplitude, right wing

AL →Amplitude, left wing

tauR →Split-cycle shift, right wing

tauL →Split-cycle shift, left wing

M1pR →Magnitude 1st harmonic, right wing

M2pR →Magnitude 2nd harmonic, right wing

beta1pR →Phase 1st harmonic, right wing

beta2pR →Phase 2nd harmonic, right wing

M1pL →Magnitude 1st harmonic, left wing

M2pL →Magnitude 2nd harmonic, left wing

beta1pL →Phase 1st harmonic, left wing

beta2pL →Phase 2nd harmonic, left wing

Outputs

VR →Voltage signal to drive the right wing

VL →Voltage signal to drive the left wing

VIII. M_cp.m

This script was a designed to move the moments to the center of pressure. It was a post-processing function ran on the data file.

Inputs

file →File name of data structure

Outputs

data →Data structure with inputs, outputs, units, and information pertaining to the tests

Bibliography

- [1] AIAA. *Nomenclature and Axis Systems for Aerodynamic Wind Tunnel Testing*. AIAA G-129-2012. American Institute of Aeronautics and Astronautics, 2012. ISBN 978-1-60086-915-0.
- [2] Air Force Research Laboratory. “US Air Force Flapping Wing Micro Air Vehicle”, 2009. URL http://www.youtube.com/watch?v=_5YkQ9w3PJ4.
- [3] Anderson, Michael L. *Design and Control of Flapping Wing Micro Air Vehicles*. Ph.D. thesis, Air Force Institute of Technology, 2950 Hobson Way, Bldg 641, Wright-Patterson AFB OH 45433, September 2011.
- [4] Anderson, Michael L. and Richard G. Cobb. “Frequency Response of a Micro Air Vehicle Wing Flapping Mechanism to Non-Harmonic Forcing”. *51st AIAA/ASME/ASCE/AHS/ASC Structures, Structural Dynamics, and Materials Conference*, 0(2010-2708), April 2010.
- [5] Anderson, Michael L. and Richard G. Cobb. “Techniques for Non-Harmonic Wing Flapping for the Control of Micro Air Vehicles”. *AIAA Guidance, Navigation, and Control Conference*, 0(2010-7555), August 2010.
- [6] Anderson, Michael L. and Richard G. Cobb. “Towards Flapping Wing Control of Micro Air Vehicles”. *Journal of Guidance and Control*, 35:296–308, 2012.
- [7] Anderson, Michael L., Nathanael J. Sladek, and Richard G. Cobb. “Aero and Structural-dynamic Repeatability of a Novel MAV Wing Manufacturing Process”. *AIAA*. AIAA, 2011.
- [8] Anderson, Michael L., Nathanael J. Sladek, and Richard G. Cobb. “Evaluation of Bi-Harmonic Amplitude and Bias Modulation for Flapping Wing MAV Control”. *49th AIAA Aerospace Sciences Meeting including the New Horizons Forum and Aerospace Exposition*, 0(2011-1161), January 2011.
- [9] ATI Industrial Automation, Inc. “ATI Force / Torque Sensor: Nano17 Titanium”. URL http://www.ati-ia.com/products/ft/ft_models.aspx?id=Nano17+Titanium.
- [10] Bar-Cohen, Y. *Electroactive polymer (EAP) actuators as artificial muscles: reality, potential, and challenges*. SPIE Press monograph. SPIE Press, 2001. ISBN 9780819440549.
- [11] Conn, Andrew T., Stuart C. Burgess, and Chung S. Ling. “Design of a parallel crank-rocker flapping mechanism for insect-inspired micro air vehicles”. *Proceedings of the*

I MECH E Part C Journal of Mechanical Engineering Science, 221(10):1211–1222, 2007. ISSN 0954-4062.

- [12] Cranston, Brian C. *Evaluation of the thorax of the Manduca sexta for flapping wing micro air vehicle applications*. Master's thesis, Air Force Institute of Technology, December 2012.
- [13] de Croon, G. C. H. E., K. M. E. de Clercq, R. Ruijsink, B. Remes, and C. de Wagter. "Design, aerodynamics, and vision-based control of the DelFly". *International Journal of Micro Air Vehicles*, 1(2):71–97, June 2009.
- [14] Doman, David B., Michael W. Oppenheimer, and David O. Sigthorsson. "Dynamics and Control of a Minimally Actuated Biomimetic Vehicle: Part I - Aerodynamic Model". *AIAA Guidance, Navigation, and Control Conference*, 0(6160), August 2009.
- [15] Doman, David B., Michael W. Oppenheimer, and David O. Sigthorsson. "Dynamics and Control of a Minimally Actuated Biomimetic Vehicle: Part II - Control". *AIAA Guidance, Navigation, and Control Conference*, 0(6161), August 2009.
- [16] Dudley, R. *The Biomechanics of Insect Flight: Form, Function, Evolution*. Princeton paperbacks. Princeton University Press, 2002. ISBN 9780691094915.
- [17] DuPont. *DuPont Kapton® Polyimide Film*.
- [18] DuPont. *DuPont Teijin Films™*.
- [19] El-Hawary, M.E. *Introduction to Electrical Power Systems*. IEEE Press Series on Power Engineering. Wiley, 2008. ISBN 9780470411360.
- [20] Finio, Benjamin M., Jessica K. Shang, and Robert J. Wood. "Body torque modulation for a microrobotic fly". *ICRA*, 3449–3456. IEEE, 2009.
- [21] Grasmeyer, Joel M., Matthew T. Keennon, and Aerovironment Inc. "Development of the Black Widow Micro Air Vehicle". *39th AIAA Aerospace Sciences Meeting and Exhibit*. 2001.
- [22] Gullan, P.J. and P.S. Cranston. *The Insectons: An Outline of Entomology 3rd Edition*. Blackwell Publishing, 2005.
- [23] Hanrahan, Shawn. "*Manduca Sexta*".
- [24] JMP. *JMP 8 User Guide*, second edition.
- [25] Karpelson, Michael, Gu-Yeon Wei, and Robert J. Wood. "A review of actuation and power electronics options for flapping-wing robotic insects". *ICRA*, 779–786, 2008.

- [26] Karpelson, Michael, Gu-Yeon Wei, and Robert J. Wood. “Milligram-scale high-voltage power electronics for piezoelectric microrobots”. *ICRA*, 2217–2224. IEEE, 2009.
- [27] Keennon, Matthew, Karl Klingebiel, Henry Won, , and Alexander Andriukov. “Development of the Nano Hummingbird: A Tailless Flapping Wing Micro Air Vehicle”. *50th AIAA Aerospace Sciences Meeting including the New Horizons Forum and Aerospace Exposition*, January 2012.
- [28] Khan, Zaeem, Kyle Steelman, and Sunil Agrawal. “Development of insect thorax based flapping mechanism”. *ICRA*, 3651–3656. IEEE, 2009.
- [29] Kitching, Ian J. “The phylogenetic relationships of Morgan’s Sphinx, *Xanthopan morgani* (Walker), the tribe Acherontiini, and allied long-tongued hawkmoths (Lepidoptera: Sphingidae, Sphinginae)”. *Zoological Journal of the Linnean Society*, 135(4):471–527, 2002. ISSN 1096-3642.
- [30] Lindholm, Garrison J. and Richard G. Cobb. “Closed-Loop Control of a Constrained, Resonant-Flapping Micro Air Vehicle”. *AIAA Guidance, Navigation, and Control Conference*, 0(2012-4980), August 2012.
- [31] Lindholm, Garrison J., Ryan P. O’Hara, Mark F. Reeder, and Richard G. Cobb. “Power Requirements for Control of Flapping Wing Micro Air Vehicle using Piezoelectric Actuators”. *AIAA*, 2012-0917. 2012.
- [32] LPKF. *In-House Rapid PCB Prototyping Product Catalog*.
- [33] LPKF. *Micro-Material Processing with the LPKF ProtoLaser U3*.
- [34] Micro-Epsilon. “Position Sensor, CCD-Sensor, Laser Sensor: MICRO-EPSILON”. URL <http://www.optoncdt.com/>.
- [35] Myers, P., R. Espinosa, C. S. Parr, T. Jones, G. S. Hammond, and T. A. Dewey. “The Animal Diversity Web”, 2013. URL http://animaldiversity.ummz.umich.edu/accounts/Manduca_sexta/classification/.
- [36] Nelson, R.C. *Flight stability and automatic control*. WCB/McGraw Hill, 1998. ISBN 9780070462731.
- [37] Office of Secretary of Defense. “UAS ROADMAP 2005”. Print, August 2005.
- [38] Office of Secretary of Defense. “FY2009–2034 Unmanned Systems Integrated Roadmap”. Print, April 2009.

- [39] O'Hara, Ryan P. *The Characterization of Material Properties and Structural Dynamics of the Manduca Sexta Forewing for Application to Flapping Wing Micro Air Vehicle Design*. Ph.D. thesis, Air Force Institute of Technology, 2950 Hobson Way, Bldg 641, Wright-Patterson AFB OH 45433, September 2012.
- [40] Sladek, Nathanael J. *Flapping wing micro air vehicle wing manufacture and force testing*. Master's thesis, Air Force Institute of Technology, 2011.
- [41] Stevens, B.L. and F.L. Lewis. *Aircraft Control and Simulation*. Wiley, 2003. ISBN 9780471371458.
- [42] Trek. *Trek Model PZD700A M/S*.
- [43] Tu, Michael S. and Thomas L. Daniel. "Submaximal power output from the dorsolongitudinal flight muscles of the hawkmoth *Manduca sexta*". *Journal of Experimental Biology*, 207(26):4651–4662, 2004.
- [44] Wang, Qing-Ming and L Eric Cross. "Performance analysis of piezoelectric cantilever bending actuators". *Ferroelectrics*, 215(1):187–213, 1998.
- [45] Wood, Robert J., Erik Steltz, and Ronald S. Fearing. "Nonlinear Performance Limits for High Energy Density Piezoelectric Bending Actuators." *ICRA*, 3633–3640. IEEE, 2005.
- [46] Wu, Huaiyu, Dong Sun, and Zhaoying Zhou. "Micro air vehicle: configuration, analysis, fabrication, and test". *Mechatronics, IEEE/ASME Transactions on*, 9(1):108–117, March 2004. ISSN 1083-4435.

Vita

Captain Justin R. Carl graduated from Lovejoy High School in Hampton, Georgia. He performed undergraduate studies at Texas A&M University in College Station, Texas where he graduated with a Bachelor of Science degree in Mechanical Engineering in May 2008. He was a member of the Corps of Cadets Squadron 8 and obtained his commission through AFROTC Detachment 805 at Texas A&M University.

Upon commissioning, he was assigned to Edwards AFB, California where he served as the Executive Officer of the USAF Test Pilot School. He then served as a flight test engineer for the 418th Flight Test Squadron performing upgrade testing on the C-5 Galaxy. In September 2011, he entered the Graduate School of Engineering and Management, Air Force Institute of Technology. Upon graduation, he will be assigned to the Air Force Research Laboratory, Wright-Patterson AFB, Ohio.

REPORT DOCUMENTATION PAGE

Form Approved
OMB No. 0704-0188

The public reporting burden for this collection of information is estimated to average 1 hour per response, including the time for reviewing instructions, searching existing data sources, gathering and maintaining the data needed, and completing and reviewing the collection of information. Send comments regarding this burden estimate or any other aspect of this collection of information, including suggestions for reducing this burden to Department of Defense, Washington Headquarters Services, Directorate for Information Operations and Reports (0704-0188), 1215 Jefferson Davis Highway, Suite 1204, Arlington, VA 22202-4302. Respondents should be aware that notwithstanding any other provision of law, no person shall be subject to any penalty for failing to comply with a collection of information if it does not display a currently valid OMB control number. **PLEASE DO NOT RETURN YOUR FORM TO THE ABOVE ADDRESS.**

1. REPORT DATE (DD-MM-YYYY) 21-03-2013		2. REPORT TYPE Master's Thesis		3. DATES COVERED (From — To) Oct 2011-Mar 2013	
4. TITLE AND SUBTITLE Power Requirements for Bi-harmonic Amplitude and Bias Modulation Control of a Flapping Wing Micro Air Vehicle				5a. CONTRACT NUMBER	
				5b. GRANT NUMBER	
				5c. PROGRAM ELEMENT NUMBER	
6. AUTHOR(S) Carl, Justin R., Captain, USAF				5d. PROJECT NUMBER	
				5e. TASK NUMBER	
				5f. WORK UNIT NUMBER	
7. PERFORMING ORGANIZATION NAME(S) AND ADDRESS(ES) Air Force Institute of Technology Graduate School of Engineering and Management (AFIT/EN) 2950 Hobson Way WPAFB, OH 45433-7765				8. PERFORMING ORGANIZATION REPORT NUMBER AFIT-ENY-13-M-37	
9. SPONSORING / MONITORING AGENCY NAME(S) AND ADDRESS(ES) intentionally left blank				10. SPONSOR/MONITOR'S ACRONYM(S)	
				11. SPONSOR/MONITOR'S REPORT NUMBER(S)	
12. DISTRIBUTION / AVAILABILITY STATEMENT DISTRIBUTION STATEMENT A: APPROVED FOR PUBLIC RELEASE; DISTRIBUTION UNLIMITED					
13. SUPPLEMENTARY NOTES This work is declared a work of the U.S. Government and is not subject to copyright protection in the United States.					
14. ABSTRACT Flapping wing micro air vehicles (FWMAV) have been a growing field in the research of micro air vehicles, but little emphasis has been placed on control theory. Research is ongoing on how to power FWMAVs where mass is a major area of concern. However, there is little research on the power requirements for the controllers to manipulate the wings of a FWMAV. A novel control theory, BABM, allows two actuators to produce forces and moments in five of the FWMAV's six DOF. Several FWMAV prototypes were constructed and tested on a six-component balance. Data was collected for varying control parameters and the generated forces were measured. The results mapped control parameters to different degrees of freedom. The force required to generate desirable motion and power required to generate that motion was plotted and evaluated. These results can be used to generate a minimum power controller in the future. The results showed that BABM control required a 26% increase in power in order to increase lift by 22%. The lift increase was accomplished by increasing the amplitude by 10% over the established baseline. The data also showed that varying some parameters actually decreased the power requirements, allowing other parameters to increase which in turn would enable more complex maneuvers. For instance, an asymmetric change in split-cycle shift of ± 0.25 decreased the power required by 14% and decreased the lift by 25%. Changing the stroke bias to ± 0.75 had a negligible effect on power but decreased the lift by 27%. Furthermore, the data identified certain parameter combinations which resulted in other forces and moments. These results identified how BABM be used as a control theory for the control of FWMAVs.					
15. SUBJECT TERMS Flapping Wing MAV, MAV Control, Control Power, BABM, Split-cycle					
16. SECURITY CLASSIFICATION OF:			17. LIMITATION OF ABSTRACT	18. NUMBER OF PAGES	19a. NAME OF RESPONSIBLE PERSON
a. REPORT	b. ABSTRACT	c. THIS PAGE			19b. TELEPHONE NUMBER (include area code)
U	U	U	UU	130	Richard G. Cobb (ENY) (937) 255-3636 ext. 4559